Journal of Materials Chemistry A

REVIEW

View Article Online
View Journal | View Issue

Cite this: J. Mater. Chem. A, 2018, 6, 12876

Sunlight-driven water-splitting using two-dimensional carbon based semiconductors

Pawan Kumar,[a] Rabah Boukherroub *[b] and Karthik Shankar *[a]

The overwhelming challenge of depleting fossil fuels and anthropogenic carbon emissions has driven research into alternative clean sources of energy. To achieve the goal of a carbon neutral economy, the harvesting of sunlight by using photocatalysts to split water into hydrogen and oxygen is an expedient approach to fulfill the energy demand in a sustainable way along with reducing the emission of greenhouse gases. Even though the past few decades have witnessed intensive research into inorganic semiconductor photocatalysts, their quantum efficiencies for hydrogen production from visible photons remain too low for the large scale deployment of this technology. Visible light absorption and efficient charge separation are two key necessary conditions for achieving the scalable production of hydrogen from water. Two-dimensional carbon based nanoscale materials such as graphene oxide, reduced graphene oxide, carbon nitride, modified 2D carbon frameworks and their composites have emerged as potential photocatalysts due to their astonishing properties such as superior charge transport, tunable energy levels and bandgaps, visible light absorption, high surface area, easy processability, quantum confinement effects, and high photocatalytic quantum yields. The feasibility of structural and chemical modification to optimize visible light absorption and charge separation makes carbonaceous semiconductors promising candidates to convert solar energy into chemical energy. In the present review, we have summarized the recent advances in 2D carbonaceous photocatalysts with respect to physicochemical and photochemical tuning for solar light mediated hydrogen evolution.

Received 4th March 2018
Accepted 23rd May 2018

DOI: 10.1039/c8ta02061b

rsc.li/materials-a

[a]Department of Electrical and Computer Engineering, University of Alberta, 9211-116 St, Edmonton, Alberta, Canada T6G 1H9. E-mail: kshankar@ualberta.ca

[b]Univ. Lille, CNRS, Centrale Lille, ISEN, Univ. Valenciennes, UMR 8520 – IEMN, F-59000 Lille, France. E-mail: rabah.boukherroub@iemn.univ-lille1.fr

Dr Pawan Kumar received his PhD degree in Chemical Science from CSIR-Indian Institute of Petroleum, Dehradun, India in 2016 under the guidance of Dr Suman L. Jain. Prior to PhD, he worked at R&DE, DRDO, Ministry of Defense, Pune, India, as a Junior Research Fellow. During his PhD, he was awarded the prestigious Raman-Charpak fellowship in 2014 by Campus France to work with Prof. Rabah Boukherroub (IEMN & University of Lille, France). After his PhD, he joined the research group of Prof. Radek Zboril at RCPTM, Palacky University, Czech Republic as a postdoctoral fellow. Currently, he is a postdoctoral researcher at the University of Alberta, Canada in the group of Prof. Karthik Shankar. His research interests are focused on the synthesis of advanced photocatalytic materials for energy applications, the heterogenization of molecular catalysts, the modification of carbon nitride and the development of photocatalysts for CO_2 activation, water splitting and photo-organic transformations.

Dr Rabah Boukherroub received a PhD in chemistry from the University Paul Sabatier in Toulouse, France. He is currently a CNRS research director and a group leader at the Institute of Electronics, Microelectronics and Nanotechnology (IEMN), University of Lille, France. He is an Associate Editor for ACS Applied Materials & Interfaces. He is also a guest Professor, China University of Petroleum, Qingdao, China. His research interests are in the area of nanostructured functional materials, surface chemistry, and photophysics of semiconductor/metal nanostructures with emphasis on biosensors, nanomedicine, photocatalysis and energy-related applications. He is a co-author of 480+ research publications and wrote 31 book chapters on subjects related to nanotechnology, materials chemistry, and biosensors. He has 11 patents or patents pending.

1. Introduction

The two biggest long term challenges of modern technological civilization are global warming due to anthropogenic carbon emissions and the steadily rising global energy demand. The problem of shortage of fossil fuels and increased CO_2 concentration in the environment due to burning of fossil fuels bring up the urgency to search for carbon neutral clean energy to sustain environmental and energy issues.[1] Due to the exponential growth of world population and global economic growth, the world's energy consumption is expected to double by 2050 and triple by the end of the century relative to the present consumption (14 TW).[2] Sunlight is an inexhaustible and continuous source of energy; approximately 4.3×10^{20} J of energy strikes the surface of the earth per hour, which is more than the current consumption of energy by all of humanity in one year.[3,4] Plants and phytoplankton are able to harvest this energy and approximately 100 Terawatts of energy is harvested, which is about six times larger than the power consumption of human civilization.[5] Plants convert solar energy into chemical energy by two reactions: (i) splitting of water into hydrogen and oxygen in which hydrogen is trapped as reduced nicotinamide adenine dinucleotide phosphate (NADPH), while oxygen is released into the environment to be used by other creatures for food oxidation, and (ii) conversion of CO_2 into organic molecules using electrons derived from water splitting. Nature has thus demonstrated that solar energy can be stored in the form of chemical bonds, which can be used to meet our energy demand.[6] Although photovoltaic devices have been deployed to convert solar energy into electrical energy with up to 43.5% efficiency, these devices encounter certain disadvantages such as intermittency, high production costs and long energy payback times.[7,8]

Dr Karthik Shankar is an Associate Professor in the Department of Electrical & Computer Engineering at the University of Alberta. He received M.S. and PhD degrees in Electrical Engineering from The Pennsylvania State University, and obtained his B.Tech degree from the Department of Metallurgy and Materials Science at the Indian Institute of Technology-Madras. He is an Associate Editor for IEEE Sensors Letters and an Editor for the Journal of Materials Science: Materials in Electronics (JMSE). He joined the University of Alberta in 2009 and received the Petro-Canada Young Innovator Award in 2010. From 2012–2017, he held a secondment to NRC-NINT as a Research Officer. His research interests consist of organic semiconductors, nanomaterials, plasmonics, solar cells and photocatalysts. As of April 2018, he has authored more than 100 journal articles that have collectively been cited over 16 000 times.

Hydrogen has been considered as a clean solar fuel due to its high free energy content ($\Delta G = +237$ kJ mol^{-1}), easily accessible water resource, and production of water and oxygen as sole by-products.[9,10] Alternatively, hydrogen due to its high energy content can convert CO_2 into hydrocarbons such as methanol, which is compatible with internal combustion engines. Additionally, as a liquid phase, it can be stored and transported easily. Currently, hydrogen is produced on a large scale by reforming (dry or steam reforming) of hydrocarbons or through gasification of fossil fuels, both of which produce large amounts of CO_2.[11] The photocatalytic production of hydrogen from water splitting is a viable approach to sustain the process which relies on two most abundant resources, water and sunlight.[12] Solar light mediated water splitting can be achieved by two methods: (i) using a photoelectrochemical cell where a semiconductor electrode, immersed in water, is irradiated with light and another electrode works as a carrier counter electrode; (ii) using a photocatalytic reactor wherein particles of a semiconductor photocatalyst suspended in water act as micro-photoelectrodes and facilitate oxidation and reduction reactions of water on their surface.

Since the initial experiment by Fujishima and Honda in 1972 on photoelectrochemical water splitting using a TiO_2 photoelectrode,[13] numerous semiconductor materials relying on *d*-block elements have been explored for solar light mediated hydrogen production. Subsequently, Bard's group demonstrated photocatalytic water splitting using suspended semiconductor particles.[14] Both photoelectrochemical and photocatalytic methods have pros and cons. Photocatalytic systems are extremely simple and have lower operating costs, but cannot profit from the use of a bias to separate charge carriers, thus limiting the achievable efficiency of conversion of sunlight into chemical energy; also, the separation of evolved hydrogen and oxygen poses a problem.[15] Up until now, different material systems such as oxides, sulfides, phosphides, nitrides, oxynitrides, oxysulfides, *etc.*, have been developed for the photocatalytic conversion of solar energy into chemical energy.[16] However, even after 45 years of research, the quantum efficiency remains too low to justify the scaling up of hydrogen production to the industrial level. An efficient photocatalytic system which can provide four consecutive proton coupled electron transfer (PCET) steps to achieve overall water splitting with a high photoconversion efficiency is still a challenge to the scientific community. Overall water splitting involves two half reactions – the oxidation of water which produces O_2, protons and electrons (OER), and the reduction of protons which produces hydrogen (HER), eqn (1)–(3). In order to sustain the process of water splitting, both OER and HER processes should occur simultaneously to chain the flow of electrons.

Overall water splitting

$$2H_2O + h\nu \rightarrow 2H_2 + O_2 \quad (1)$$

Oxygen evolution reaction (OER)

$$2H_2O \rightarrow 4H^+ + 4e^- + O_2 \quad (2)$$

Hydrogen evolution reaction (HER)

$$4H^+ + 4e^- \rightarrow 2H_2 \quad (3)$$

The reduction potential of H^+/H_2 is 0.00 V at pH 0 *vs.* NHE; however −0.41 V overpotential is needed for the production of hydrogen in aqueous solutions at pH 7 *vs.* NHE, while the potential for water oxidation H_2O/O_2 is +1.23 V *vs.* NHE at pH 0 (or +0.82 V *vs.* NHE at pH 7). According to these values, a minimum semiconductor band gap energy of 1.23 eV is required to drive the overall water splitting reaction. In practice, a slightly larger bandgap of 1.35 eV or higher is required to split water due to overpotential-related losses. The value of potential can be changed to any pH by using equation $E^0 = E^0(pH_0) - 0.06pH$, where E^0 is the standard reduction potential.[17,18] Furthermore, the position of the semiconductor valence band should be more positive than +0.82 V *vs.* NHE at pH 7, while the position of the conduction band should be more negative than −0.41 V *vs.* NHE at pH 7.

Many inorganic semiconductors such as CoP, $NaTaO_3$, ZnO, $InVO_4$, $ZnGa_2O_4$, ZnS, Ta_3N_5, Cu_2ZnSnS_4, and CdS and mixed metal oxides such as $Ru_xTi_{1-x}O_2$, Rh–Cr mixed oxide nanoparticles, dispersed $(Ga_{1-x}Zn_x)N_{1-x}O_x$ and ZrO_2-supported $Ni_xFe_{3-x}O_4$, *etc.*, are developed as water splitting photocatalysts.[20–22] However, solar to fuel conversion efficiency is still limited to 1–2% due to charge recombination, lack of visible light absorption, and poor charge separation. A low electronic band gap to absorb in the visible region, appropriately long carrier lifetimes and/or carrier diffusion lengths, earth abundance, high stability, nontoxic nature and easy processability are the prime requirements of an ideal photocatalyst. Unfortunately, many promising semiconductors, especially oxides, have a wide band gap and absorb light below 400 nm, which represents only 4% of the whole solar spectrum (Fig. 1). If all the incident UV light on Earth up to 400 nm can be harvested, only 2% solar conversion efficiency can be achieved, which is equal to the maximum conversion efficiency of photosynthesis in green plants (1–2%).[23] Furthermore, the inherent health hazards of UV light require specially designed reactors with quartz windows, which add an extra cost to the process. So, in order to achieve maximum solar conversion efficiency, it is of utmost importance to harvest visible light which is approximately 45% of the total solar spectrum. If it is possible to harvest solar light up to 600 nm, the conversion efficiency can be increased up to 16% which can be further increased up to 32% if light up to 800 nm can be captured. Furthermore, charge recombination is prevalent and it is estimated that only 10% of photogenerated electron–hole pairs are available for water splitting. Charge recombination can take place on the surface or in the bulk of semiconductors (Fig. 2a). Surface recombination can be slowed down by forming heterojunctions through surface decoration with noble metal nanoparticles, which causes the formation of Schottky barriers;[24,25] the built-in field associated with the Schottky barrier prevents fast recombination. Another option is to use promoters – hole capturing agents, *i.e.*, IrO_2, CoO_x, RuO_2, *etc.*,[26–28] (Fig. 2b) or perform the catalytic reaction in the presence of hole scavengers such as alcohols. Volume recombination can be prevented by reducing the semiconductor particle size[29] or modifying the surface morphology (nanotubes and nanospikes) so that more electrons and holes can reach the surface and are available for the photoreaction. The ideal nanostructure is one where the processes of light absorption and charge separation are orthogonalized and wherein the maximum distance that photogenerated carriers have to travel to reach the site of chemical reaction is smaller than the retrieval length in that material.[30–32]

Apart from these approaches, the hybridization of a nanostructured large band gap n-type semiconductor with a low band gap p-type semiconductor to create a type-II (staggered) p–n heterojunction is also a useful strategy.[34,35] The depletion region or energy band offset at the heterojunction interface creates a driving force for efficient charge separation, thus

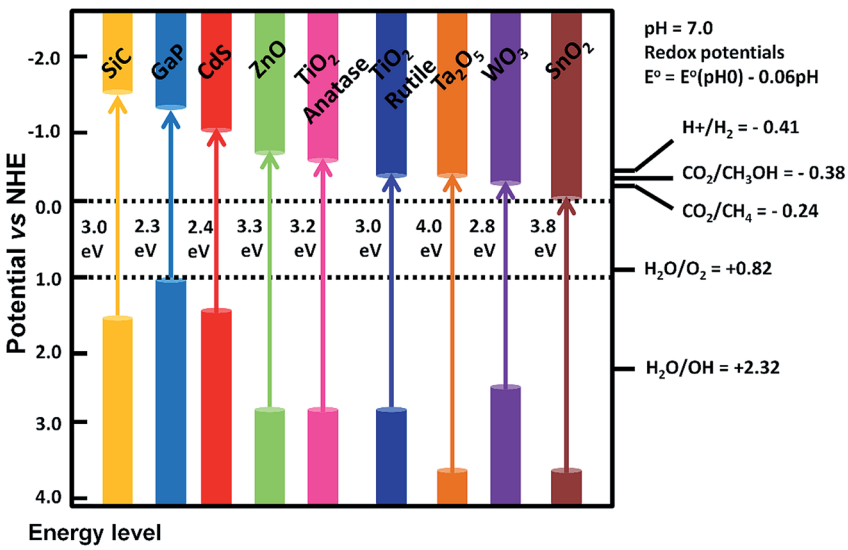

Fig. 1 Band gap and band edge positions of a range of semiconductors *vs.* NHE at pH 7 representing the redox potential of water splitting. Adapted with permission from ref. 19.

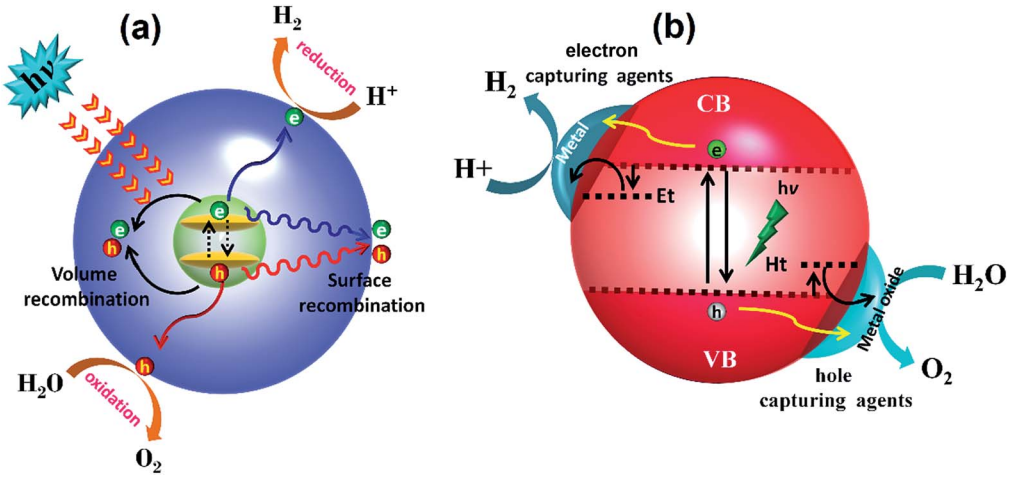

Fig. 2 (a) Schematic illustration of the charge generation, separation, recombination and conversion processes in photocatalysts and (b) facilitation of charge separation by electron and hole capturing agents. Adapted with permission from ref. 24 and 33.

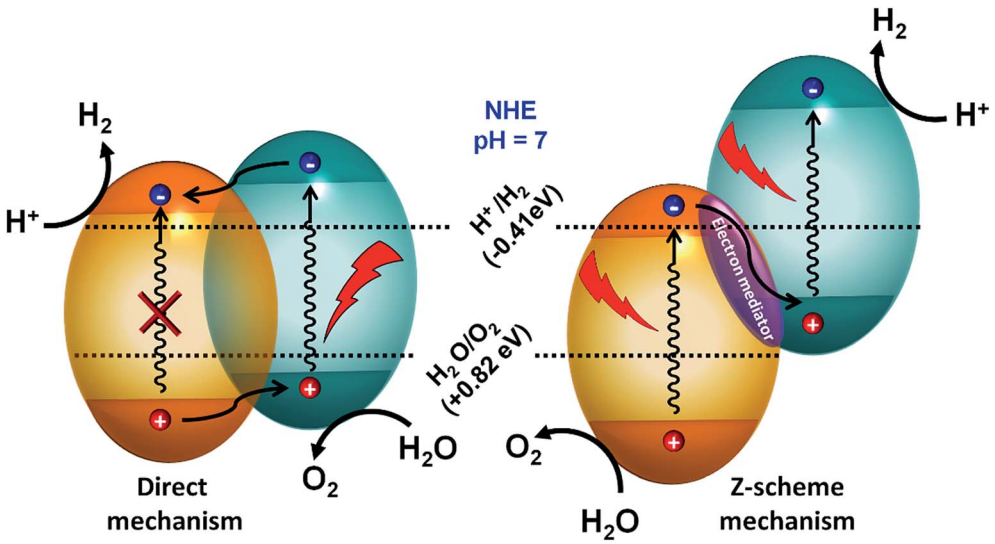

Fig. 3 Mechanistic representation of direct and Z-schemes of photocatalysis on two different band gap semiconductors for overall water splitting.

preventing geminate recombination. The low band gap p-type semiconductor can absorb visible light and transfer the photogenerated electrons to the conduction band of the large band gap semiconductor, while photogenerated holes in the p-type react directly with the reactants on the surface (direct mechanism) (Fig. 3). Another more fascinating approach involves mixing of two low band gap semiconductors one of which has a more positive valence band (oxidative) and facilitates water oxidation, while the other has a more negative conduction band to facilitate proton reduction (reductive). Individually none of them can sustain overall water splitting, while when they are mixed together they can sustain the process of overall water splitting. Following the absorption of light, photogenerated electrons in the conduction band of the oxidative semiconductor annihilate photogenerated holes in the reductive semiconductor. These electrons in the conduction band of the reductive semiconductor facilitate proton reduction, while holes in the valence band of the reductive semiconductor facilitate water oxidation. This mechanism is called the Z-scheme mechanism and needs two photons for the completion of overall water splitting (Fig. 3).[36,37] Many examples of Z-scheme photosystems for water splitting have been described in the literature, including $SrTiO_3$:La,Rh and $BiVO_4$:Mo,[38] $BiVO_4$ and Ru/$SrTiO_3$:Rh,[39] Ir/CoO_x/Ta_3N_5 and Ru/$SrTiO_3$:Rh,[40] *etc.* Generally Z-scheme catalysts require an electron mediator, *i.e.*, (Fe^{3+}/Fe^{2+}, $[Co(bpy)_3]^{3+/2+}$, graphene), which facilitates charge transfer at the interface of contact.[41,42]

Although a lot of research has been dedicated to reducing the bandgap of semiconductors to achieve high solar to hydrogen (STH) conversion, photocatalytic performance is still limited by low absorption coefficients for visible regime photons, poor quantum yields, fast carrier recombination,

photo-corrosion and reliance on expensive noble metal co-catalysts. In recent years, two-dimensional (2D) carbon based materials have emerged as new photocatalytic materials due to their excellent electronic, optical, physicochemical and surface properties.[43–48] Carbonaceous materials are earth abundant and provide a niche for nanoscale modification in the chemical and morphological structure, which facilitates efficient charge separation.[49] In the past decade, the exponential rise in the number of reports on carbon materials for photocatalytic applications makes evident their wide potential for various applications. Numerous carbon based 2D materials such as graphene, graphene oxide (GO), carbon nitride (C_3N_4), polyimide polymers, holey graphene (C_2N), doped carbon quantum dots and their 2D derivatives have been introduced.[50–52] Carbon materials being composed of conjugated sp^2 carbon networks provide excellent charge carrier mobility on their surface. The high surface area of 2D materials and rapid charge transport over the surface of conjugated carbon based materials result in short paths for carriers to reach reaction sites and remove the reliance on metal based electron and hole capturing agents thus providing opportunities to create metal-free photocatalysts.[53–55]

Among various carbon based materials, graphene is the most intensively investigated in photocatalytic applications to increase the performance of inorganic semiconductors due to its exceptionally conductive surface and high specific surface area; however, the absence of a band gap restricts its role in photosensitization.[56–59] Although a limited increase in photocatalytic performance has been demonstrated for several graphene/inorganic hybrids, the inorganic semiconductor remains the charge generation center along with its inherent drawbacks.[60–62] Band gap opening in graphene by doping with heteroatoms and promoting defects is the most effective method to convert metallic graphene into a semiconductor to exploit its sub-nanoscale properties.[63–66] The differential electronic densities and divergent atomic centers give rise to various active sites for photoreactions. While doped graphene materials can absorb a wide swathe of photons in sunlight to generate electron–hole pairs due to their narrow bandgap, the VB maxima remain unfavorable and produce poorly oxidative holes to facilitate water oxidation.[67–69] The band gap broadening can be achieved by adding high dopant concentrations, but this reduces the number of π-conjugated conductive nanochannels required for efficient charge separation.[70] Furthermore, difficulties in the mass production of graphene/doped graphene limit the application of this frontier material in photocatalysis. Doped carbon derived from a heteroatom-rich source, possessing less ordered doped graphenic domains, seems amenable to scale-up and mass production due to the ease of synthesis. However, doped carbon inherits the drawbacks of graphene such as a very narrow band gap, self-degradation, and deactivation of active sites due to which their application beyond electrocatalysis is less promising.[71–74] On the other hand, graphene oxide (GO) behaves as a semiconductor possessing a variable band gap depending on oxygen concentration due to the presence of defects and oxygen rich sp^3 hybridized carbon domains. The maximum hydrogen yield achieved using GO was 2833 μmol h^{-1} in the presence of a methanol sacrificial donor in contrast to 46.6 μmol h^{-1} in the absence of a sacrificial donor.[75] The formation of hybrids and heterojunctions of graphene/graphene oxide with inorganic semiconductors/dye molecules/metals and doping have been used to achieve high H_2 yields in the presence of sacrificial reagents.[60,76–79] However, the use of methanol and other sacrificial reagents is undesirable for sustainable hydrogen production. Therefore, an ideal material should have the requisite band structure and active sites to facilitate the simultaneous reduction and oxidation of water instead of requiring the use of sacrificial electron or hole scavengers.

Recently, 2D polymeric semiconductors have been envisaged as future photocatalysts due to the ease of synthesis from cheap resources, superior visible light absorption, tunable band gap and easy processability.[48,53,80,81] Graphitic carbon nitride (g-C_3N_4), a polymeric material composed of triazine (C_3N_3) or tri-*s*-triazine/heptazine (C_6N_7) units with alternate C and N, provoked excitation in the photocatalysis community due to its resilient stability (chemical inertness, thermal resistance and absence of photocorrosion), appropriate band structure and ease of synthesis from benign sources.[82–86] Since the first report by Wang *et al.* in 2009 on photocatalytic water splitting using g-C_3N_4, this field has witnessed intensive research activity.[87] g-C_3N_4 possesses a moderate band gap of 2.6–2.7 eV and its CB and VB redox potential values lie at −1.1 eV and +1.6 eV, respectively with a substantial lifetime span of the photoexcited state (nanosecond regime) making it a suitable photocatalytic material for water splitting.[88] Apart from the band gap, the presence of numerous nitrogen rich sites and ordered defects provides active centers for the substrate interaction, which increases reactant concentration on the catalyst surface for catalytic and photocatalytic reactions.[80,89–91] However, extending the visible light absorption profile of g-C_3N_4 beyond 450–460 nm and increasing the carrier lifetime are the major challenges. Numerous nanoarchitecture assemblies of g-C_3N_4 and inorganic semiconductor/dye molecules/graphenic materials have been designed for improving charge separation and visible light absorption parameters.[92] Doping with metal atoms/ions and heteroatoms has also been used to shift the visible light absorption profile towards longer wavelengths.[93–97] The synthesis of carbon nitride materials from nitrogen rich precursors affords porous bulk g-C_3N_4.[98] In bulk carbon nitride, graphenic C_3N_4 sheets remain stacked together, which compromises the photocatalytic efficiency due to a substantial amount of concealed surface that is unexposed to light and reactants. These stacked sheets can be metamorphized into few layered 2D C_3N_4 sheets by various solvent intercalations.[48,99–102] However, the exfoliation of g-C_3N_4 to sheets works to the detriment of photocatalytic performance due to band gap broadening and loss of crystallinity due to abundant intralayer hydrogen bonds between sheets, which promote charge localization and lead to poor intralayer carrier transport.[103–105] Furthermore, residual functionalities also act as carrier trapping centers, which reduce the quantum efficiency of photocatalysis. Hence forming few layered g-C_3N_4 sheets while maintaining crystallinity to decrease trap sites is the best approach to synergistically achieve a combination of high

surface area and good charge transport/separation. Actually, crystalline carbon nanosheets have afforded some of the highest reported H_2 yields among carbon based materials as high as 9577.6 μmol h^{-1} g^{-1} with a quantum efficiency of 9.01% at 420 nm, which was 15.5 times higher than that of bulk g-C_3N_4.[106] The nanosheets of carbon nitride can be further modified with quantum dots, graphene, doped graphene, and doped carbon nitride sheets to improve photocatalytic performance.[107–109]

Although g-C_3N_4 is a good hydrogen evolution catalyst, its VB band edge potential is less positive so its water oxidation performance remains underwhelming. The photocatalytic performance of g-C_3N_4 to achieve overall water splitting can be improved by introducing electron rich or deficient units into the framework, which shift band edge positions such that the band structure of g-C_3N_4 can be tuned. The polyimide derivative of carbon nitride synthesized by heating triazine precursors and dianhydride precursors at high temperature offers tunable band gap imide semiconductors.[110–112] The band structure of these polyimide polymers depends on the ratio of triazine/heptazine and dianhydride, and by controlling the type of monomer unit, a more oxidative VB position can be achieved. Apart from band edge tuning, these materials possess a higher visible light absorption and the presence of different charge density units facilitates better charge separation within the sheets.

Certain other 2D semiconductors with better optical and charge transport properties have been reported in the past few years. One of these semiconductors is C_2N (holey graphene) whose narrow band gap and ordered porous structure make it a suitable candidate for various applications, including water splitting.[113] Theoretical investigations suggested that combining C_2N nanohybrids with other 2D semiconductor materials is a promising approach to optimally harvest sunlight with a high quantum efficiency.[114] 2D–2D hybrids are better than conventional hybrids due to superior face to face interactions, which facilitate better charge transfer and carrier mobility. However, for C_2N hybrids, most of the discussion is limited to theoretical calculations and more efforts are needed to experimentally realize such nanohybrids.

This review represents an extended discussion on various 2D carbon materials, focusing on their synthesis, properties, photocatalytic performance, and chemical and structural modification of their framework *via* various approaches to achieve an appropriate band structure for water splitting. The initial sections of this review will cover graphene/graphene oxide based materials with a specific focus on improved charge carrier separation and band gap opening *via* various dopants and their nanocomposites with inorganic semiconductors for hydrogen generation. Next, carbon nitride based polymers as semiconductors will be surveyed, and improvements in their photocatalytic performance through surface engineering, 2D sheet transformation, band structure manipulation and particularly, chemical modification by replacement and/or doping of triazine or heptazine units will be reviewed in depth. Later in this review, 2D polyimide polymers, carbonaceous-inorganic 2D–2D semiconductors, emerging carbon based semiconductors, *i.e.*, C_2N, C_3N, molecular 2D semiconductors, carbonaceous quantum dots and their nanohybrids with carbon nitride sheets for solar to hydrogen generation will be scrutinized.

2. Graphene based materials as photocatalysts

In contrast to inorganic 2D materials, carbonaceous 2D materials such as graphene, graphene oxide, and carbon nitride have emerged as potential photocatalytic materials due to their exceptional features including, but not limited to, high surface area, excellent charge transport and favorable optical properties.[115–117] The discussion on 2D carbonaceous structures is incomplete without graphene, which impelled the research on various advanced carbon based materials for numerous applications. Graphene is a monoatomically thick sp^2-hybridized 2D carbon layer arranged in a hexagonal fashion with a continuous π–π conjugated network. Ideally, graphene is a monoatomic layer sheet of graphite. Graphene has emerged as an almost magical material in the world of materials science due to its astonishingly high surface area (2630 m^2 g^{-1}), excellent electron mobility on its surface (200 000 cm^2 V^{-1} s^{-1}), high mechanical strength (1060 GPa), high thermal conductivity (3000 W m^{-1} K^{-1}), and favorable optical and chemical properties.[118] Since the first report on the discovery of graphene by the scotch tape method by Geim and Novoselov,[119] tremendous advancements in the field of graphitic materials have been achieved for various applications such as batteries, solar cells, fuel cells, biosensors, supercapacitors, catalysts, photocatalysts, *etc.*[120–125] The isolation of a single layer defect-free graphene sheet has been attempted by various physical means such as thermal exfoliation, chemical vapor deposition (CVD), ultrasonication and solvent assisted exfoliation.[126] But expensive and tedious procedures and inability to accomplish large scale production limit commercial deployment. Chemical oxidation of graphite with harsh oxidizing agents like $KMnO_4$ + H_2SO_4, H_3PO_4 + H_2SO_4, H_2O_2 + HCl, *etc.*, partially oxidize graphite bulk material to graphite oxide and sheets can be easily separated due to repulsive forces between negatively charged sheets to produce graphene oxide (GO).[127,128] The GO sheets can be reduced partially by chemical, hydrothermal or thermal treatment to prepare reduced graphene oxide (rGO).[129] Although these methods produce graphene sheets with few defects, their attributes are still comparable to graphene. Due to excellent conductivity and zero band gap, which facilitate fast charge transfer on graphene surfaces, numerous nanohybrid composites of rGO with various semiconductors such as TiO_2, ZnO, WO_3, Cu_2O, CuO, Fe_2O_3, MnO_2, ZrO_2, ZnS, CdS, CdSe, Bi_2WO_6, MoS_2, $BiVO_4$, $Sr_2Ta_2O_7$, $InVO_4$, $ZnFe_2O_4$, *etc.*, have been reported for photocatalytic and other applications.[60,130–133] As per the rule of diffusion of charge ($t = d^2/k^2D$, where d = particle size, k = constant, and D = diffusion coefficient), two dimensional sheets are more appealing for the water splitting process due to the facilitation of transport of photogenerated charges to reaction sites prior to recombination.[134] Apart from high surface area and a more conductive surface, it has been reported that

graphene can work as a macromolecular photosensitizer and reduce the band gap of semiconductors.[135] For example, ZnS is a wide band gap semiconductor which absorbs in the UV spectral range, while its composite with graphene (ZnS GR nanocomposite) is fairly photoactive under visible light.[136] Among various graphene/semiconductor composite materials, cobalt oxide/graphene has proved to be an efficient catalyst. Liang *et al.* demonstrated that Co_3O_4 nanocrystals grown on rGO can act as a bi-functional catalyst in the oxygen reduction reaction (ORR) and oxygen evolution reaction (OER),[137] even though both Co_3O_4 and rGO, taken separately, have small affinity for these reactions. The conjugation of Co_3O_4 and rGO drastically increased their electrocatalytic activity due to synergistic chemical coupling effects between Co_3O_4 and graphene. Nitrogen doping further enhanced the activity as well as stability of the composite. Cobalt oxide nanoparticles and B,N-decorated graphene (CoO_x NPs/BNG) compounds displayed better ORR and OER activity due to improved electron transfer capacity, plenty of Co–N–C active sites and strong coupling effects.[138] The nanocomposites of rGO with hydrogen evolving semiconductors have been found to be good hydrogen evolving photocatalysts. The band edge position of CdS is suitable for hydrogen evolution; however in the nanostructured form, CdS has a tendency to aggregate, resulting in a low surface area and therefore a lower yield. The synthesis of a nanocomposite of CdS with GO by a hydrothermal method produces CdS nanoparticles homogeneously distributed on the surface of rGO. In the hydrothermal treatment, residual oxygen functionalities facilitate better attachment of nanoparticles to the sheets. It is important to note that hydrothermal treatment does not completely remove oxygen functionalities from the surface of GO. The prepared rGO–CdS nanocomposites showed enhanced water splitting characteristics.[139–141] The rGO loading is crucial for achieving an optimal hydrogen evolution rate. Excessive loading may prevent light from reaching the semiconductor surface and inhibit electron–hole pair generation. Furthermore, Pt loading increases the photoefficiency of the composite. By using a Pt loaded (1 wt%) rGO/CdS nanocomposite, a quantum efficiency of 22.5% can be reached for hydrogen evolution at 420 nm (Fig. 4).[141] N-doped graphene (N-graphene) further increases the hydrogen evolution rate due to the creation of a heterojunction between N-graphene sheets and CdS, which facilitates better charge transfer. The N-graphene (2 wt%)/CdS composite exhibited the highest H_2 evolution rate which was approximately five times that of CdS alone.[142]

Core–shell structures, prepared using two or more components, have proven themselves to be better advanced functional materials for improved photocatalytic performance due to synergistic attributes in terms of uniformity in size, manipulation in core and shell composition, dispersibility, stability, and tunability of optical, catalytic, and magnetic properties. Apart from this, the formation of a p–n heterojunction at the inner core and outer shell interface can be used to facilitate enhanced charge carrier concentration on the surface.[143] Many core–shell morphologies such as rods, spheres, hollow spheres, spindles, *etc.*, with different arrangements of the semiconductor in the core and shell have been prepared for solar light-driven water splitting.[144] Graphene coated nanostructured semiconductor particles provide promising results for the water splitting reaction due to better dispersibility of charge over graphene sheets.[145] Few layer thick graphene sheet-wrapped particles are more efficient than bulk nanocomposites due to transmission of light from few layered graphene sheets to the semiconductor assembly and better charge transportation on the surface of graphene sheets. Few nanometer thick rGO coated anatase TiO_2 nanoparticles (graphene–TiO_2 NPs) were synthesized by the surface functionalization of TiO_2 with APTMS (3-aminopropyl trimethoxysilane) to create a positively charged TiO_2 surface and subsequent wrapping of negatively charged graphene oxide followed by hydrothermal reduction and annealing.[146] The obtained graphene–TiO_2 NPs

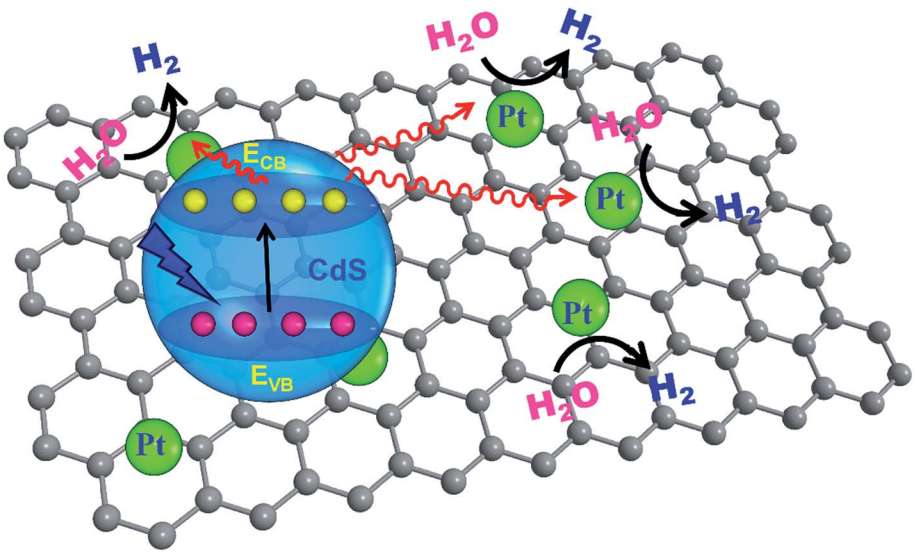

Fig. 4 Schematics of visible light driven electron–hole pair generation in CdS and its efficient separation on reduced graphene oxide in the CdS/rGO nanocomposite. The photogenerated electrons in the conduction band of CdS are transferred to Pt and rGO sheets, which facilitate better charge separation and electrons are more easily accessible to protons to generate H_2. Adapted with permission from ref. 141.

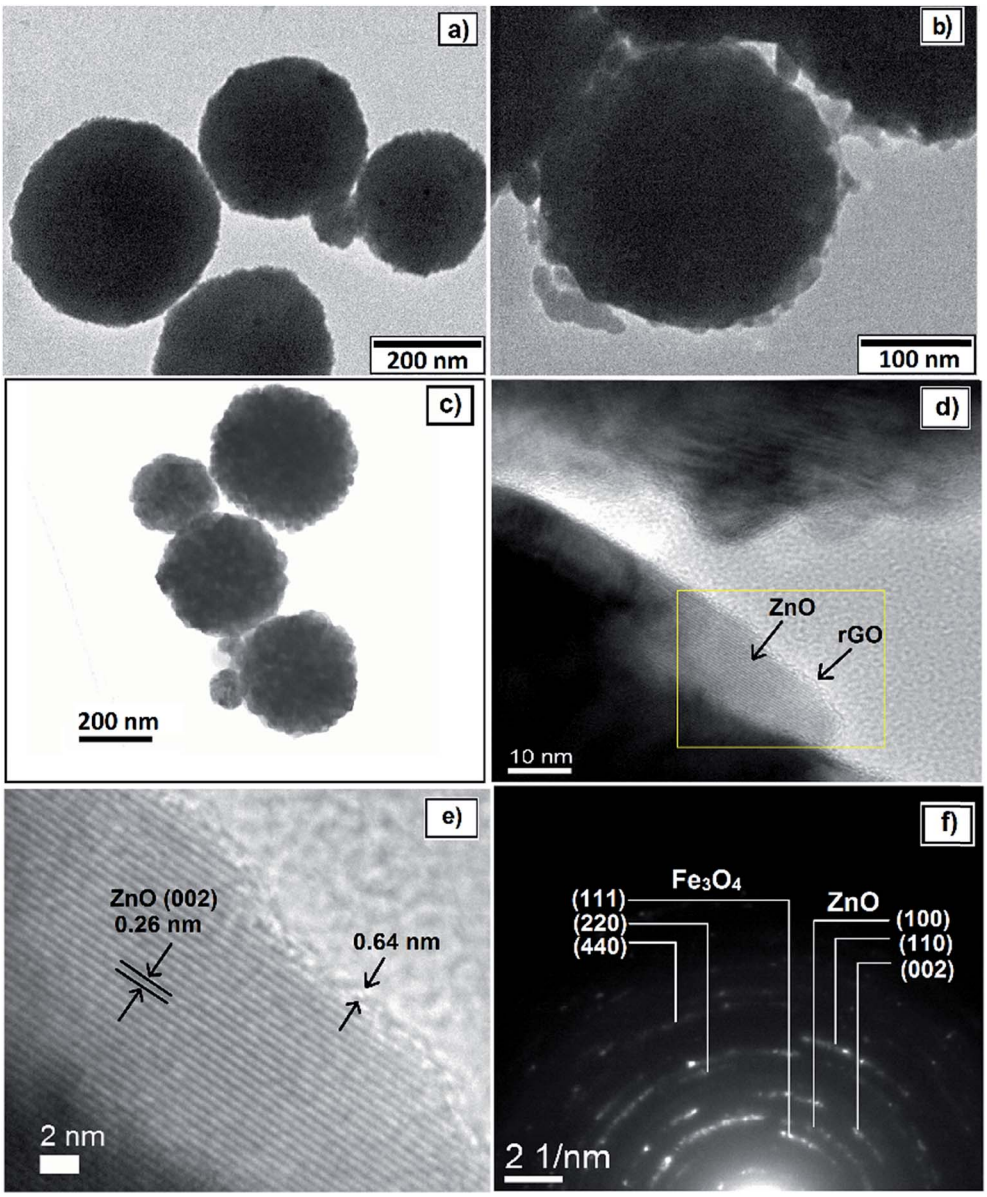

Fig. 5 TEM images of (a) Fe_3O_4, (b) CuZnO@Fe_3O_4, and (c) rGO@CuZnO@Fe_3O_4, (d) high magnification TEM of rGO@CuZnO@Fe_3O_4 showing crystalline ZnO and amorphous rGO zones, (e) HR-TEM image showing the lattice fringes and interplanar 2D spacing of ZnO and the thickness of the rGO layer, and (f) SAED pattern of rGO@CuZnO@Fe_3O_4 microspheres displaying the diffraction patterns of Fe_3O_4 and ZnO. Reproduced with permission from ref. 133 Copyright 2017 Elsevier.

displayed excellent photoactivity under visible light for methylene blue degradation. To exploit the advantages of the core–shell morphology and better charge carrier mobility on rGO sheets, Kumar *et al.* prepared core–shell structured CuZnO@Fe_3O_4 microspheres coated with rGO (rGO@CuZnO@Fe_3O_4) for visible light mediated CO_2 reduction.[133] The TEM images of the nanoparticles showed coated rGO as an amorphous zone on crystalline ZnO (Fig. 5). The oxide layer (mainly Fe_3O_4) present on the surface of the Fe_3O_4 core works as a semiconductor.[147] After the absorption of visible light, Fe_2O_3 can transfer photogenerated charges in the conduction and valence bands of ZnO, while Cu acts as an electron capturing agent to facilitate efficient transfer on rGO sheets. The band structure of such a nanocomposite was also suitable for water splitting and 45.5 μmol g^{-1} cat hydrogen was evolved as a by-product.

Reduced graphene oxide can also act as an electron transport mediator in Z-scheme photocatalytic systems. For example, a Z-scheme heterojunction photocatalyst, consisting of $BiVO_4$, Ru–$SrTiO_3$:Rh and rGO, in which $BiVO_4$ due to its more positive valence band facilitates water oxidation and $SrTiO_3$:Rh due to its more negative conduction band promotes proton reduction, exhibited a significantly enhanced photocatalytic water splitting rate (Fig. 6).[42] It has been found that for photoreduced graphene oxide (PRGO), the rates of hydrogen and oxygen evolution are much higher than those of hydrazine mediated chemically reduced graphene oxide. This fact can be explained on the basis of the higher hydrophobicity of PRGO, which facilitates better

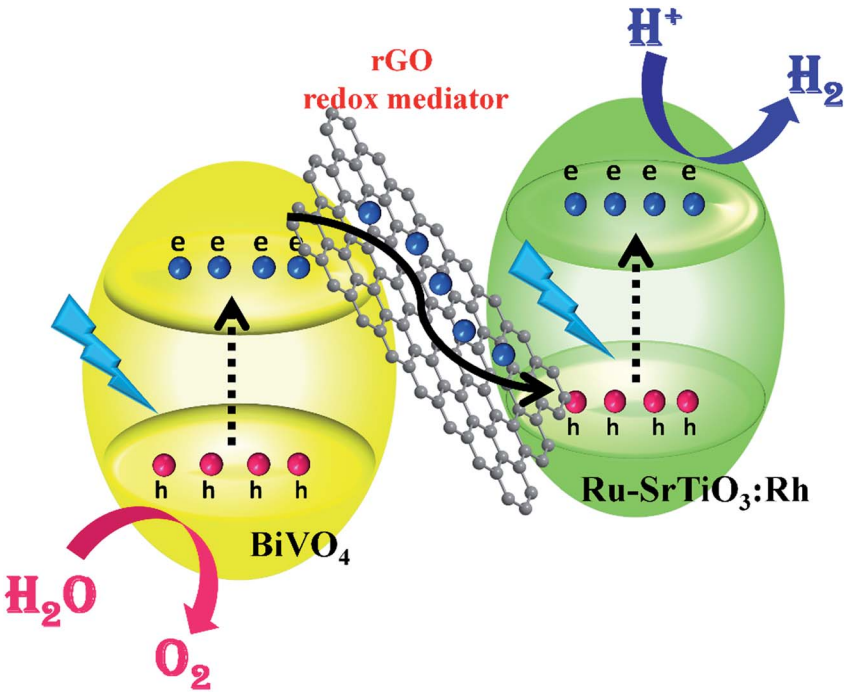

Fig. 6 Two photon Z-scheme overall water splitting on the $BiVO_4$–Ru–$SrTiO_3$:Rh photocatalyst. $BiVO_4$ can oxidize water to O_2 by photogenerated holes due to its positive valence band, but cannot reduce protons. The Ru–$SrTiO_3$:Rh composite can reduce protons due to its negative conduction band, but cannot oxidize water. The composite of $BiVO_4$ and Ru–$SrTiO_3$:Rh photocatalysts can sustain overall water splitting by two photons. $BiVO_4$, after photoexcitation, transfers electrons to the valence band of Ru–$SrTiO_3$:Rh, which upon second excitation reach the conduction band of Ru–$SrTiO_3$:Rh. Reduced graphene oxide serves as a solid-state redox mediator by facilitating electron transfer from the conduction band of $BiVO_4$ to the valence band of Ru–$SrTiO_3$:Rh. Adapted with permission from ref. 42.

transfer of electrons from the O_2 evolving catalyst to the H_2 reduction catalyst. Using PRGO as the electron mediator, H_2 and O_2 yields of 11 and 5.5 μmol h^{-1}, respectively, and an associated turnover number (TON) of 3.2 over 24 h were achieved.

3. Graphene oxide as a finite band gap semiconductor for water splitting

Graphene is known as a zero band gap material. However, the oxidation of graphene to graphene oxide (GO) transforms it into a semiconductor. The oxidation of graphene to GO adds several oxygen carrying functionalities, which break the conjugated π-system of graphene due to the transformation of some sp^2 carbons into sp^3 carbons.[148] Due to the larger electronegativity of oxygen, the carbon skeleton of GO becomes positive and GO behaves like a p-type material.[149] The presence of conducting sp^2 and non-conductive sp^3 domains on the GO sheets leads to the creation of a band gap, which depends on the extent of oxidation of the material. So by tuning the oxidation level, the band gap of GO can be controlled. Yeh *et al.* were the first to demonstrate that GO can split water into hydrogen and oxygen.[75] The band gap of GO was determined to be between 2.4 and 4.3 eV, depending on the oxidation level and this band gap was wide enough to meet the criterion of water splitting (1.23 V). The negative conduction band afforded a hydrogen yield of 280 μmol after 6 h of visible light irradiation, while using methanol as a sacrificial donor, the yield of hydrogen increased to 17 000 μmol after 6 h irradiation (Fig. 7).

GO can also achieve CO_2 reduction due its sufficiently negative conduction band (−0.79 V *vs.* NHE) and positive valence band (+2.91 V *vs.* NHE) to facilitate water oxidation for producing the required protons.[150] The decoration of GO sheets with Cu nanoparticles further enhances the photo-efficiency due to charge capture by Cu metal.[151] Due to oxidation, several surface defects generated on GO act as charge-recombination sites and decrease the photocatalytic performance of GO for water splitting. The treatment of GO with ammonia at elevated temperature can repair these defects by the removal of epoxy and carboxyl groups, and through the introduction of various nitrogen functionalities, *i.e.*, quaternary, pyridinic, and pyrrolic groups on the graphene sheets. Furthermore, the band gap of GO can be reduced due to the overlapping of π-orbitals of N and C and the delocalization of electrons at higher energy, so the position of the HOMO gets slightly uplifted. The back oxidation of nitrogen doped graphene oxide with a strong oxidizing agent ($KMnO_4$ + H_2SO_4) generates sheets having p-doped domains (due to the presence of O on sp^3 C), n-doped domains (due to the presence of N) and interfacial channels (due to sp^2 carbon). Yeh *et al.* showed that N-doped graphene oxide quantum dots (NGO-QDs), due to the presence of N and O atoms, behave like a p–n heterojunction and the conjugated sp^2 carbon skeleton acts as a charge transporting tunnel (Fig. 9).[76] The band gap of NGO-QDs was 2.2 eV and linear potential scans demonstrated CBM and VBM values

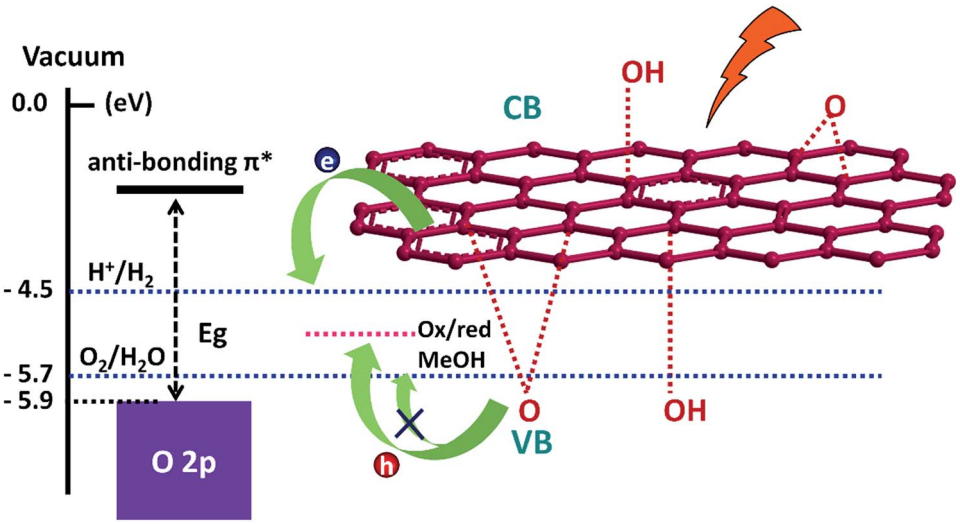

Fig. 7 Band diagram of GO showing the conduction band (CB) and valence band (VB) positions relative to proton reduction and water oxidation. The CB of GO has a higher overpotential than the level of H_2 generation and photogenerated electrons are transferred to the solution phase for proton reduction. The holes in the VB of GO are annihilated by the hole scavenger (methanol) instead of O_2 generation from water oxidation due to the higher reduction potential of methanol than water. The top-of-valence energy level was obtained using density functional theory for GO with 12.5% O coverage, and the levels for H_2 and O_2 generation were obtained from the literature. Adapted with permission from ref. 75.

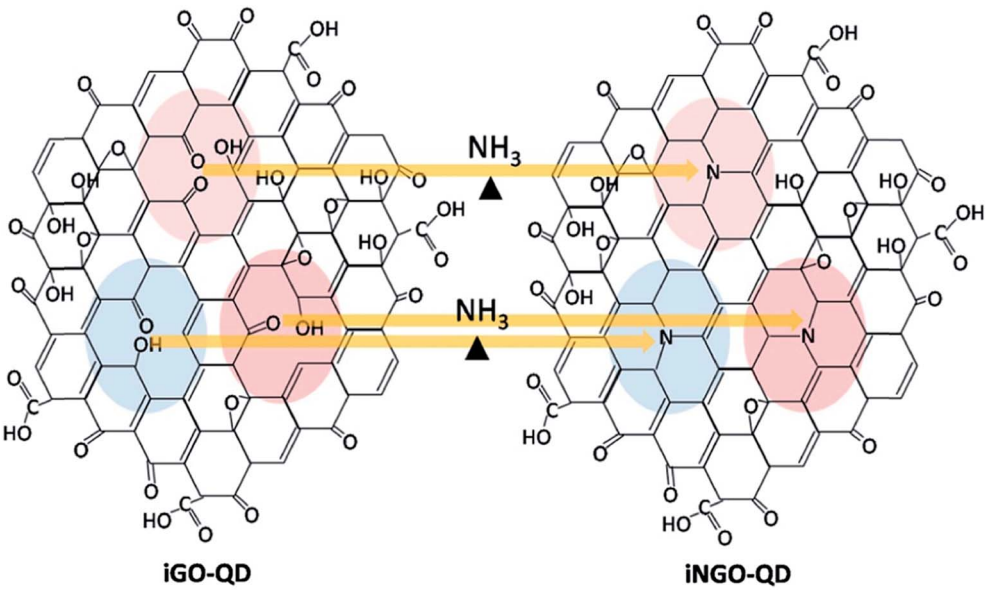

Fig. 8 Repairing of vacancy defects in iGO-QDs by hydrothermal ammonia treatment which introduces various nitrogen functionalities in the iNGO-QDs. Reproduced with permission from ref. 152 Copyright 2015 Elsevier.

of approximately −0.85 and 1.35 eV (*vs.* Ag/AgCl), respectively, which validates the overall water oxidation capability. Furthermore, by changing the oxidant that governs the concentration of oxygen on the sheets, the p-type character and band edge position can be controlled. For example, by using HNO_3 as an oxidant for the oxidation of nitrogen-doped graphene (NG), the CBM (−0.8 V *vs.* Ag/AgCl) and VBM (+1.4 V *vs.* Ag/AgCl) levels were found to shift slightly (Fig. 8).[152]

Chen *et al.* demonstrated that the hydrothermal treatment of nitrogen-doped graphene oxide quantum dots (NGO-QDs) in ammonia transforms some pyridinic/pyrrolic groups into amino/amide groups (Fig. 10a).[153] The obtained amino/amide groups due to the non-planar nature can donate their lone pair of electrons to the π-conjugated network of graphene (Fig. 10b). The intramolecular transfer of nitrogen lone pairs in the network of sheets induces spin orbital coupling effects and reduces the energy difference between singlet (S1) and triplet (T1) orbitals, resulting in singlet–triplet splitting. This facilitates easy and efficient S1 → T1 transfer through intersystem crossing (ISC) of excited electrons.[154] The PL intensity of

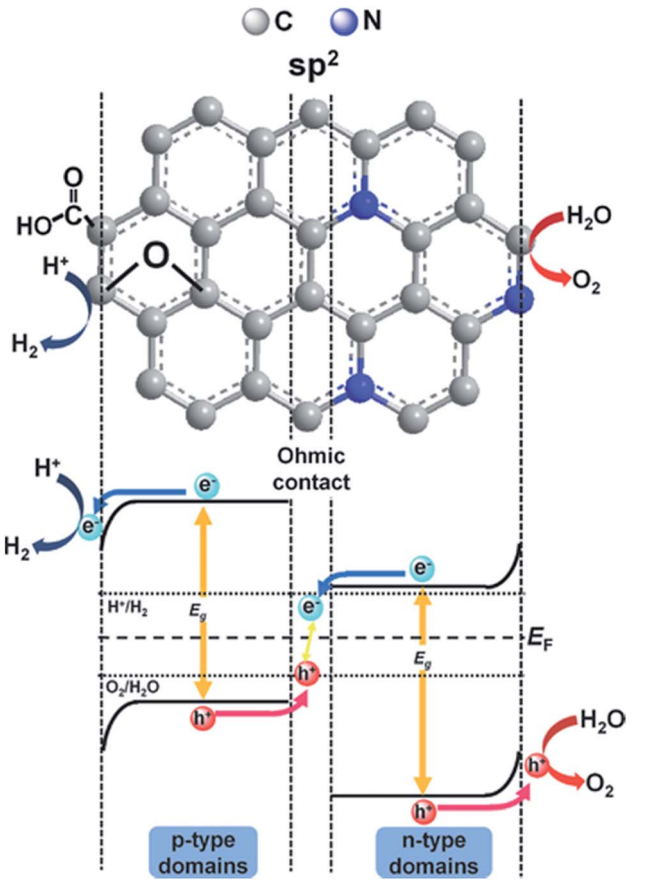

Fig. 9 Schematics of p–n heterojunction formation on NGO-QDs during hydrothermal treatment of GO-QDs with NH_3. Reproduced with permission from ref. 76 Copyright 2014 Wiley-VCH.

ammonia treated nitrogen-doped graphene dots (A-NGODs) was decreased, suggesting that the removal of some oxygen functionalities and slow electron–hole recombination on the N-doped basal plane took place. Time-resolved PL decay curves of GODs, NGODs, and A-NGODs showed average lifetimes of excited states of 0.43, 0.54, and 1.5 ns, respectively. The longer lifetime of excited species in A-NGODs validates the S1 ↔ T1 transition of electrons through intersystem crossing (Fig. 11). By using (A-NGODs) as a catalyst, a 21% quantum yield can be achieved by using Pt as a co-catalyst in a water/triethanolamine mixture.

Like reduced graphene oxide, many composites of GO with metals (Cu, Ag, Au, Pt, *etc.*), semiconductors (TiO_2, $BiVO_4$, CdS, *etc.*), metal complexes (Ru, Co, Ir, *etc.*) are reported for enhancing the hydrogen evolution rate. The surface of GO provides the opportunity for strong interaction with metal, metal oxide nanoparticles and other substrates which work synergistically by facilitating charge transport, increasing absorption and surface area to achieve overall water splitting. The GO/TiO_2 composite was found to be an effective photocatalyst for hydrogen production because unpaired π electrons on GO can interact with Ti atoms on the surface of TiO_2 to generate Ti–O–C bonds, which extend light absorption in the visible region.[155–157] Due to the formation of a p–n heterojunction in GO/TiO_2 hybrids, better charge separation can be achieved which facilitates efficient water splitting (Fig. 12).

4. Sensitization of graphene-based materials

Due to the presence of an ample number of functional groups, GO provides an opportunity for covalent functionalization of metal complexes on its surface. Metal phthalocyanine and ruthenium complexes have been successfully anchored onto GO; however due to the presence of mainly epoxide functionalities on basal planes, lower loading was achieved. Therefore, efforts are underway for the covalent functionalization of basal planes by breaking epoxide bonds followed by the attachment of metal complexes. Kumar *et al.* demonstrated the attachment of phthalocyanines (Co,[158] Cu[159] and Fe[160]) and polypyridyl metal complexes (Ru[161,162]) on GO sheets with high loading by functionalizing epoxide moieties with chloroacetic acid and subsequent covalent attachment of homogeneous metal complexes for various applications, *i.e.*, CO_2 photoreduction, thiol oxidation, CO_2 to DMF formation, *etc.* It has been found in all cases that the photocatalytic performance of metal complex-loaded GO was increased manifold due to better charge injection in the conduction band of GO. Hexanuclear Mo metallic clusters ($[Mo_6Br_{14}]^{2-}$),[163] which are very photoactive and able to transfer multiple electrons in photocatalysis processes, were also immobilized on GO by taking advantage of the labile nature of their apical halogen atoms, which can be easily replaced by oxygen present on graphene sheets (Fig. 13).[164]

The sensitization of undoped and doped graphene with metal complexes or organic dyes further improves the visible light absorption as well as photocatalytic performance.[165] A copper complex immobilized on N-doped graphene (GrN_{700}–CuC) was found to be a good photocatalyst for CO_2 reduction to methanol (1600 μmol g_{cat}^{-1}) in water/DMF/triethylamine solution under visible light irradiation.[166] Wang *et al.* reported covalently immobilized manganese phthalocyanine to reduced graphene oxide by using a glycinato linker (Fig. 14).[167] The synthesized photocatalyst was used for the production of hydrogen from water in the presence of platinum. The yield of hydrogen was found to be 8.59 μmol mg^{-1} during this study. Metal-free dyes due to their inexpensive nature, degradability and wide absorption range have proven to be good photosensitizers for the hydrogen evolution reaction. Eosin Y, an organic acidic dye, binds with reduced graphene oxide (EY–RGO) through hydrogen bonding and π–π interaction to produce a photocatalytic material for hydrogen generation in the presence of Pt nanoparticles decorated on the surface of reduced graphene oxide (Fig. 15).[168,169] The presence of both Pt and RGO was crucial for the production of hydrogen and by using a EY–RGO/Pt photocatalyst the rate of hydrogen production reached was about 10.17 μmol h^{-1}, corresponding to an apparent quantum yield (AQY) of 4.15% at 420 nm. The superior photocatalytic activity was assumed to occur due to efficient charge separation on the surface of RGO and subsequent

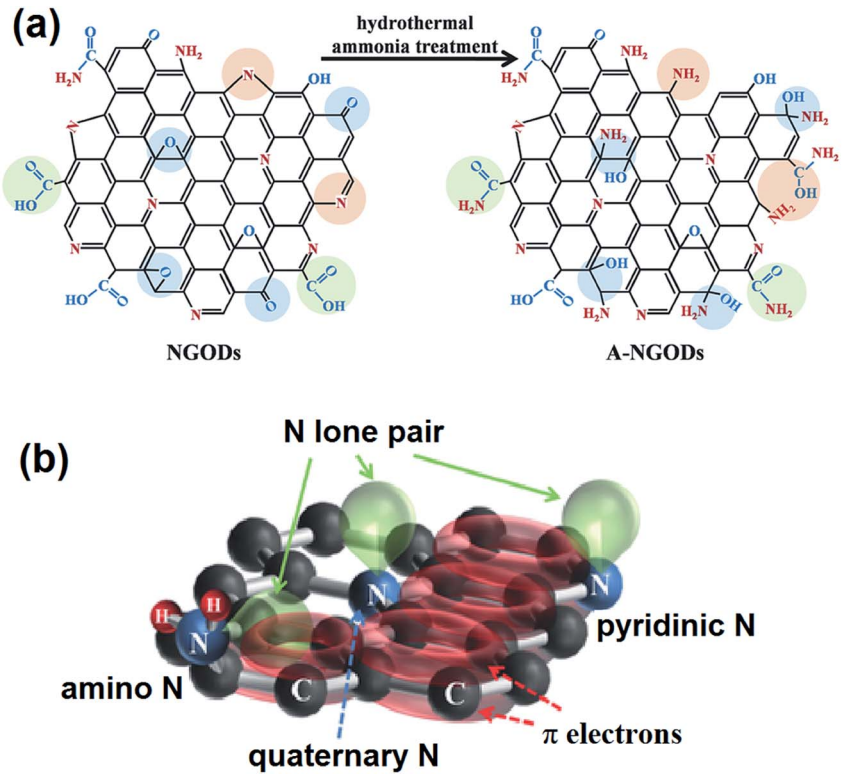

Fig. 10 Schematic of (a) hydrothermal cleavage of pyridinic and pyrrolic rings in NGODs to create epoxy, carbonyl, and carboxylic groups for decorating the basal plane and periphery of the A-NGODs with amino and amide groups. (b) An orbital diagram showing the overlaps of the nitrogen lone pair orbital in nitrogen functionalities with the aromatic π-system. The more effective overlap of the lone pair orbital of amino ($-NH_2$) groups in A-NGODs with the aromatic π-system of sheets than the planar pyridinic-N atom lone pair orbital has been revealed. Reproduced with permission from ref. 153 Copyright 2016 Wiley-VCH.

capture by Pt nanoparticles. Furthermore, to maximally harvest the solar spectrum, EY and Rose Bengal (RB) were grafted on the surface of RGO (ER-G/Pt) and the rate of hydrogen evolution increased significantly. By using ER-G/Pt, the hydrogen production rate was increased up to 36.7 μmol h^{-1}, corresponding to a quantum yield (QY) of 9.4% at a 420 nm wavelength.[79]

5. Doped graphene photocatalysts

Although graphene is a zero band gap semimetal in which quasiparticles obey a linear dispersion relationship between the energy and momentum, *i.e.*, the conduction band touches the

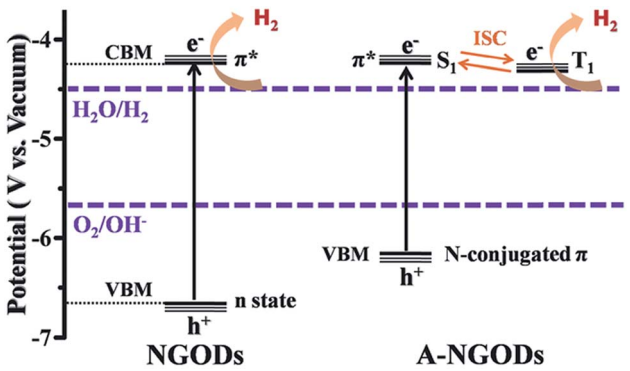

Fig. 11 The band structure diagram of NGODs and A-NGODs shown relative to the redox potential of water for H_2 and O_2 generation. The small energy difference between singlet (S_1)–triplet (T_1) splitting of the CBM of A-NGODs facilitates the $S_1 \leftrightarrow T_1$ transition of electrons *via* ISC, which prolongs the lifetime of the excited electrons for H_2 production from water reduction. Reproduced with permission from ref. 153 Copyright 2016 Wiley-VCH.

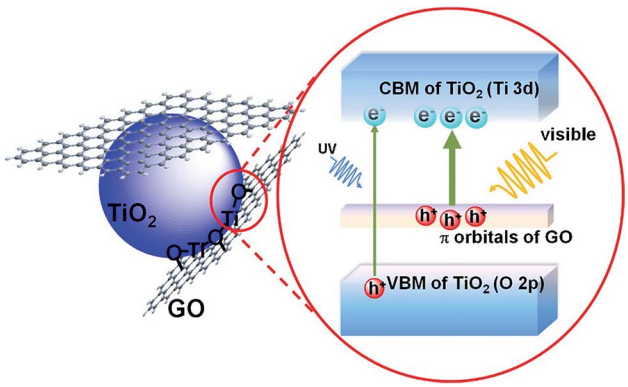

Fig. 12 The band gap narrowing of TiO_2 due to Ti–O–C bonding between unpaired π-electrons on GO and surface Ti atoms of TiO_2, which facilitates the light absorption profile of TiO_2. Reproduced with permission from ref. 157 Copyright 2013 Elsevier.

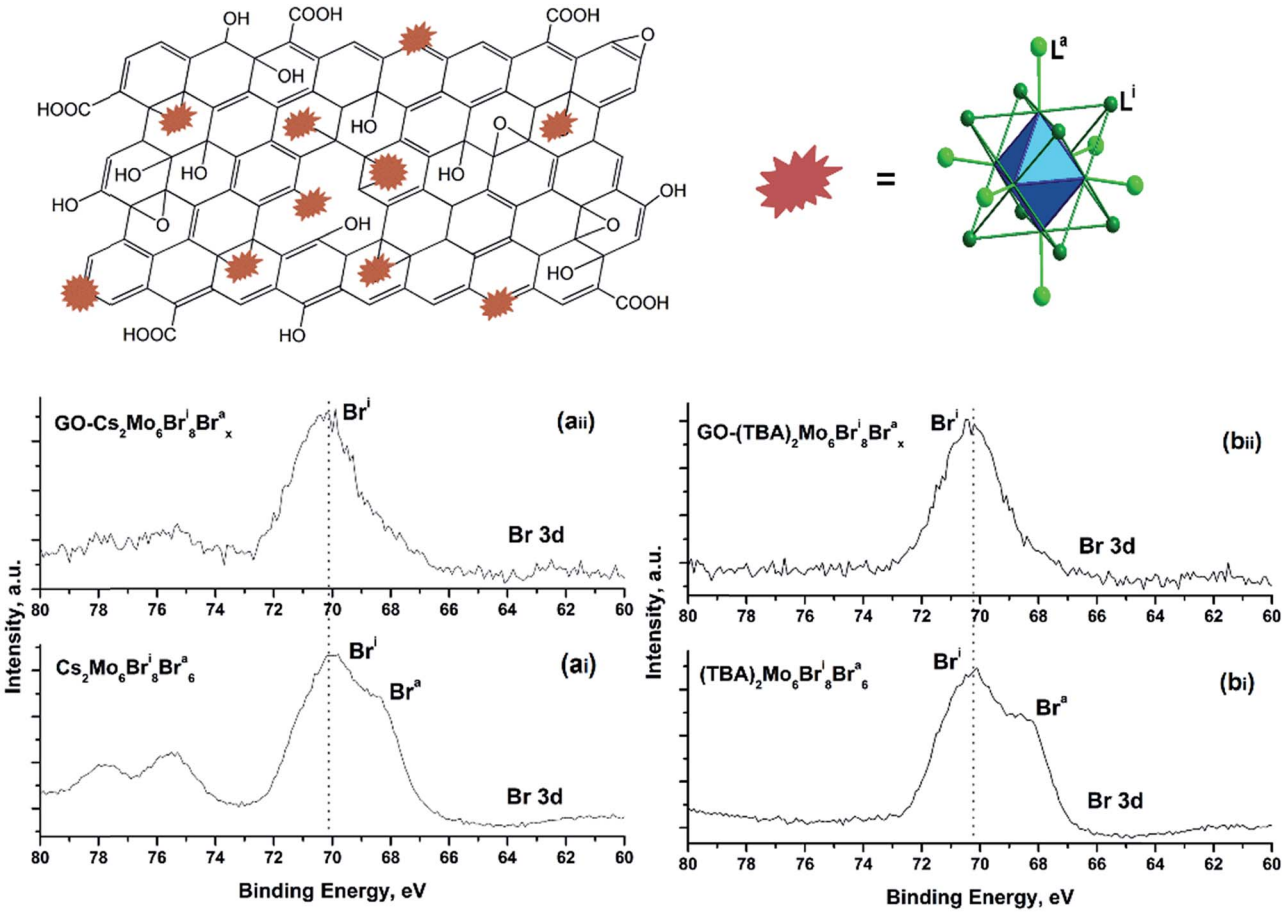

Fig. 13 A schematic illustration of Mo_6 clusters decorated on GO nanosheets; the right side image depicts the structure of the Mo_6 cluster exhibiting the positions of inner and apical ligands. High resolution XPS spectra in the Br_{3d} region for $Cs_2Mo_6Br_8^iBr_6^a$ (ai) and GO-$Cs_2Mo_6Br_8^iBr_x^a$ (aii) composites, and $(TBA)_2Mo_6Br_8^iBr_6^a$ (bi) and GO-$(TBA)_2Mo_6Br_8^iBr_x^a$ (bii) composites showing a decrease in the signal intensity of apical bromine atoms, suggesting their attachment to GO by the replacement of bromine atoms with oxygen on GO. Reproduced with permission from ref. 164 Copyright 2015 Elsevier.

valence band at a single Dirac point, there are various routes to create a band gap in graphene (Fig. 16a). By lowering the size of graphene sheets, *i.e.*, nanoribbons and nanodots, a band gap is opened in graphene due to the quantum confinement effect. Furthermore, the number of sheets is also an important parameter which influences the electronic environment of another sheet. The charge density on the edge of sheets can be increased in comparison to the basal plane. The presence of

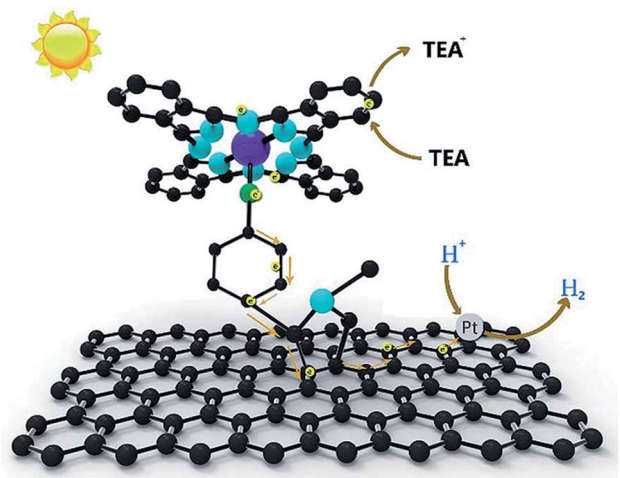

Fig. 14 Outline of the electron transfer from MnPc to a graphene sheet for hydrogen evolution. Reproduced with permission from ref. 167 Copyright Royal Society of Chemistry.

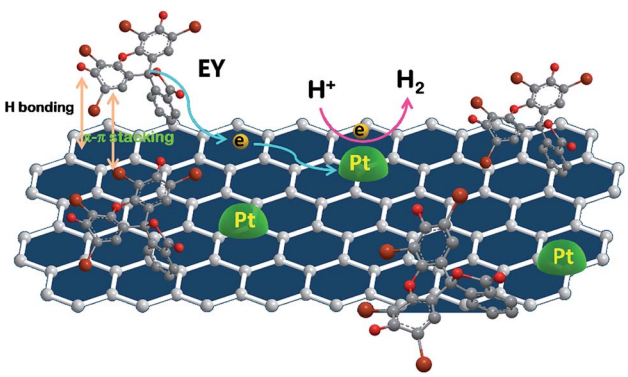

Fig. 15 Bonding of Eosine dye (EY) on rGO sheets through π–π interaction. EY transfers visible light photogenerated electrons to rGO sheets, which due to higher mobility increases charge separation. Electrons on rGO sheets are captured by Pt and used for hydrogen generation from water. Adapted with permission from ref. 168.

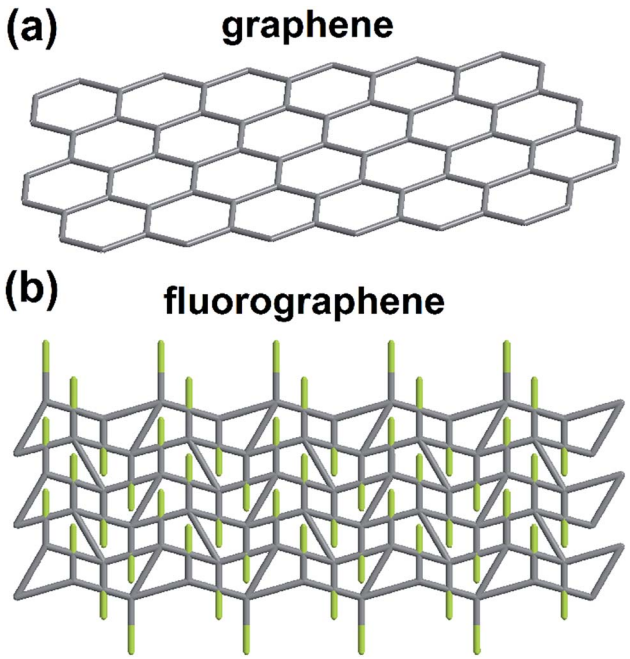

Fig. 16 Structure of (a) graphene sheets showing the planar sheets of sp^2 hybridized carbon atoms arranged in a hexagonal fashion, and (b) fluorographene sheets of sp^3 carbons atoms arranged in a chair conformation. Adapted from ref. 171.

defects like vacancies and dislocations also opens the band gap by inducing additional electronic states.[170] The introduction of various elements like H, O, N, F, *etc.*, also affects the electronic properties of sheets. For example, fluorographene, a 2D sheet of graphite fluoride, is an insulator and its band gap can be tuned by controlling the number of fluorine atoms (Fig. 16b).[171] The attachment of fluorine atoms to sp^2 hybridized carbon distorts the hybridization of carbon to sp^3 and shifts the Dirac point. Theoretical calculation revealed that the band gap of partially fluorinated graphene (from $C_{32}F$ to C_4F) can be tuned from 0.8 to 2.9 eV.[172] However, experimental results showed an optical gap >3.8 eV (Fig. 17).[173] Partially chlorinated and brominated graphene counterparts have also been reported.[174] The fluorographene provides an opportunity for further functionalization of graphene with high selectivity. Cyano groups were introduced in a scaffold of the graphene skeleton by the replacement of fluorine atoms and the resulting cyanographene possesses high negative charge as revealed by zeta potential measurements.[175] The replacement of F atoms in fluorographene by hydroxyl groups transforms graphene into a room temperature organic magnet and the magnetic properties can be tailored depending on the F/OH ratio.[176] In addition, several covalent functionalization approaches have been utilized to form various functional groups such as –SH, –OH, alkyl, *etc.*, on the surface of graphene.[177–179]

Tailoring the structure of pristine graphene by substitution with heteroatoms like B, N, P, F, *etc.*, influences the charge distribution on the sheets and represents an effective way to modify the electronic, surface, optical and electrochemical properties. The dopant atoms can either work as donors or acceptors, depending on their electronegativity with respect to the carbon atom. Various heteroatoms like N, B, and P have been introduced into the graphene skeleton by using different precursors. Among them N doping has been found to show the best results due to the higher energy level of the N_{1s} orbital, which uplifts the energy level of the newly hybridized orbital. N-doping contributes mainly three kinds of nitrogen to the

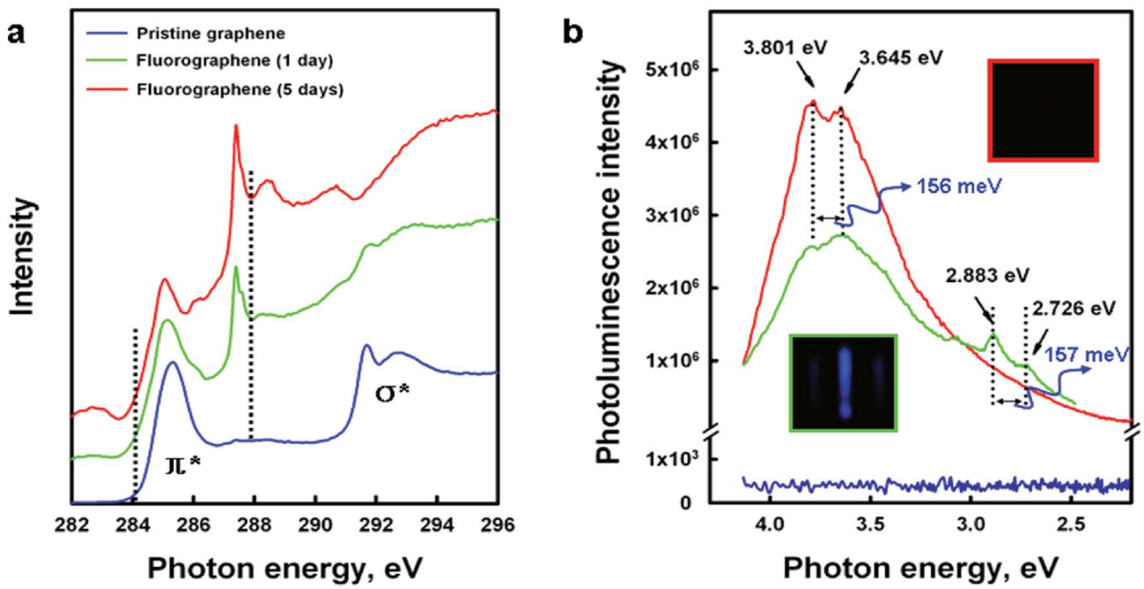

Fig. 17 The opening of the band gap in fluorographene. (a) NEXAFS spectra of pristine graphene and fluorographene with two different contents of fluorine. The dashed lines at 284.1 and 287.9 eV mark the leading edges of the π* resonance for the pristine and fluorinated samples, respectively. (b) The PL emission of the pristine graphene and fluorographene dispersed in acetone using 290 nm (4.275 eV) excitation at room temperature. The optical images in the inset show the blue PL emission, which persists for approx. 30 s after the excitation laser is turned off. (Reproduced with permission from ref. 173 Copyright 2011 American Chemical Society).

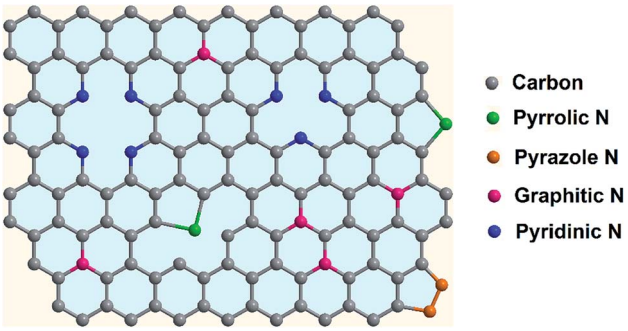

Fig. 18 Structure of N-doped graphene showing various types of N atoms according to bonding configuration. Adapted with permission from ref. 182.

graphenic structure: (1) pyridinic nitrogen, (2) quaternary nitrogen, and (3) pyrrolic nitrogen (Fig. 18).[180] Pyridinic nitrogens due to their position and availability of their lone pairs in the π orbital can participate in conjugation and increase the charge density of sheets; the Fermi level shifts above the Dirac point, distorts the symmetry of the graphene sub-lattice and creates a band gap in the N-doped sheets.[181] The value of the band gap is strongly dependent on the amount of nitrogen; by manipulating the concentration of nitrogen atoms, the band gap can be tuned.

N-doped graphene can be synthesized by various methods such as CVD, arc discharge method, and the thermal treatment of GO or rGO with nitrogen rich sources like ammonia, amines, hydrazine hydrate, urea, melamine, nitrogen, *etc.*[184] The most commonly used nitrogen source is ammonia even though the nitrogen content with ammonia treatment remains low (Fig. 19). Numerous composite materials such as Co/Co_9S_8 (ref. 185) with doped-graphene have been utilized for photocatalytic applications, *i.e.*, dye degradation, water splitting, solar cells, *etc.* Like N-doping, P-doping also induces band gap opening in graphene and can afford water splitting. In a recent report, 1.3 at% P-doped graphene was synthesized by thermal annealing of graphene with phosphoric acid and showed improved capacitance and cycling stability.[186] Biological carbon precursors modified with phosphoric acid can also generate P-doped graphene. For example, phosphoric acid modified alginate, after thermal annealing, gives P-doped graphene having high P content (17.16 at% for (P)G-1).[187] The band gap of P-doped graphene was estimated to be 2.85 eV and afforded 282 μmol g^{-1} h^{-1} of H_2. Some doped-graphene sheets demonstrate enhanced electrocatalytic performance comparable to that of precious Pt metal.[188,189] The doping of graphene with two dopant atoms (with reverse electronegativity like B and N) can accumulate synergistic effects to boost electrocatalytic performance in the oxygen reduction reaction (ORR).[190–192] However, most of the reports focused on the use of doped graphene for the ORR

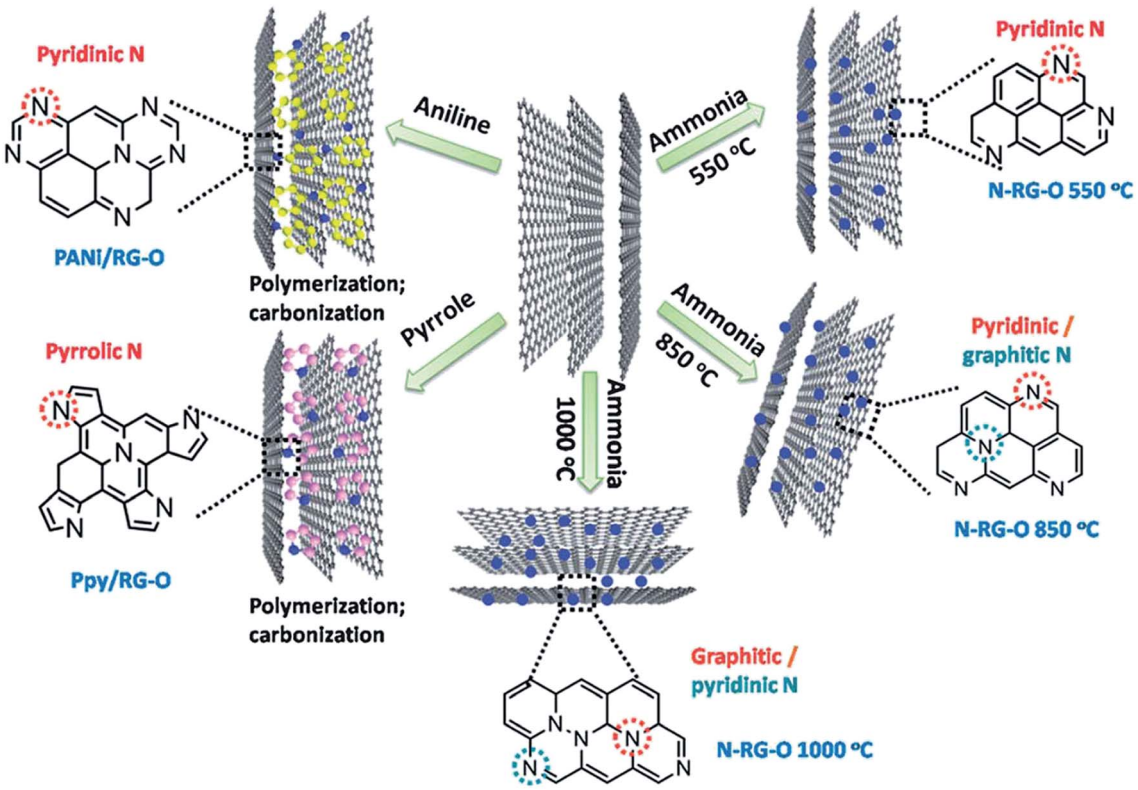

Fig. 19 Schematic diagram for the preparation of N-doped graphene with different N states. N-RG-O 550, 850, and 1000 °C were prepared by annealing of GO powder at temperatures of 550 °C, 850 °C, and 1000 °C in the presence of NH_3. PANi/RG-O and Ppy/RG-O were prepared by annealing of PANi/G-O and Ppy/G-O composites at 850 °C. Reproduced with permission from ref. 183 Copyright 2012 Royal Society of Chemistry.

and only a few reports are available for the hydrogen evolution reaction (HER). In this avenue, theoretical calculations showed that N- and P-co-doped graphene should be the best choice for the HER due to down shifting of the valence band, which may result in the highest HER activity over various singly doped and co-doped graphene materials. To achieve this goal, N- and P-co-doped graphene (N,P-graphene-1) was prepared by annealing of melamine (nitrogen source), triphenylphosphine (P source) and GO (graphene oxide sheets) in a 10 : 10 : 1 mass ratio under argon at 950 °C for 3 h. The N,P-doped graphene-1 displayed a 10 mA cm^{-2} HER current density at an overpotential of ~420 mV, which was much lower than that of single atom doped N- and P-graphenes.[193] For the doping process, ionic liquids can also be used as a source of heteroatoms and they also provide porosity to materials. For example, thermal annealing of polyaniline-coated GO and ammonium hexafluorophosphate (NH_4PF_6) produced nitrogen, phosphorus, and fluorine tri-doped graphene with a porous structure.[194] In this process, NH_4PF_6 serves as a source of heteroatoms as well as a soft template and its degradation produced gases, which provided porosity to the material. The metal free N-, P-, and F-tri-doped graphene multifunctional catalyst furnished hydrogen and oxygen gas with a production rate of 0.496 and 0.254 μl s^{-1}, respectively.

The OER is the main constraint in the water splitting reaction, which requires noble metal oxides such as IrO_2 or RuO_2 to overcome the sluggish kinetics of the OER. As an alternative, $NiCo_2O_4$ is a suitable choice over these noble metals due to its low cost and wide abundance. The performance of $NiCo_2O_4$ can be further improved by hybridization with graphenic materials.

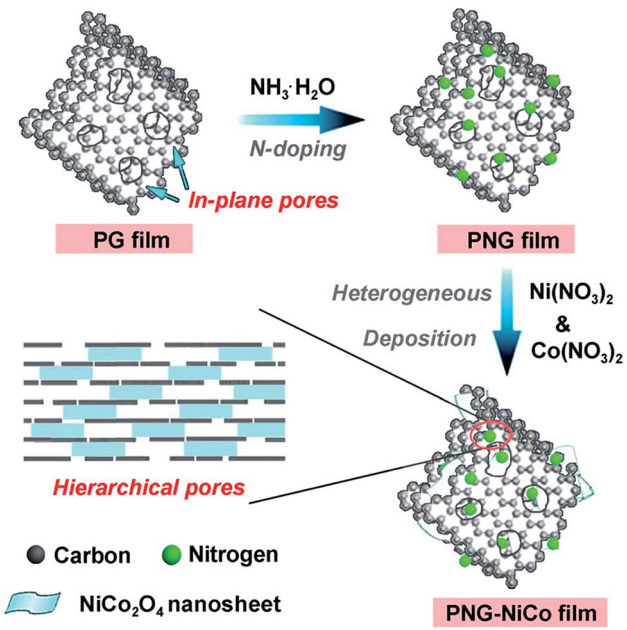

Fig. 20 Fabrication of N-doped graphene–$NiCo_2O_4$ 3D hybrid catalyst (Notations PG, PNG and PNG-NiCo signify porous graphene, porous N-doped graphene, and porous N-doped graphene–$NiCo_2O_4$ hybrid, respectively). Reproduced with permission from ref. 195 Copyright 2013 American Chemical Society.

In this avenue, Chen *et al.* reported on the synthesis of a 3D N-doped graphene $NiCo_2O_4$ nanocomposite by using in-plane porous graphene and subsequent doping and controlled growth of $NiCo_2O_4$ for an enhanced OER (Fig. 20).[195]

The pyrolysis of carbonaceous materials at an elevated temperature under an inert atmosphere gives defect-rich graphenic carbon and use of an additional nitrogen source or the precursor itself can produce N-doped carbon. Due to the presence of a band gap, high surface area, better light absorption and easy synthesis from earth abundant materials, doped carbon represents an interesting alternative to replace graphene materials in photocatalytic applications. By choosing appropriate precursors, the amount of the dopant can be controlled in the samples. For the synthesis of doped carbon materials, various carbon sources rich in heteroatoms can be utilized. Biomass rich in nitrogen content also provides opportunities for the synthesis of derived doped carbon from cheap and environmentally benign sources.[196] Similar to heteroatom co-doped graphene, the co-doping of carbon with different heteroatoms creates variable band gaps and numerous active sites on the surface, which lead to the enhancement of catalytic and photocatalytic performance.[197] For example, the carbonization of melamine (N source), glucose (C source) and sulphuric acid (S source) produced N-, S-doped carbon exhibiting a high surface area.[198] Due to heteroatom doping, several sites are evolved on the surface of doped carbon and serve as active sites for various catalytic reactions. For example, N-, P-, and S-doped hollow carbon shells with a very high surface area were synthesized by thermal treatment of poly(cyclotriphosphazene-*co*-4,4′-sulfonyldiphenol) (C, N, P, and S-doping source) and ZIF-67 (source of the carbon framework).[199] In recent years, metal organic frameworks (MOFs) have become popular for the synthesis of heteroatoms, particularly N-rich carbon.[200,201] The advantages of carbon derived from MOFs are high N content, high porosity, periodicity of defects and possibility of manipulation of the band gap, which make them excellent metal free photocatalytic and electrode materials for hydrogen and oxygen evolution. Zeolitic imidazolate framework (ZIF) based MOFs are widely utilized for the synthesis of N-rich carbon materials. Zhao *et al.* reported the synthesis of nitrogen-rich carbon (ZNG) by the carbonization of ZIF-8 at 800–1000 °C.[202] The hydrogen evolution rate from a sample prepared at 1000 °C carbonization temperature was found to be 18.5 μmol h^{-1} under visible light in the presence of triethanolamine and 3 wt% Pt co-catalysts. This catalyst showed excellent photocatalytic performance even in the absence of Pt with a hydrogen evolution rate of ~5.8 μmol h^{-1}. CoP nanoparticle embedded N-doped hollow carbon nanotubes/polyhedra derived from a core–shell structured ZIF-8@ZIF-67 MOF displayed increased water splitting efficiency.[203] Several nanocomposite materials of semiconductors and doped carbon have been employed for various applications particularly electrochemical and photochemical hydrogen evolution.[204–207] For example, CoO nanoparticles embedded in a N-doped carbon layer were synthesized by thermal pyrolysis of polypyrrole-coated Co_3O_4 nanoparticles at 900 °C; this material exhibited excellent activity for the ORR and OER which was assumed to be

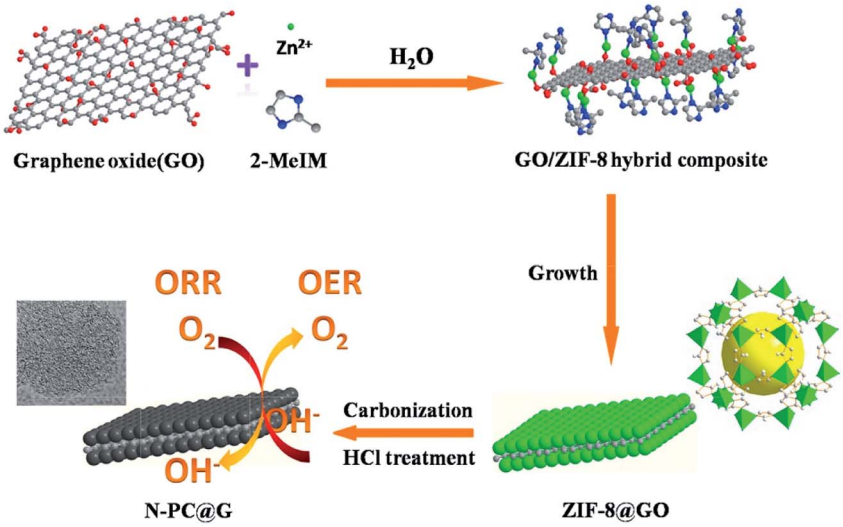

Fig. 21 Schematic illustration of the synthesis steps of sandwich-like structured N-doped porous carbon@graphene (N-PC@G). Reproduced with permission from ref. 211 Copyright 2016 Elsevier.

due to the porous nature of doped carbon and synergistic interaction.[208] The main challenge in electrocatalytic water splitting is the replacement of the expensive noble metal platinum. Metal carbide (particularly Mo_2C) seemed to be an interesting alternative to Pt because of similar d-band electronic density, high electrical conductivity, and good hydrogen–adsorption properties. In this respect, ultra-small molybdenum carbide (Mo_2C) nanoparticles embedded in nitrogen-rich carbon Mo_2C@NC displayed remarkable catalytic activity and stability over a wide range of pH (pH 0–14) for the electrocatalytic HER.[209] The Mo_2C@NC produced hydrogen at a rate of 34.5 μmol h^{-1}, corresponding to 100% faradaic efficiency close to the theoretically achievable value. The dramatically high performance of this catalyst was believed to be due to the strong electron-withdrawing features of N dopants, which facilitated electron transfer in the direction $Mo_2C \rightarrow C \rightarrow N$, so that neighboring C atoms could act as donors and acceptors to provide active sites. Another report also demonstrated that Mo_2C embedded in N-doped carbon achieved better electrocatalytic water splitting performance.[210] The controlled synthesis of N-doped porous carbon sandwiched reduced graphene oxide (N-PC@G) was achieved by the pyrolysis of ZIF-8 sandwiched GO (Fig. 21). The structure obtained by maintaining a GO concentration of 0.02 g in reaction and thermal treatment at 900 °C afforded the highest surface area (1094.3 m^2 g^{-1}) and the obtained catalyst showed better OER and ORR activity due to better charge transport of holes generated in doped carbon on rGO sheets.[211]

6. Carbon nitride based photocatalysts for hydrogen evolution

Polymeric semiconductor materials such as polyaniline and polyparaphenylene[212] have been used for hydrogen production even though they absorb UV light and the associated quantum efficiency is too low. In recent years, carbon nitride, the oldest reported synthetic organic polymer, has re-emerged as a material of choice due to its specific chemical and physical properties such as a low band gap and a suitable band edge position for efficient water splitting, nontoxic nature, wide stability, easy

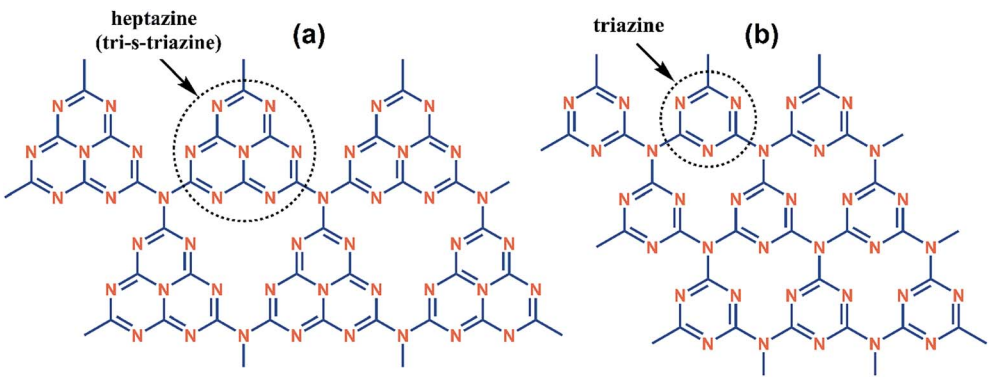

Fig. 22 Structure of graphitic carbon nitride based on (a) *s*-heptazine (gh-C_3N_4) and (b) *s*-triazine units (gt-C_3N_4). The *s*-heptazine network gh-C_3N_4 is about 30 kJ mol^{-1} more stable than gt-C_3N_4. Adapted with permission from ref. 213 and 214.

synthesis and processability.[87] In the world of 2D materials, carbon nitride competes with graphene because of a similar graphitic structure, high surface area, astonishing optical and chemical properties and ease of synthesis. Carbon nitride (C_3N_4) is a 2D polymeric semiconductor consisting of interconnected tri-*s*-triazine units *via* tertiary amines. Carbon nitride exists in several allotropic forms (C_3N_4, that is, α-C_3N_4, β-C_3N_4, cubic C_3N_4, pseudocubic C_3N_4, g-h-triazine, g-o-triazine, and g-h-heptazine) depending on the basic monomer unit and the pattern of linkage, which governs the morphology, crystallinity and even photoactivity. Graphitic carbon nitride possessing a layered graphite-type structure is the most stable form. Graphitic carbon nitride (g-C_3N_4) is either composed of triazine (C_3N_3) units in which case it is amorphous and less stable or tri-*s*-triazine (heptazine, C_6N_7) units, which results in a crystalline and more stable compound (Fig. 22). The synthesis of carbon nitride from its precursor always affords carbon nitride with a heptazine structure due to its higher stability. The continuous N-bridged tris-*s*-triazine ring structure gives rise to graphite type π-conjugated planar sheets. Due to the high degree of polymerization of tri-*s*-triazine units, g-C_3N_4 exhibits astonishing thermal stability (up to 600 °C) and chemical stability (stable in acidic and basic media). Triazine units containing amorphous carbon nitride (gt-C_3N_4) can be synthesized by the reaction of cyanuric chloride and lithium nitride.[213,214] Tri-*s*-triazine units containing carbon nitride frameworks can be isolated by the polycondensation of nitrogen rich precursors such as urea, cyanamide, dicyandiamide, thiourea, formamide, melamine, CCl_4/ethylene diamine, guanidine, *etc.* Due to alternate repetition of carbon and nitrogen in carbon nitride, it has a medium band gap of 2.7 eV and absorbs in the blue region (420–450 nm) of visible light. The position of the conduction band at −1.1 V (*vs.* NHE at pH 0) and valence band at +1.6 V (*vs.* NHE at pH 0) makes it a suitable candidate for water splitting (Fig. 23).[51,215,216]

Large scale production using urea provides an opportunity for the realization of a catalyst for future use; however mass loss is more important than with other precursors although it can be limited by condensation in closed systems or co-condensation in a cage of porous material such as silica.[217,218] The synthesis of carbon nitride materials from urea with a high g-C_3N_4 yield and variable band gap can also be achieved using eutectic molten alkyl halide salts.[219] The annealing temperature also controls the photoactivity of g-C_3N_4. Generally, most of the reports described the synthesis of carbon nitride at 550 °C. However, a report by Papailias *et al.* showed that a sample annealed at 450 °C was more photoactive than samples annealed at 550 °C for NO degradation.[220] It is proposed that polycondensation at a controlled temperature produces nitrogen vacancy defects, which prevent the intrinsic radiative decay of charges and populate the conduction and valence bands with more available electrons and holes, respectively.[221] A TiO_2/C_3N_4 composite, prepared at high calcination temperature (600 °C), was found to be optimal due to the creation of oxygen vacancies and Ti^{3+} defects, which promote Z scheme transition instead of direct transition.[222] Besides the annealing temperature, the annealing environment also influenced the photocatalytic performance of g-C_3N_4. g-C_3N_4 containing carbon vacancies and nanoholes, prepared by two step heating (i) at 650 °C under argon and (ii) at 550 °C in air, displayed a high H_2 evolution rate (5261 μmol h^{-1} g^{-1}) with a quantum efficiency of 29.2% at 400 nm.[223]

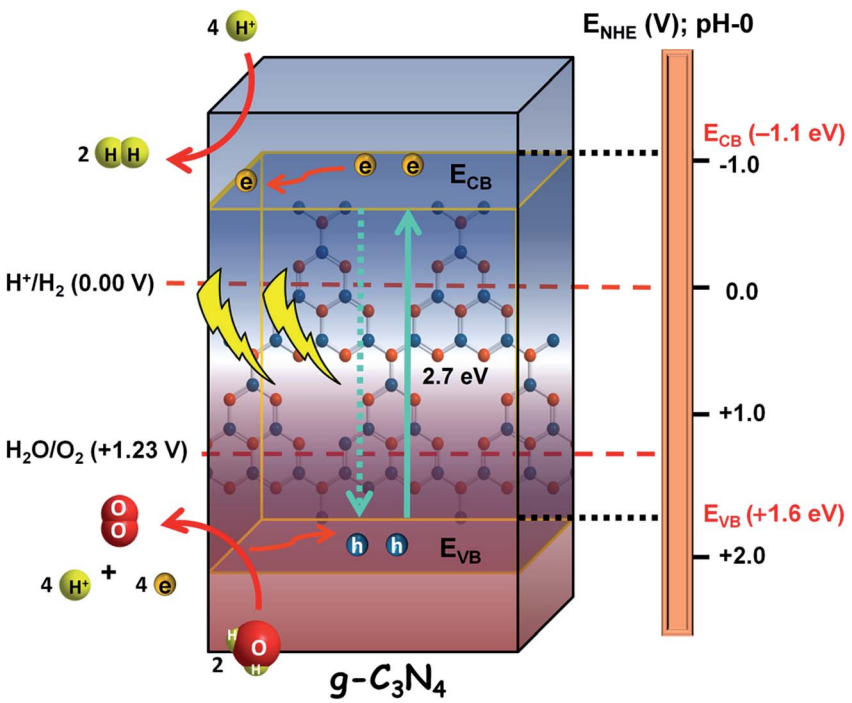

Fig. 23 Band structure diagram of g-C_3N_4 showing the positions of conduction and valence bands and relative oxidation and reduction potentials of water.

Interestingly, the deliberate introduction of defects into carbon nitride sheets improved the photocatalytic performance. Niu *et al.* reported that rapid heating (5 min) of carbon nitride at 650–700 °C followed by fast cooling promoted defects in the CN structure and the band gap was reduced to 2.17 eV which is low enough to absorb a large part of the visible spectrum.[224]

Furthermore, due to the band gap and presence of nitrogen-rich sites on carbon nitride, it can promote various oxidation and reduction reactions such as alkylation, oxidative coupling, hydrogenation (phenol to cyclohexanone), NO decomposition, oxygen reduction reaction (ORR), and CO_2 activation under metal-free conditions.[225–230] The presence of various kinds of nitrogen (especially pyridinic) in g-C_3N_4 makes it more electron-rich and provides active sites to facilitate base promoted nucleophilic reactions like the oxidation of alcohols to aldehydes by activating O_2,[231] transesterification of keto-esters,[232] and three component coupling (benzaldehyde, piperidine, and phenylacetylene) to propargylamine.[233] It is important to note here that the three component coupling reaction proceeds only in the presence of strong bases such as butyl-lithium, organo-magnesium reagents, or lithium diisopropylamide. Despite being a semiconductor, carbon nitride also suffers from the drawback of charge recombination and limited light absorption in the lower wavelength region, which restricts its photoactivity. Furthermore, due to a more reductive conduction band than the water reduction potential (0.00 V *vs.* NHE at pH 0), g-C_3N_4 showed excellent hydrogen evolution activity; in contrast, the valence band is relatively weakly oxidative, compared to the water oxidation potential (+1.23 eV), leading to low activity for oxygen evolution activity. Many efforts have been devoted to improving the performance of carbon nitride by adding various metals (Pd, Cu, Ru, Fe, Pt, and Ni), and inorganic semiconductors ($InVO_4$, Fe_3O_4, Cu_2O, TiO_2, $NaNbO_3$, $Mn_{0.8}Cd_{0.2}S$, Bi_2WO_6, ZnO, WO_3, $ZnCr_2O_4$, CoP, Co_2P, $CuCo_2O_4$, Ni_2P, WS_2, $BiPO_4$, MoS_2, In_2O_3, CeO_2, ZnS, *etc.*), graphene oxide, graphene, fullerene, carbon dots, organic polymers, metal complexes, metal free dyes, *etc.*[92,215,234–243] The composite materials of carbon nitride with semiconductors not only increase the photocatalytic efficiency by synergistic mechanisms, but also improve the photostability. For example, $AgPO_4$, an excellent oxygen evolving catalyst, suffers from the drawback of self-reduction to silver.[244] Furthermore, a positive conduction band edge comparable to the proton reduction potential and a tendency to make large particles make it inappropriate for hydrogen evolution. However, upon hybridization with g-C_3N_4, it becomes quite stable with better photoactivity due to the formation of heterojunctions and smaller particles. Yang *et al.* prepared a $AgPO_4$ and carbon nitride hybrid ($AgPO_4$/ECN400) by a two-step method using cyanuric acid and melamine as precursors of g-C_3N_4 and the subsequent growth of $AgPO_4$ by reaction of a Ag^+ ion source and $NaPO_4$.[245] The synthesized $AgPO_4$/ECN system was found to be very stable and exhibited excellent photocatalytic performance for rhodamine B (RhB) degradation and O_2 evolution. Previously proposed mechanisms

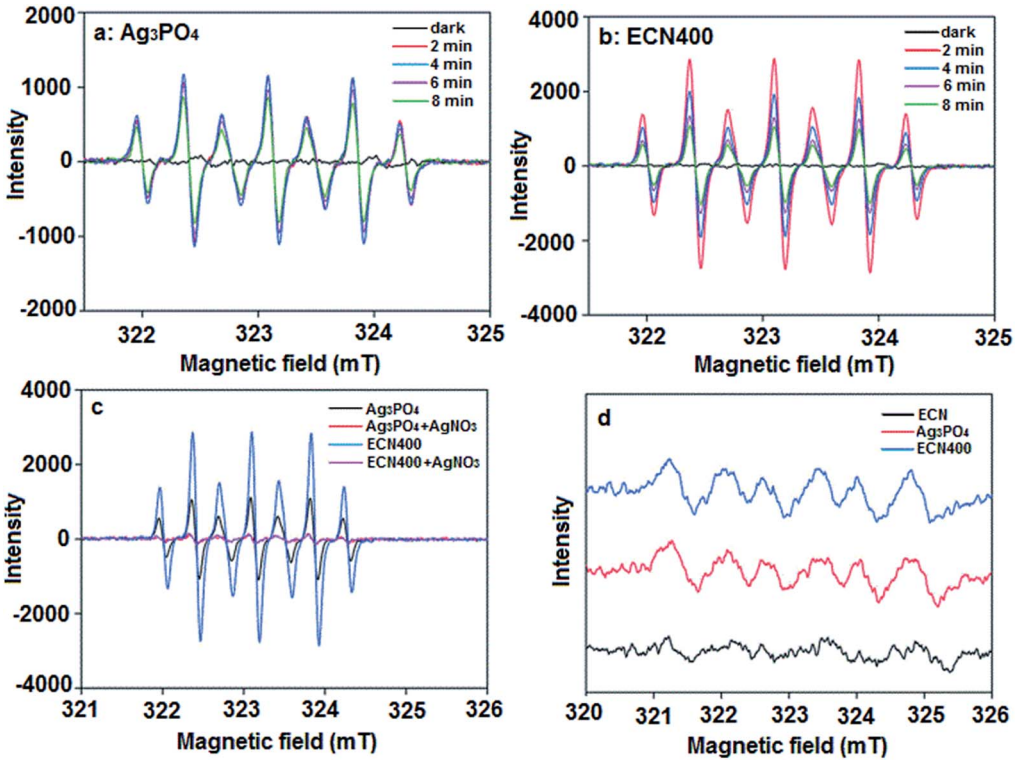

Fig. 24 ESR spectra of radical adducts trapped by DMPO in an (a) aqueous dispersion of Ag_3PO_4, (b) aqueous dispersion of ECN400, (c) Ag_3PO_4 and ECN400 in the presence or absence of $AgNO_3$, and (d) ECN, Ag_3PO_4, and ECN400 methanol dispersions. Reprinted with permission from ref. 245 Copyright 2015 Wiley-VCH.

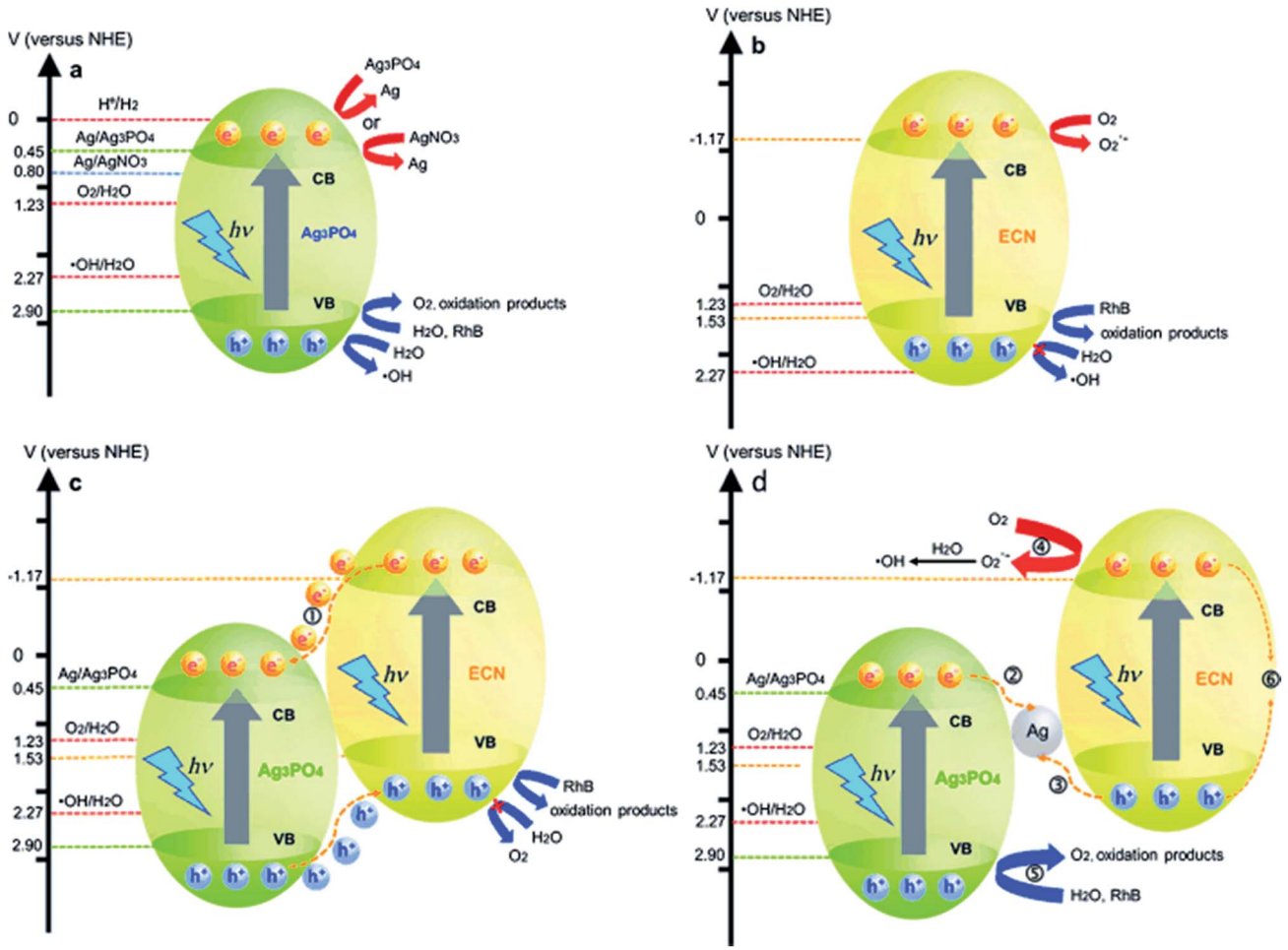

Fig. 25 Schematic for the energy-level diagram of (a) Ag_3PO_4 and (b) ECN, (c) conventional mechanism, and (d) proposed Z-scheme mechanism for charge transfer. The band-gap values of Ag_3PO_4 and ECN were estimated to be 2.45 and 2.70 eV, respectively. The E_{VB} of Ag_3PO_4 and ECN was calculated to be 2.90 and 1.53 eV *vs.* NHE, respectively, whereas their corresponding E_{CB} was 0.45 and −1.17 eV *vs.* NHE, respectively. Reproduced with permission from ref. 245 Copyright 2015 Wiley-VCH.

suggesting a transfer of electrons from the CB of g-C_3N_4 to the CB of $AgPO_4$ and holes from the VB of $AgPO_4$ to the VB of g-C_3N_4 were not convincing, due unfavorable charge transfer and inability of accumulated holes in the VB of g-C_3N_4 to facilitate dye oxidation and O_2 evolution.[246,247] The negligible O_2 yield and RhB degradation activity using pristine g-C_3N_4 are due to its inability to facilitate the water oxidation process. Dye degradation experiments by introducing benzoquinone (BZQ) (an $O_2^{\bullet-}$ radical scavenger), *tert*-butyl alcohol ($OH^\bullet$ scavenger) and Na_2-EDTA (direct hole scavenger) revealed that $O_2^{\bullet-}$ was the dominant active species responsible for dye degradation. The investigation of the reaction mechanism with the help of ESR using 5,5-dimethyl-1-pyrroline-N-oxide (DMPO) as a trap agent showed the signals of DMPO–$OH^\bullet$ and DMPO–$O_2^{\bullet-}$ adducts, which in turn indicate the generation of $OH^\bullet$ and $O_2^{\bullet-}$ radicals under visible light irradiation with increasing signal intensity during the duration of irradiation. Interestingly, for $AgPO_4$ and ECN400 in the presence of $AgNO_3$, the signals from DMPO–$OH^\bullet$ disappeared after irradiation due to the generation of $OH^\bullet$ radicals and the intensity of the signal increased during the irradiation time, suggesting that fewer $OH^\bullet$ radicals were generated at an earlier stage; the absence of an ESR signal in the dark demonstrated that the presence of light is crucial. Additionally, the signals of DMPO–$O_2^{\bullet-}$ adducts were observed in pristine $AgPO_4$, ECN400 and the $AgPO_4$/ECN400 hybrid confirming the generation of superoxide radicals (Fig. 24). On the basis of these results, a Z scheme mechanism was proposed for higher photocatalytic performance. Initially, under visible light irradiation, electrons generated in the CB of carbon nitride are transferred to the CB of $AgPO_4$. These electrons reduce Ag^+ to Ag and the system turns into a three phase Ag_3PO_4/Ag/ECN system. Subsequently, electrons generated in the conduction band of $AgPO_4$ and holes generated in the valence band of carbon nitride recombined at the Ag interface, resulting in electrons in the conduction band of g-C_3N_4 (ECN400) and holes in the valence band of $AgPO_4$ (Fig. 25). The electrons in the CB of ECN400 can reduce O_2 to an $O_2^{\bullet-}$ radical which is transformed in to a $^\bullet OH$ radical after the abstraction of a proton from water, while holes in the VB of $AgPO_4$ were utilized for the direct oxidation of RhB and water. The proposed Z scheme was further supported in follow up studies.[248]

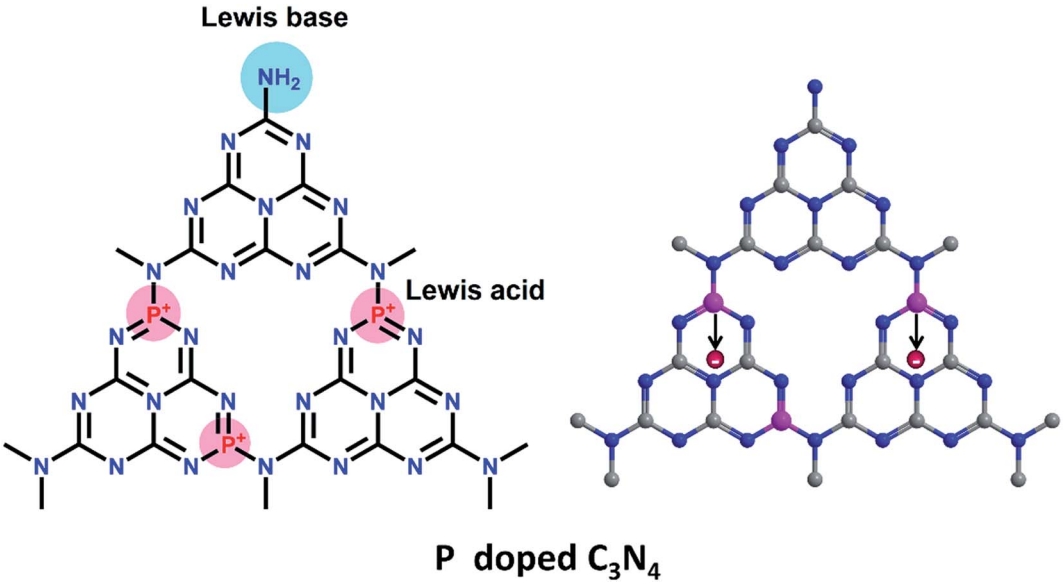

Fig. 26 Chemical structure of P-doped C_3N_4 showing Lewis acid and Lewis base sites created by P doping and $-NH_2$ groups present on the periphery. The pyridinic nitrogen due to the presence of lone pairs also provides basic sites. Reproduced with permission from ref. 250 Copyright 2015 Royal Society of Chemistry. The structure on the right side depicts the electron transfer from a P atom to the π-conjugated network responsible of the band gap reduction of P-doped C_3N_4.

7. Doped-carbon nitride for photocatalysis

The doping of carbon nitride with heteroatoms is appealing because heteroatoms can influence charge density on sheets, which affects visible light absorption properties. Among various possible doping agents, ionic liquids having a heteroatom counter ion are considered the best candidates for the doping of carbon nitride because of high boiling points, negligible vapor pressure and high stability (up to 400 °C) so that they can participate in the C–N condensation step during polymerization. Phosphorous doping is appealing because the replacement of C in C_3N_4 sheets with electron rich P atoms will lead to the addition of a lone pair of electrons in the sheet's π conjugated system (Fig. 26). Zhang *et al.* synthesized phosphorus-doped carbon nitride by heating dicyandiamide and $BmimPF_6$ (1-butyl-3-methylimidazolium hexafluorophosphate) precursors.[249] ^{31}P NMR analysis of the developed materials indicated that some of the carbon atoms were replaced by P atoms. Additionally, XPS analysis revealed 3.8 at% of phosphorus in P-doped carbon nitride. Due to P doping, the band gap of P-doped C_3N_4 was reduced down to 1.60 eV, so that it can absorb almost in the whole visible spectrum. The band gap value of materials strongly depends on the amount of P doping and can be tuned by controlling the precursor concentration. It is important to note here that the precursor of the doping material should be stable and participate in the polycondensation step. For example, P-doped carbon nitride can also be synthesized using relatively inexpensive hexachlorotriphosphazene $(NPCl_2)_3$ as a source of phosphorus and guanidinium hydrochloride (GndCl) as a precursor for the C_3N_4 framework.[250] The synthesized catalyst showed better performance for visible light promoted hydrogen evolution in the presence of a Pt co-catalyst and triethanolamine as a sacrificial donor. The P-doped C_3N_4 synthesized using 10 wt% hexachlorotriphosphazene at 550 °C (P10-550) afforded the highest rate of hydrogen evolution (50.6 μmol h^{-1}), which was 2.9 fold higher than that of pure g-C_3N_4. Similarly, a P-doped nanotubular structure was prepared using melamine and sodium pyrophosphate (phosphorous atom source) followed by heating at 500 °C and then used for hydrogen production from water splitting.[251] The activity of the doped catalyst can be further improved by adding metal nanoparticles like nickel nanoparticles. Indeed, it has been demonstrated that P-doped carbon nitride decorated with Ni nanoparticles (Ni@g-PC_3N_4) displayed better photoactivity than P-doped C_3N_4 for visible light driven reduction of nitro compounds.[252] P-doped C_3N_4 was synthesized by using $BmimPF_6$ as a phosphorus source and dicyandiamide as a heptazine framework source;[249] Ni@g-PC_3N_4 was prepared by introducing specific wt% of Ni nanoparticles into dicyandiamide and $BmimPF_6$ precursors followed by heating at 550 °C. 5 wt% loading of Ni nanoparticles was found to be optimum to achieve the complete transformation of nitroaromatics to anilines within 8 h of visible light irradiation.

Similar to P-doping, boron and fluorine co-doped mesoporous carbon nitride (CNBF) was synthesized by thermal polymerization of dicyandiamide and 1-butyl-3-methylimidazolium tetrafluoroborate ($BmimBF_4$) in which $BmimBF_4$ itself serves as a source of B and F but also as a soft template for improving the surface area.[253] The CNBF catalyst promotes the selective transformation of cyclohexane to cyclohexanone under thermal and oxidative conditions. Although boron doping of carbon nitride gave good results for organic transformation, these structures were found to be inactive for water splitting. This has been assigned to the detrimental effect

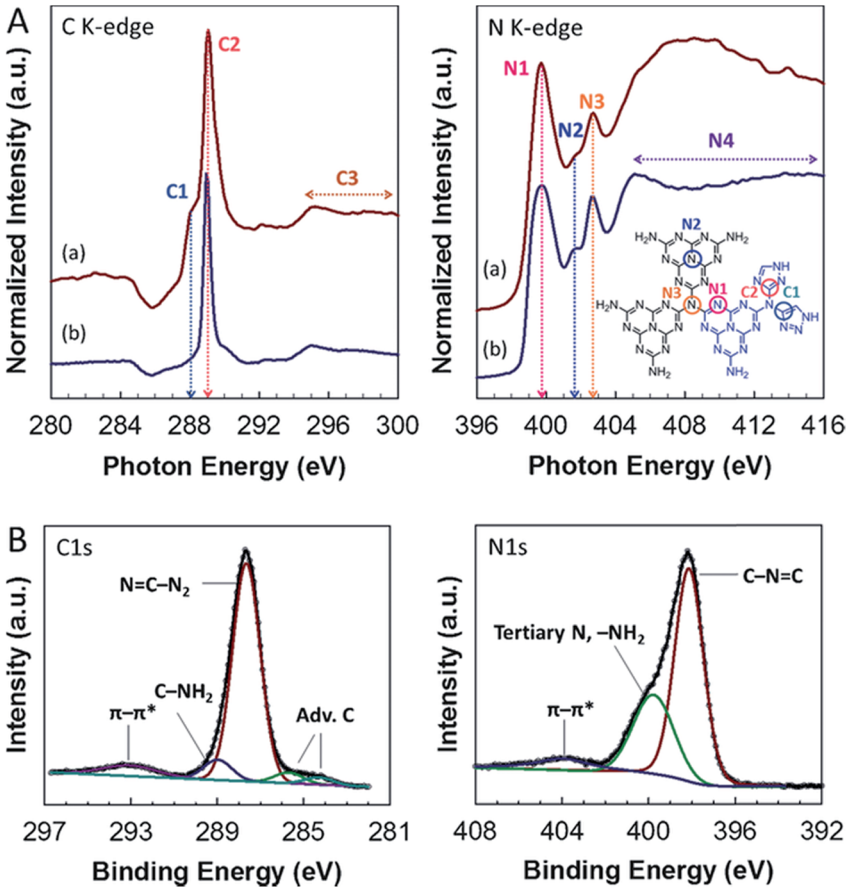

Fig. 27 (A) Carbon K-edge and nitrogen K-edge NEXAFS spectra of (a) MCN-8 and (b) g-C_3N_4 (inset: proposed molecular structure). (B) High-resolution XPS of MCN-8 in C_{1s} and N_{1s} regions. Reproduced with permission from ref. 260 Copyright 2017 Wiley-VCH.

of dopant debris, which behave as deep trap-sites and can also unfavorably distort the electronic structure. However, the careful selection of dopant precursors can overcome this problem. For instance, B-modified g-C_3N_4 synthesized by thermal annealing of low cost urea and Ph_4BNa exhibited good hydrogen activity for the hydrogen evolution reaction.[254] Boron acts as a Lewis acid, while nitrogen atoms on sheets work as intrinsic Lewis base sites which generate frustrated Lewis pairs and favor the fast splitting of light-generated excitons.[255] So, these Lewis pairs on sheets facilitate the formation of hydrogen adatom centers on the acid–base sites, which promote the surface activity of the catalyst.[256] Apart from $BmimBF_4$, ammoniotrihydroborate (BNH_6) and boric acid $B(OH)_3$ have also been used as boron sources for the synthesis of B-doped carbon nitride.[257,258] Nitrogen-doped carbon nitride was also prepared by using EMIM-dca (1-ethyl-3-methylimidazolium dicyanamide) and 3-MBP-dca (3-methyl-1-butylpyridine) ionic liquids.[259] The carbon to nitrogen ratio of g-C_3N_4 is 3 : 4 and the main challenge is to increase the nitrogen content, which may potentially reduce the band gap. To achieve this goal, Vinu *et al.* prepared

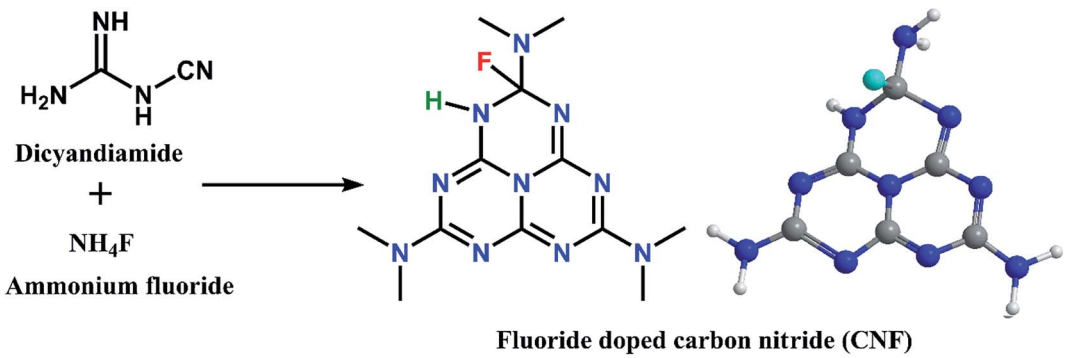

Fig. 28 Synthesis outline of F-doped carbon nitride (CNF) showing out of plane F atoms attached to corner C atoms. Reproduced and redrawn with permission from ref. 262 Copyright 2010 American Chemical Society.

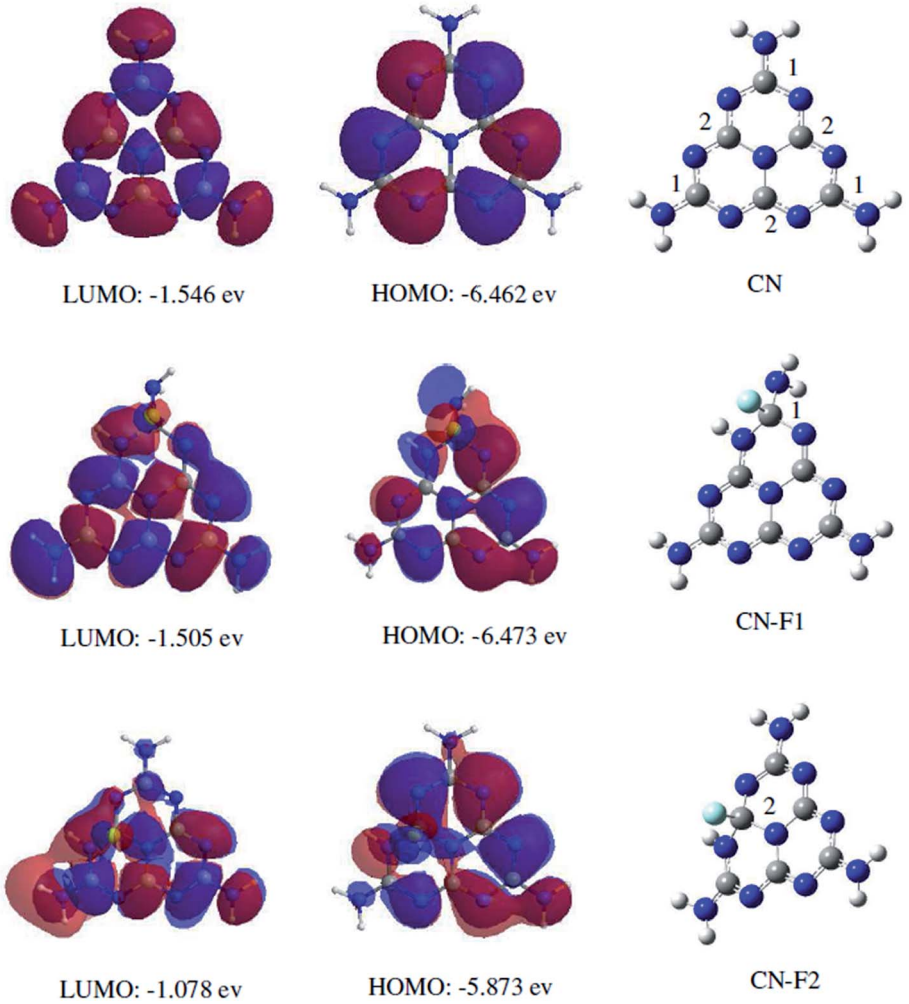

Fig. 29 The atomic orbital diagram of the Frontier molecular orbitals and optimized geometry of C_3N_4 and F-doped C_3N_4 (CNF) having F atoms attached in an out of plane fashion on corner carbon (CN–F1) and bay carbon (CN–F2). The CN–F2 has higher energy and displays more prominent band shifting. Reproduced with permission from ref. 262 Copyright 2010 American Chemical Society.

new nitrogen-rich carbon nitride (MCN-8) having a C_3N_5 stoichiometry by using 3-amino-1,2,4-triazole as a source of nitrogen (Fig. 27). Due to N-doping, the band gap of carbon nitride was reduced to 2.2 eV and the surface area was increased up to 296.7 m^2 g^{-1}.[260] The obtained catalyst was able to split water into hydrogen at a significant rate (801 μmol of H_2 under visible-light irradiation for 3 h) without the use of any external dopant. Furthermore, carbon nitride polymer with a high N stoichiometric ratio (C_3N_6) containing diaminotetrazine units has been reported by the same group for improved water splitting.[261]

Instead of the addition of expensive dopants, some cheap nitrogen and heteroatom precursors can provide doping elements in the polycondensation step. For example, fluorine-doped carbon nitride (CNF) can be synthesized by using NH_4F and dicyandiamide precursors (Fig. 28).[262] XPS and ^{19}F solid state NMR analysis confirmed the doping of fluorine (~3 at%) and theoretical calculation showed that the fluorine atom was attached to a carbon atom in an out of plane fashion. The attachment of F atoms to corner and bay carbon atoms shifts the LUMO and HOMO positions and modifies the redox properties in such a way as to promote heterogeneous photocatalysis (Fig. 29). The band gap value of CNF was determined to be 2.63 eV and the hydrogen evolution rate of the CNF catalyst using Pt as a co-catalyst from a water/triethanolamine mixture under visible light (λ > 420 nm) was 2.7 times higher than that of unmodified g-C_3N_4. A recent study demonstrated that the hydrothermal treatment of g-C_3N_4 with dilute HF does not lead to F doping. However, structural distortion was induced in the CN framework, which creates delocalized electronic states that affect the charge distribution pattern on CN sheets. Due to this distortion, the positions of the CB and VB were shifted toward negative potentials, which facilitate better hydrogen evolution.[263]

Carbon-rich carbon nitride polymer was also synthesized using a hydrothermal route by heating melamine and glucose. The –CHO and C–OH groups of glucose react with melamine to give a more conjugated carbon extended network. Due to the presence of a more conjugated network, the electrical conductivity and visible light absorption capacity were enhanced

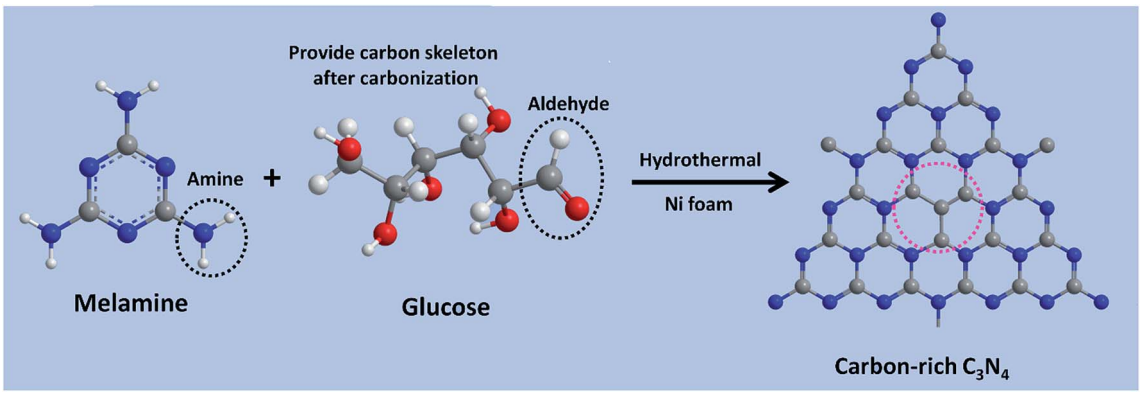

Fig. 30 Schematic illustration of the polymerization process of melamine (MA) and glucose in a water solution to carbon-rich C_3N_4. Reproduced and redrawn with permission from ref. 264 Copyright 2015 Royal Society of Chemistry.

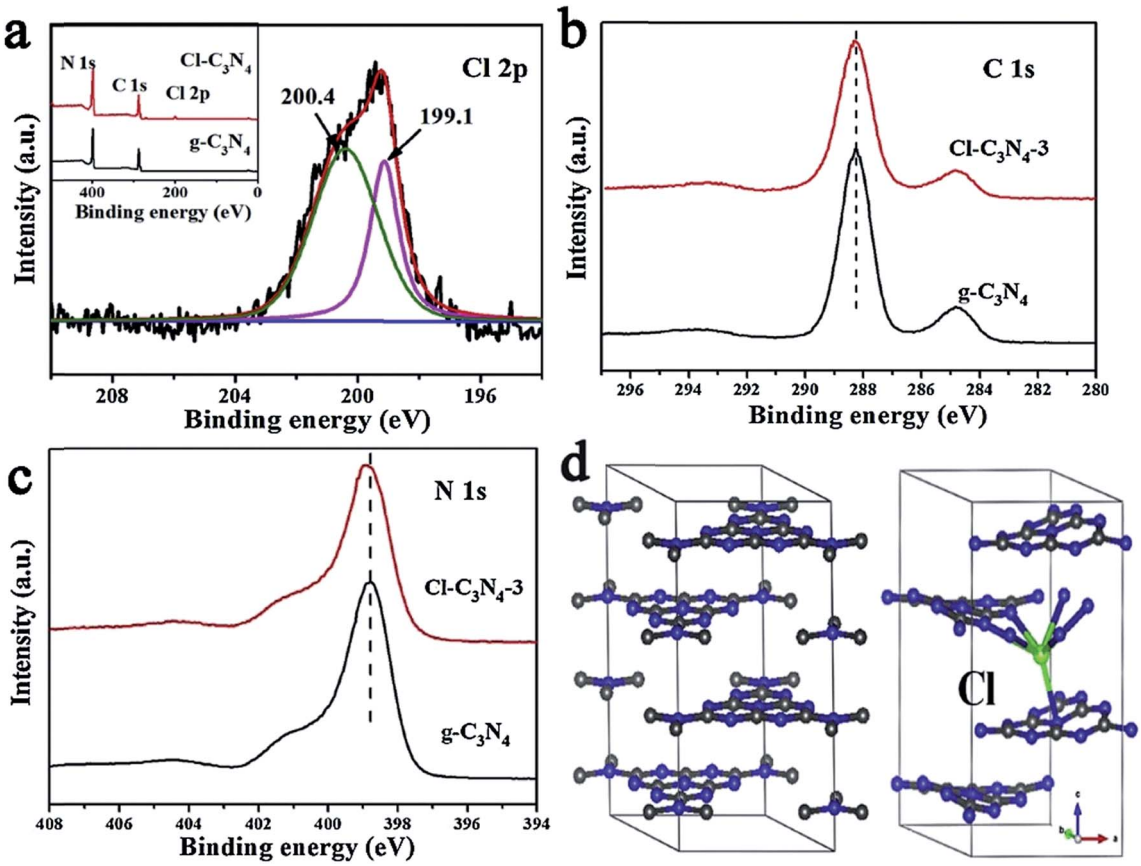

Fig. 31 High resolution XPS of Cl-doped g-C_3N_4 (a) in the Cl_{2p} region; inset shows the survey scan, (b) HR-XPS of g-C_3N_4 and Cl-doped g-C_3N_4 in the C_{1s} region and (c) N_{1s} region, and (d) crystal structure of pristine g-C_3N_4 and Cl-doped g-C_3N_4. Reproduced with permission from ref. 270 Copyright 2017 Elsevier.

(Fig. 30).[264] Post calcination doping with carbon using glucose has also been reported for hydrogen evolution (H_2 production rate of 40.37 μmol h^{-1}).[265] In another study, Che *et al.* demonstrated that the introduction of a carbon ring in between C_3N_4 framework (C ring)–C_3N_4 improved electron–hole pair separation due to an extended π network along with better visible light absorption to achieve a high photocatalytic rate of hydrogen production (371 μmol g^{-1} h^{-1}).[266] Similar to the carbon ring introduction in the carbon nitride framework, melamine was also introduced into CN sheets by thermal annealing at high temperature, resulting in the removal of some nitrogen and formation of conjugated topological carbon nitride (TCN) with

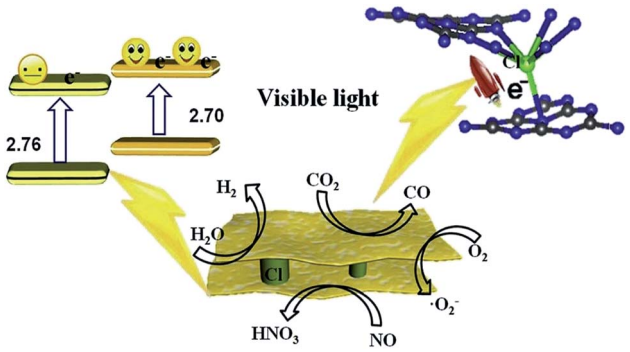

Fig. 32 Sketch of the visible light-assisted charge transfer and photocatalytic mechanism of Cl intercalated g-C_3N_4. Reproduced with permission from ref. 270 Copyright 2017 Elsevier.

a more extended conjugated network.[267] In order to exploit the band gap reduction *via* P doping and better charge mobility due to an extended π-conjugated network, C- and P-co-doped carbon nitride (CNPCN-1*) was synthesized using phytic acid as a sole source of C and P.[268] The resulting material exhibited a much higher yield for hydrogen generation in photocatalytic experiments (1493.3 μmol g^{-1} h^{-1}) which is *ca.* 9.7 times higher than the performance of unmodified g-C_3N_4. Carbon nitride materials modified with other heteroatoms, *i.e.*, sulfur, have also been reported for electrocatalytic and photocatalytic water oxidation.[269]

Apart from doping *via* the replacement of carbon or covalent functionalization, the strong intercalation of chlorine in the carbon nitride framework was found to result in a better photocatalytic efficiency for hydrogen evolution (Fig. 31). Chlorine intercalated g-C_3N_4 can be easily prepared by thermal treatment of melamine and ammonium chloride. Mott–Schottky curves revealed that the presence of chlorine upshifted the positions of the CB and VB. The electronic charge density plot showed that charge density was concentrated on the Cl atom, indicating the intercalation of Cl, which extends the local 2D π-conjugated system of g-C_3N_4 into three dimensions and facilitates charge separation (Fig. 32). The obtained Cl-modified g-C_3N_4 photocatalyst displayed 19.2 times more yield of H_2 than pristine g-C_3N_4, and an apparent quantum efficiency of 11.9% at 420 ± 15 nm.[270] By analogy Br-modified g-C_3N_4 exhibited a several-fold increment in hydrogen production.[271,272]

8. Surface area modification of carbon nitrides for improved hydrogen evolution

Apart from doping, surface area and morphological manipulation have been established to improve the adsorption of reactants, making more active sites available for the reaction, enabling the collection of more light and increasing the resulting photoresponse. The surface area of carbon nitride materials can be increased by the use of appropriate monomers and their reaction under planned conditions or by templating materials. Organic materials (especially surfactants such as P123, Triton-X, CTAB, *etc.*) were investigated for soft templating, while inorganic silica was used as a hard templating material to achieve a high surface area.[273–276] For example, a mesoporous carbon nitride structure prepared by a sol–gel method showed, upon the removal of the silica template with HF, an improved surface area and photoactivity for water splitting. High surface area carbon nitride prepared with tetraethyl orthosilicate and cyanamide (TEOS : CN) precursors in a 1 : 6 ratio was found to give the best results (40.5 mL H_2 in 24 h) under visible light using a H_2O/TEOA (9 : 1) mixture and Pt co-catalyst.[277] In the soft template method of surface area improvement, the generated pores have nonspecific geometry and may collapse during the heating step, which reduces the surface area. The use of an ordered mesoporous silica structure as a hard template is advantageous because in addition to an increase in the surface area, the mesoporous geometry remains intact after the removal of silica. The Vinu group has done pioneering work on ordered mesoporous carbon nitride synthesis by using SBA-15 as a template.[232] Numerous morphological modifications in the structure of carbon nitride have been achieved by this approach (spherical, hollow spherical, tubes, 3D structures, *etc.*) by using ordered silica sources, *i.e.*, KIT-6, KCC and MCM-41.[275,278,279] The surface properties like the surface area of carbon nitride materials can be further improved by using two or more carbon nitride sources. Xu *et al.* synthesized nanoporous graphitic carbon nitride having a 3.4 times higher surface area (46.4 m^2 g^{-1}) by heating dicyandiamide and thiourea at a programmed temperature.[273] In this synthesis, thiourea served as a source of the heptazine ring skeleton along with dicyandiamide and also acted as a soft template. Furthermore, the heating of specific hydrogen bonded precursors can help in attaining a specific morphology and crystallinity. Melamine and cyanuric acid form a hydrogen bonded macromolecular structure in DMSO and after precipitation give rise to flower like spheres, which upon annealing yield carbon nitride hollow spheres. These hollow spheres displayed better absorption and lifetime with a small broadening of the band gap. However, the morphology of these spheres was distorted due to the evolution of ammonia during the polycondensation step.[280] In contrast, microwave thermolysis of a melamine/cyanuric acid hydrogen bonded supramolecular conjugate produced more crystalline, defect-free hollow microspheres. A hydrogen evolution test in the presence of triethanolamine (TEOA) and a Pt cocatalyst (5 wt%) gave 40.5 μmol h^{-1}, being two-fold higher than that of g-C_3N_4 (Fig. 33).[281] The co-polycondensation of urea and oxamide produced g-C_3N_4 nanotubes (CN–OA). The CN–OA exhibited optical absorption above 465 nm due to the n → π* transition of lone pairs of nitrogen present on the edge of heptazine units. The apparent quantum yield (AQY) of CN-OA-0.05 for H_2 evolution with a green LED (>525 nm) reached 1.3%, which is approximately 10 times higher than that of bulk g-C_3N_4. Several nanostructured morphologies have been recently prepared by utilizing the melamine/cyanuric acid macromolecular structure under various conditions.[282] For example, Zhao *et al.* described the synthesis of hollow mesoporous g-C_3N_4 mesospheres from melamine cyanuric acid conjugates for water splitting.[283] The alteration of monomeric units was also accompanied by several

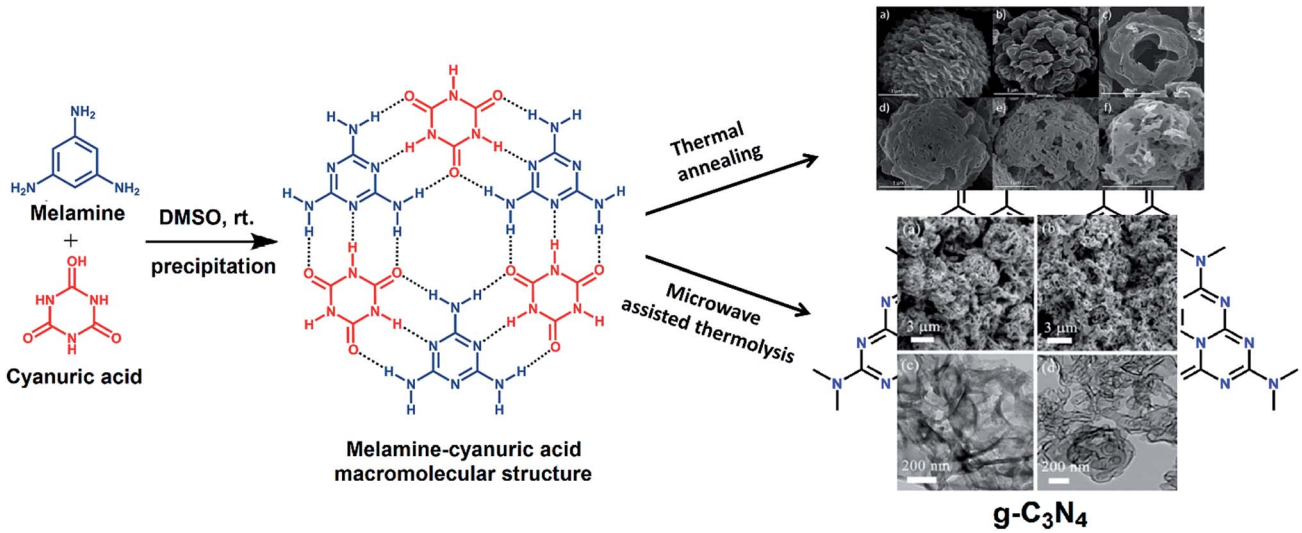

Fig. 33 Step (1): general outline of the synthesis of a hydrogen bonded melamine–cyanuric acid macromolecular structure in DMSO. Step (2): thermal and microwave annealing of the macromolecular structure to hollow spheres. Upside SEM image of C_3N_4 hollow microspheres: (a) as-synthesized and after thermal treatment at (b) 350 °C, (c) 400 °C, (d) 450 °C, (e) 500 °C, and (f) 550 °C (reproduced with permission from ref. 280 Copyright 2013 Wiley-VCH). Low side (a, b) SEM images of CN540 and CN_{16}; (c, d) TEM images of CN540 and CN_{16}. The notation CN540 represents microspheres prepared by thermal treatment of the macromolecular structure at 540 °C for 4 h and CN_{16} stands for microspheres prepared by microwave treatment for 16 min. (Reproduced with permission from ref. 281 Copyright 2016 Wiley-VCH).

morphological transformations, *i.e.*, 1,3,5-trichlorotriazine and dicyandiamide after hydrothermal treatment and thermal annealing gave a spherical O-doped C_3N_4 photocatalyst.[284] The addition of sulfur powder (S8) was also found to promote the synthesis of hollow vesicle shaped nanoparticles.[285] Furthermore, microwave promoted synthesis of various morphologically modified g-C_3N_4 assemblies is gaining popularity due to the fast reaction and efficient yield of products along with the preservation of the structure. Defected holy g-C_3N_4 sheets were prepared by microwave thermolysis of a hydrothermally digested dicyandiamide precursor for solar light mediated hydrogen evolution (81.6 μmol h^{-1}).[286]

9. Carbon nitride sheets as photocatalysts

The synthesis of carbon nitride through polycondensation of organic nitrogen containing precursors afforded bulk agglomerated structures similar to graphite; bulk graphitic carbon nitride possesses a layered structure in which tris-*s*-triazine units are connected to each other *via* planar amino groups in each layer. Therefore, bulk C_3N_4 can be delaminated into 2D sheets which have a unique surface and photocatalytic properties. However, studies showed that similar to the isolation of GO from graphite by Hummer's method, the synthesis of carbon nitride sheets was difficult because of the strong covalent C–N linkage between entangled sheets and hydrogen-bonding between the strands of polymeric melon units with NH/NH_2 group bonds.[287] Attempts to synthesise carbon nitride sheets by the Hummer's method resulted in the formation of g-C_3N_4 particles instead of nanosheets.[288] However, other "top-down" approaches such as thermal oxidation, etching, solvent

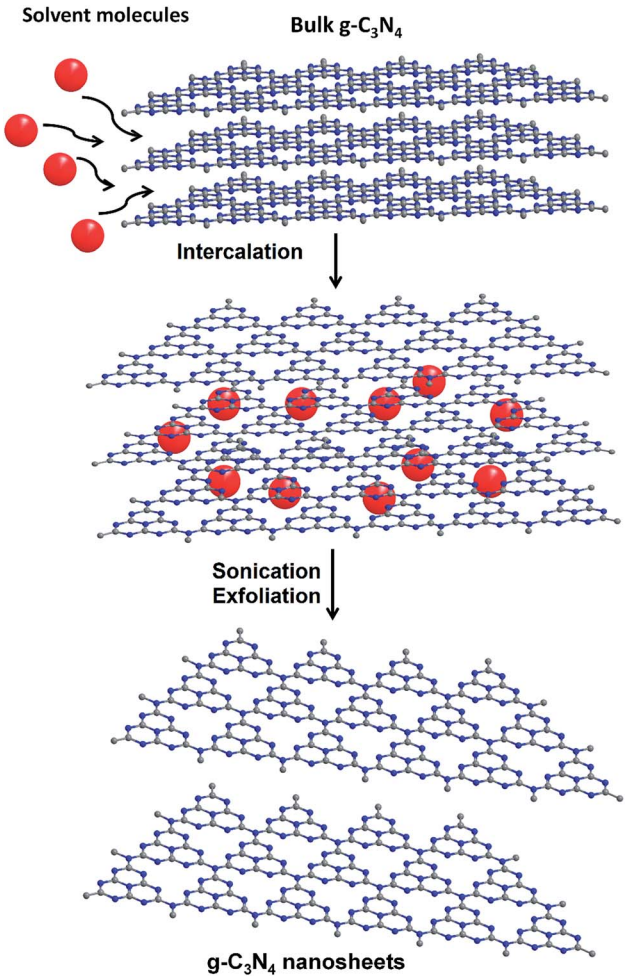

Fig. 34 Schematic illustration of solvent-assisted exfoliation of bulk g-C_3N_4 to ultrathin nanosheets. Adapted with permission from ref. 289.

exfoliation and precursor processing have worked well. Among them solvent mediated exfoliation is appealing due to its low cost, ease of processing, and the fact that the chemical structure remained unaltered during the detachment of the sheets. In solvent exfoliation, the solvent is intercalated between the sheets and induces their detachment (Fig. 34). For example, Yang *et al.* synthesized 2 nm thick g-C_3N_4 nanosheets with a high surface area (384 m^2 g^{-1}), large aspect ratio and plenty of nitrogen sites, by exfoliation of bulk carbon nitride in isopropanol.[99] The 2D sheets exhibited an exceptional hydrogen evolution rate (93 μmol h^{-1}), which was much higher than that of bulk g-C_3N_4 (10 μmol h^{-1}). Similarly, Ou *et al.* also reported the synthesis of crystalline carbon nitride nanosheets (CCNNSs) by delamination of bulk carbon nitride materials using isopropanol.[104] The obtained nanosheet structure was composed of approximately 10–12 sheets and exhibited an apparent quantum efficiency of 8.57% at 420 nm for hydrogen production from aqueous methanol, which was the highest AQE among various carbon nitride sheets. Other solvents such as water,[289] NMP, ethanol, 1,3-butanediol,[290] *etc.*, were also used for producing thin carbon nitride nanosheets. In the "bottom-up" approach, precursor materials generate few layered thick carbon nitride. For example, the use of Ph_4BNa with dicyandiamide affords sheets having an average thickness of 3.6 nm.[254] Monolayer carbon nitride sheets were also isolated using concentrated H_2SO_4 as the intercalation agent, followed by ultrasonication; the obtained material showed better light absorption behavior and hydrogen evolution activity.[100] Liquid ammonia (LA)-assisted lithiation, which involves the intercalation of lithium ions between g-C_3N_4 sheets, is a very fast exfoliation method (takes about 30 min).[291] Recently, the use of a few ring containing aromatic molecules bearing a polar group, *i.e.*, 1-pyrenebutyrate, has been introduced for exfoliation as well as non-covalent surface modification. The π–π stacking between the aromatic molecule and carbon nitride conjugated system helps in achieving better interactions between the molecule and sheets, while the polar moiety helps in the delamination of sheets in a polar solvent. Due to non-covalent interactions, the optoelectronic and surface properties of sheets remained intact.[292]

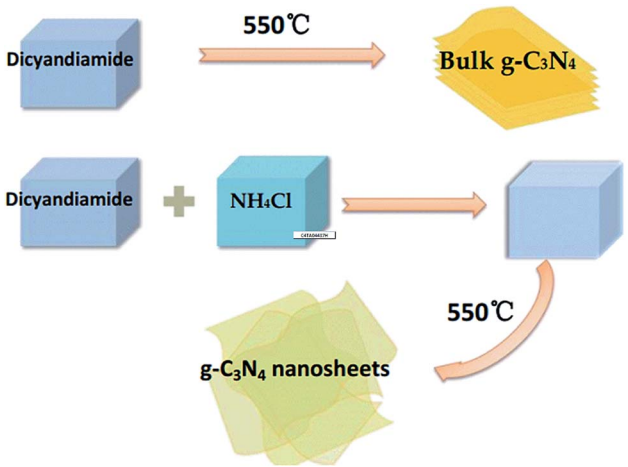

Fig. 36 Pictorial representation of the synthesis of bulk and ultrathin nanosheets of g-C_3N_4. Reproduced with permission from ref. 295 Copyright 2014 Royal Society of Chemistry.

Instead of the detachment of sheets, the synthesis of sheets from precursors and heteroatom additives is a more promising approach due to the avoidance of hazardous solvents and tedious workup. The heteroatom additives act as soft templates to obtain a 2D morphology. For example, heating of melamine with KCl produces carbon nitride nanosheets (1.5–10 nm) in a way compatible with green chemistry.[293] Furthermore, due to the presence of K^+ ions in the lattice structure, the process of charge recombination was decreased. The prepared nanosheets (K10-g-C_3N_4) gave a hydrogen evolution rate of 102.8 μmol h^{-1},

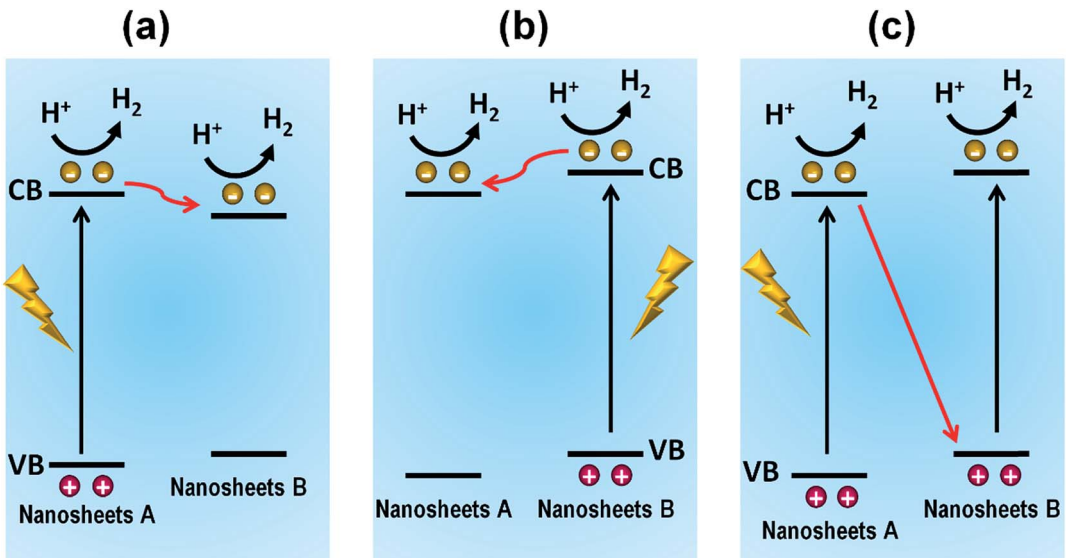

Fig. 35 Plausible mechanism of electron transfer between K-g-C_3N_4 nanosheets having different thicknesses and band structures. Adapted with permission from ref. 293.

about 13 times higher than that of a pristine g-C_3N_4 sample. The presence of variable thicknesses of sheets of different band gaps (depending on thickness) creates numerous heterojunctions in the material and photogenerated electrons move from high band gap sheets to low band gap sheets, which facilitates better charge separation (Fig. 35).

In a similar way, potassium borohydride was also investigated for the synthesis of C_3N_4 sheets with a thickness of ~1.5 nm (Fig. 36).[294] Ammonium chloride seems to be a better alternative for achieving carbon nitride sheets (~3.1 nm), because the fast annealing step creates gaseous bubbles, which behave like a gas template and produce ultrathin sheets without the additional step of removal of counter ions.[295] Fluorescence decay time measurement indicated that the lifetime of charge excited species of nanosheets was increased due to the quantum confinement effect. The catalyst exhibited an average hydrogen evolution rate of 450 μmol h^{-1} under a 300 W Xe lamp using a water/triethanolamine mixture.

The hybridization of carbon nitride nanosheets with metals or semiconductors has been found to enhance photoactivity. For instance, the nanocomposite of g-C_3N_4 and hexagonal CuS demonstrated a hydrogen evolution rate of 126.5 μmol h^{-1} that was much better than that of pure g-C_3N_4 nanosheets.[296] The hybridization of nanosheets with bulk materials also leads to efficient and fast charge separation due to the formation of variable band gap nanojunctions.[297] Near-infrared femtosecond transient absorption (TA) spectroscopy revealed that carbon nitride nanosheets can extract photogenerated electrons on bulk carbon nitride at a much faster rate than g-C_3N_4 alone. A 10% mass loading of g-C_3N_4 nanosheets on bulk carbon nitride materials exhibited a two times higher hydrogen evolution rate.[298] A hybrid of B-doped carbon nitride nanolayers with bulk CN materials (s-BCN) led to the enhancement of the photoelectrochemical response due to efficient charge separation between B-doped nanosheets and bulk g-C_3N_4. The fabricated nanojunction photoanode displayed 103.2 mA cm^{-2} at 1.23 V *vs.* RHE, a 10-fold higher photocurrent than the bulk graphitic carbon nitride (G-CN) photoanode, with an incident photon-to-current efficiency (IPCE) of 10% at 400 nm.[299] Apart from this, the sensitization of C_3N_4 nanosheets with organic dyes such as erythrosin B (ErB)[300] achieved enhanced photocatalytic hydrogen evolution.

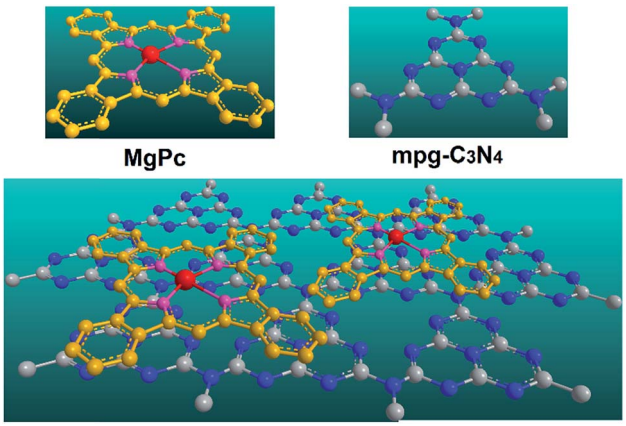

Fig. 37 Chemical structure of MgPc and carbon nitride, and immobilization of MgPc on mpg-C_3N_4 through π–π interaction. Adapted with permission from ref. 301.

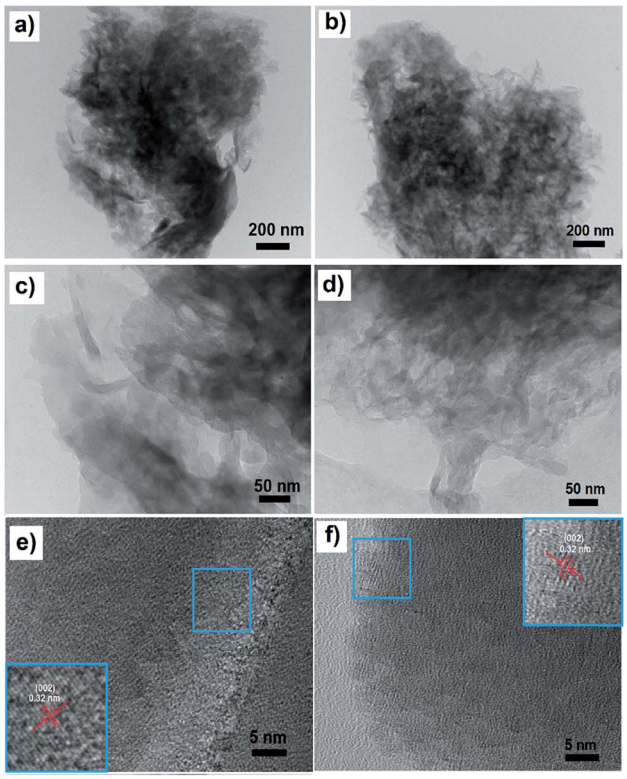

Fig. 38 TEM and HR-TEM images of npg-C_3N_4 and $Fe(bpy)_3$/npg-C_3N_4, showing porous (a, b), and crumpled (c, d) structures; (e, f) fringe patterns and 2*d* spacing. Reproduced with permission from ref. 303 Copyright 2016 Royal Society of Chemistry.

10. Metal complex functionalized carbon nitride

The immobilization of homogeneous metal complexes on carbon nitride improves the photocatalytic performance. Due to the structural similarity of carbon nitride sheets to graphene sheets, metal complexes can be immobilized on C_3N_4 sheets by noncovalent interactions (π–π or ionic interactions). For example, magnesium phthalocyanine was immobilized on the surface of mesoporous carbon nitride sheets by π–π stacking to improve the visible light response by sensitization (Fig. 37). The obtained 0.05 wt% MgPc/mpg-C_3N_4 nanohybrid catalyst afforded 0.07% quantum efficiency for hydrogen evolution at 660 nm in the presence of platinum as a co-catalyst (3 wt% Pt) and triethanolamine as the sacrificial donor.[301]

Similarly, asymmetric zinc phthalocyanine (Zn-tri-PcNc) immobilized on g-C_3N_4 behaved as a photosensitizer to produce hydrogen with an efficiency of 125.2 μmol h^{-1}.[302] In another report, Kumar *et al.* immobilized an iron bipyridyl complex ($Fe(bpy)_3$) on npg-C_3N_4 by taking advantage of π–π interaction, and employed $Fe(bpy)_3$/npg-C_3N_4 as an efficient

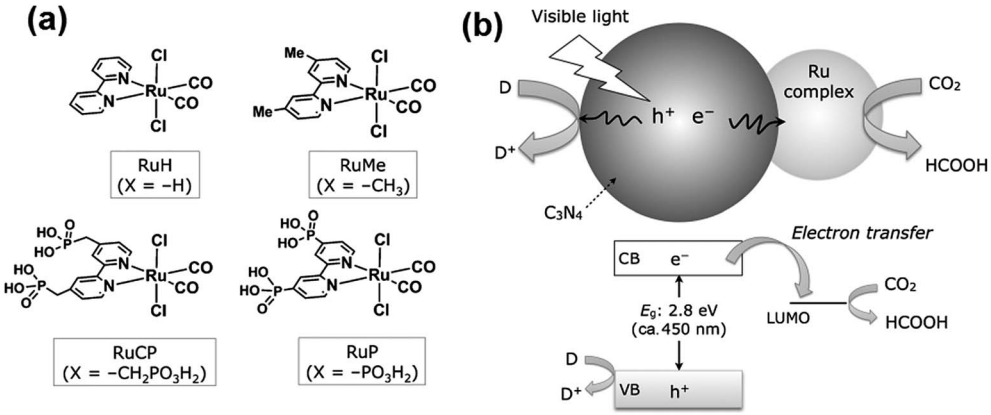

Fig. 39 (a) Structures of various Ru complexes used for attachment on C_3N_4. (b) Mechanism of CO_2 reduction by using a Ru complex/C_3N_4 hybrid photocatalyst. Reproduced with permission from ref. 304 Copyright 2015 Wiley-VCH.

photocatalyst for visible light mediated oxidative coupling of amines to imines under 20 W LED light (Fig. 38).[303] The higher photocatalytic performance was assumed to be due to the better injection of photogenerated electrons from the metal complex into the conduction band of carbon nitride. However, the attachment of the metal complex on carbon nitride sheets by π–π interaction is weak and prone to leaching in the solution phase, during photocatalytic experiments.

The presence of nitrogen atoms on carbon nitride sheets creates an unequal charge distribution on carbon nitride sheets and provides an opportunity for ionic interactions. In order to strengthen the attachment of metal complexes to carbon nitride sheets, Kuriki *et al.* functionalized C_3N_4 sheets with a ruthenium complex (*trans*(Cl)-[Ru(bpyX$_2$)(CO)$_2$Cl$_2$]; X = PO_3H_2), bearing phosphoric groups by anionic interaction. The resulting material gave a turnover number greater than 1000 and an apparent quantum yield of 5.7% at 400 nm for the reduction of CO_2 into formic acid (Fig. 39a).[304] It is worthwhile to mention here that the LUMO of *trans*(Cl)-[Ru(bpyX$_2$)(CO)$_2$Cl$_2$] type complex is situated below the conduction band of carbon nitride such that electrons can easily flow from carbon nitride to the metal complex, which subsequently produces CO, H_2 or HCOOH by CO_2 or proton insertion steps (Fig. 39b). The chain length also influences the efficiency of charge transfer between carbon nitride and the metal complex, *i.e.*, a long chain length has a detrimental effect on photocatalytic performance. For example, the metal complexes attached with a phosphoric group having additional carbon in the chain showed lower photocatalytic performance, due to inefficient charge transfer through a long chain. By following a similar approach, a ruthenium binuclear complex was also immobilized over the surface of g-C_3N_4 to achieve visible light assisted CO_2 reduction.[305] Porphyrin possessing four carboxylic moieties (mTCPP) was also immobilized on g-C_3N_4 by ionic interaction for solar light induced water splitting.[306]

To overcome the disadvantages of leaching and lower loading, covalent immobilization of homogeneous complexes has been envisaged as a viable solution to the problem. However, due to higher stability, carbon nitride sheets are supposed to be immune to functionalization and only a few reports are available on covalent functionalization of carbon nitride. Despite its chemically inert nature, harsh conditions can introduce some –OH functionalities into the sheets. Dong et *al.* prepared –OH functionalized graphitic C_3N_4 (O-g-C_3N_4) by thermal treatment with H_2O_2.[307] The introduction of –OH not only generated the possibility for further functionalization, but also reduced the band gap from 2.72 to 2.69 eV. Recent reports demonstrated that the amino group present at the edge of g-C_3N_4 sheets (g-C_3N_4–*x*CN) can be transformed into a nitrile (–CN) moiety by treatment with NaSCN and acetonitrile under photoinduced conditions, leading to a reduced band gap of carbon nitride down to 2.29 eV.[308] In another approach, –CN terminated P-doped g-C_3N_4 was prepared by treatment of g-C_3N_4 with NaH_2PO_2 at elevated temperatures, which facilitated the doping of P atoms and also reduced the –C–NH_2 moiety to –CN.[309] The decoration of various functional groups on the g-C_3N_4 structure can be cultivated to achieve stable molecular catalyst loading. Kumar *et al.* were able to achieve strong attachment of a heteroleptic iridium complex onto –OH functionalized nanoporous carbon nitride due to ionic interaction between the negatively charged –OH functionalized sheets and positively charged iridium metal complex (Fig. 40).[310] The synthesized nanoporous graphitic carbon nitride supported iridium complex (npg-C_3N_4/Ir-T) exhibited excellent activity for CO_2 photoreduction to methanol (9934 μmol g_{cat}^{-1}; TON 1241 with respect to Ir). The band gap value obtained from the Tauc plot and cyclic voltammetry suggested that due to the attachment of the iridium complex, the band gap was reduced to 2.24 eV. The conduction band position of npg-C_3N_4/Ir-T was found to be at −0.54 V *vs.* NHE being more positive than the reduction potential of formic acid (CO_2/HCOOH = −0.61 V) and comparable to that of CO (CO_2/CO = −0.53 V) and HCHO (CO_2/HCHO = −0.48 V), which ruled out their formation and methanol was selectively produced due to the large potential difference (CO_2/CH_3OH = −0.38 V) (Fig. 41). The –OH functionalized C_3N_4 (O–C_3N_4) also provides sites for further covalent functionalization, *i.e.*, the –OH groups in O–C_3N_4 were converted to alkyne functionalities by treatment with thionyl chloride and propargyl alcohol, and subsequently a cobalt complex bearing azide groups was attached *via* click reaction (Co@npg-C_3N_4) (Fig. 42).[311]

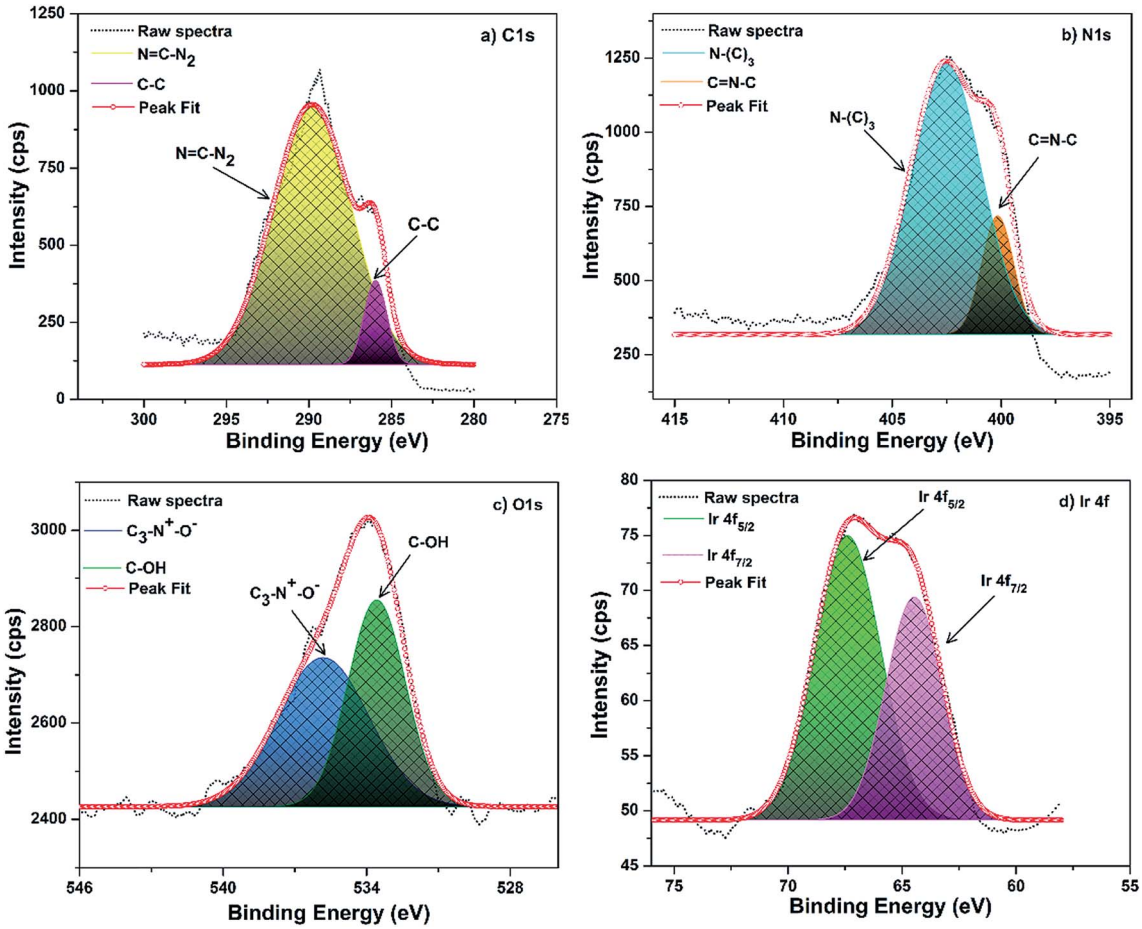

Fig. 40 High resolution XPS of npg-C_3N_4/Ir-T: (a) C_{1s}, (b) N_{1s}, (c) O_{1s} and (d) Ir_{4f} regions. Reproduced with permission from ref. 310 Copyright 2017 Elsevier.

In addition to the aforementioned approaches, hydrogen bonding was also considered to achieve robust binding between dye molecules and the carbon nitride framework. Viologen, an organic dye molecule, which behaves as an excellent redox mediator due to low reduction potential and the ability to form a stable radical cation ($V^{\bullet+}$), which is easily reoxidized to a dication (V^{2+}), was immobilized on g-C_3N_4 by taking advantage of hydrogen bonding.[312] The viologen modified carbon nitride composite showed an increased hydrogen evolution rate (41.57 μmol h^{-1}) due to efficient transfer of photogenerated electrons from carbon nitride to the Pt cocatalyst.

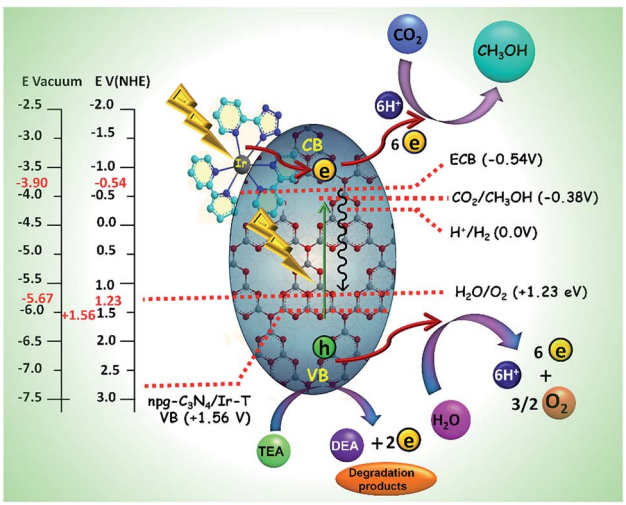

Fig. 41 Plausible mechanism of CO_2 photoreduction to methanol on npg-C_3N_4/Ir-T. Reproduced with permission from ref. 310 Copyright 2017 Elsevier.

11. New carbon nitride materials by alteration of the basic framework

Although tremendous work has been performed to improve the physical, morphological and surface properties of carbon nitride based materials to achieve higher photoresponsivity, chemical modification of the basic construction unit (*s*-heptazine or tri-*s*-triazine) is less explored and is still in its infancy. Fig. 43 displays various chemicals and construction units that can be used for the synthesis of g-C_3N_4 frameworks. The alteration of the basic framework of carbon nitride provides an opportunity to achieve entirely new physical and chemical properties and can be tuned by controlling the nature of chemical modification. Melon, a *s*-heptazine unit containing

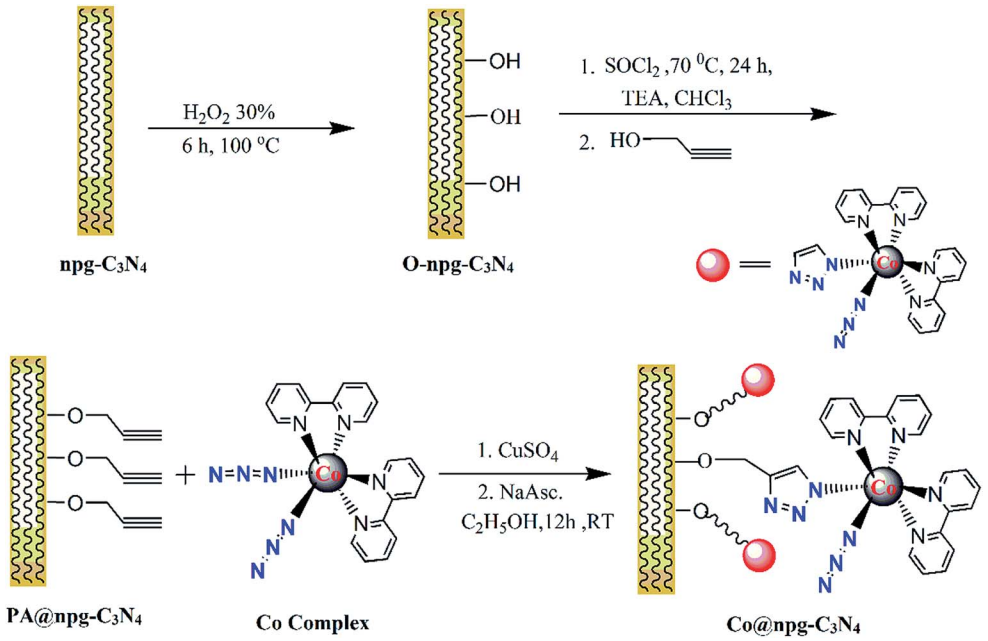

Fig. 42 Covalent functionalization of carbon nitride with a cobalt complex *via* [3 + 2] azide–alkyne cycloaddition "click" reaction to give a Co@npg-C_3N_4 photocatalyst. Reproduced with permission from ref. 311 Copyright 2017 Wiley-VCH.

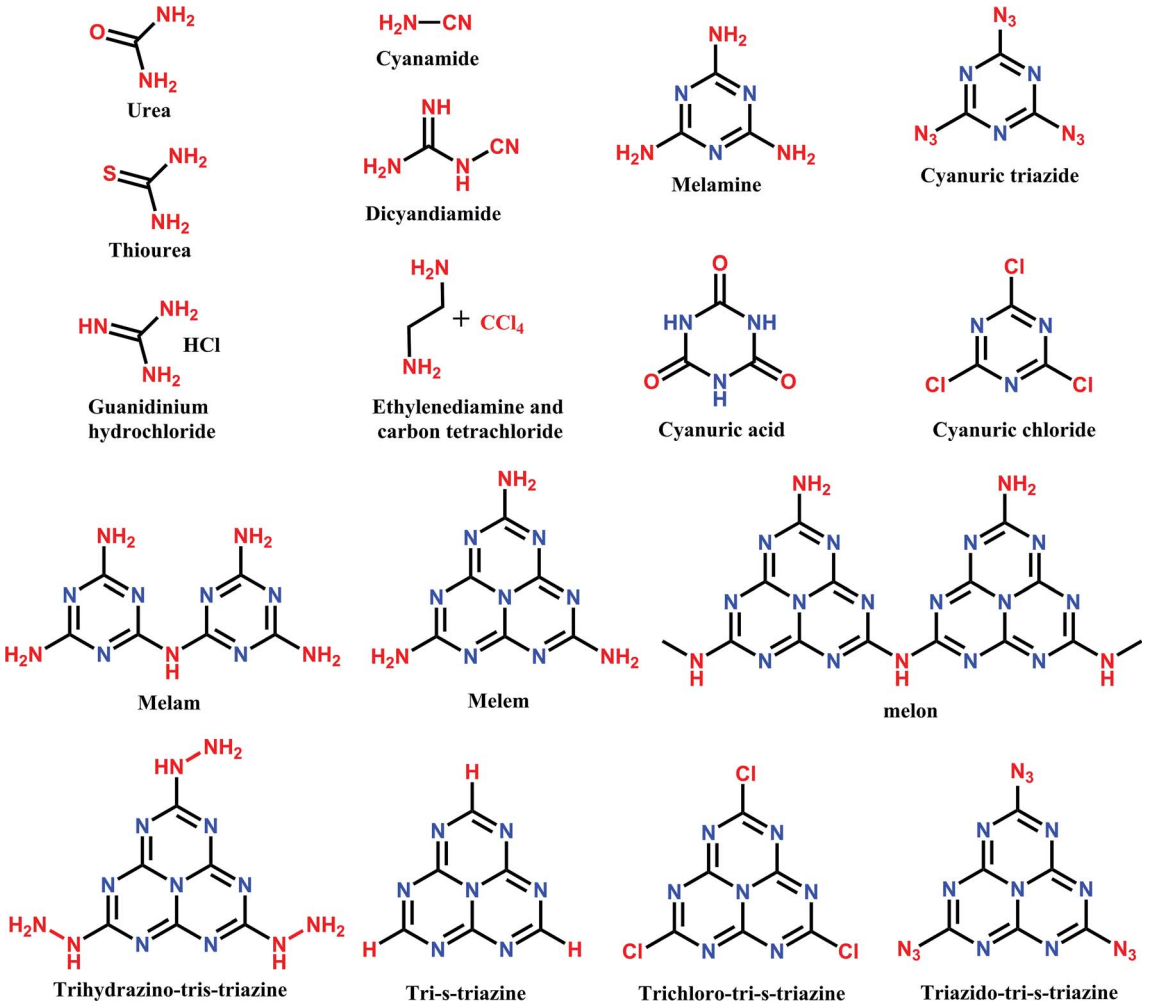

Fig. 43 Basic structure of some carbon nitride precursors and their relevant molecular structures.

oligomer (8–10), has been known for a long time since Berzelius synthesized it and Liebig named it.[313] The thermodynamic stability of melon is higher than that of g-C_3N_4, and a misconception identified it as g-C_3N_4, because its XRD pattern gives a pseudo-graphitic peak even though it does not have a sheet-like planar structure. Melem, 2,5,8-triamino-*s*-heptazine, has been considered as the smallest free unit of carbon nitride polymer and can be prepared easily by heating melamine at 400–425 °C.[314] Studies revealed that even a single unit of melem can act as a photocatalyst.[315] DFT calculations suggested that the hydrogen bonded heptazine-water unit can generate a molecular excited-state, which promotes hemolytic oxidation of water *via* an electron/proton transfer from water to the heptazine unit. The produced heptazinyl radical produces hydrogen by the detachment of the proton either by absorbing a second photon or by the recombination of two heptazinyl radicals and regenerating two heptazine molecules.[316] Furthermore, a hybrid of melem and g-C_3N_4 (melem/g-C_3N_4), prepared by a hydrothermal method, revealed that the presence of melem on the carbon nitride framework increases the visible light mediated dye degradation capability by lowering the electron–hole pair recombination rate.[317] The amino functionalities in melem can be transformed into other groups such as –Cl, –OH, –N_3, –O^-K^+, –NH–NH_2, –N_3, –N=PPh_3, *etc.*[318,319]

The strategic modification of monomer units can afford a carbon nitride framework with different properties. The introduction of a new organic unit into a carbon nitride heptazine framework can modify the band gap structure. For example, when an electron deficient pyromellitic dianhydride (PMDA) unit was introduced into the carbon nitride framework by the reaction of PMDA and melem (1 : 1 wt ratio) at 325 °C, a new polyimide polymer was obtained (Fig. 44). The distinct

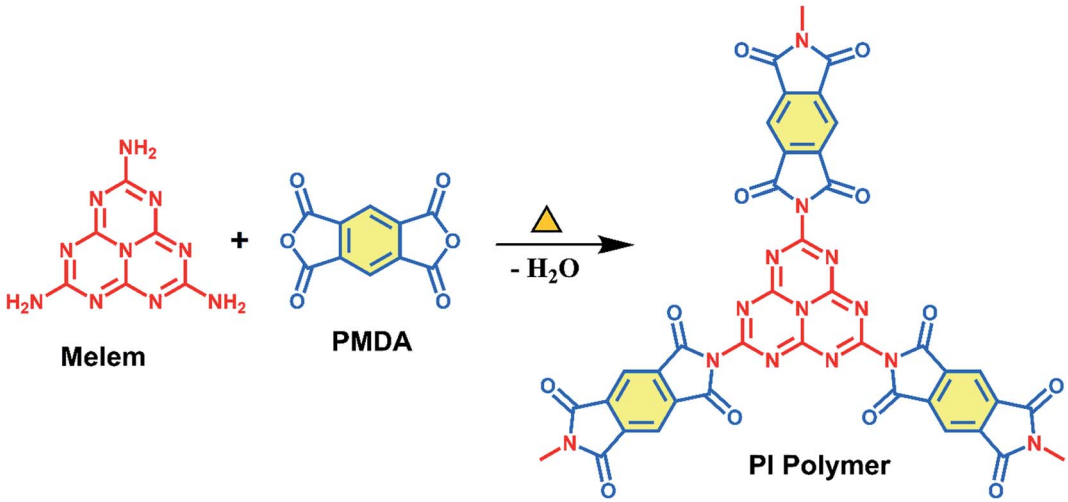

Fig. 44 Synthesis scheme of PI polymer by solid state thermal poly-condensation of melem and PMDA. Adapted with permission from ref. 320.

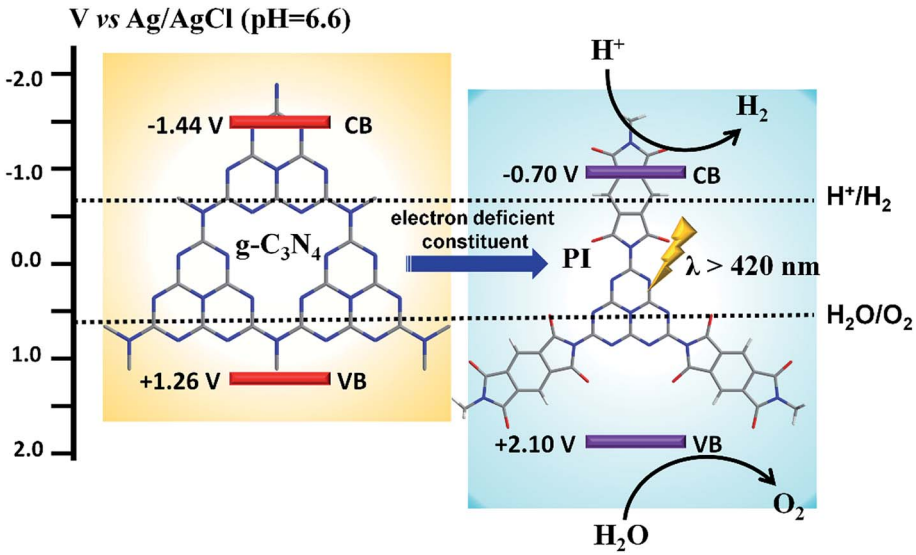

Fig. 45 Sketch of the band structure of g-C_3N_4 and polyimide polymer depicting the shifting of the band position of carbon nitride by introducing PMDA units. Adapted with permission from ref. 320.

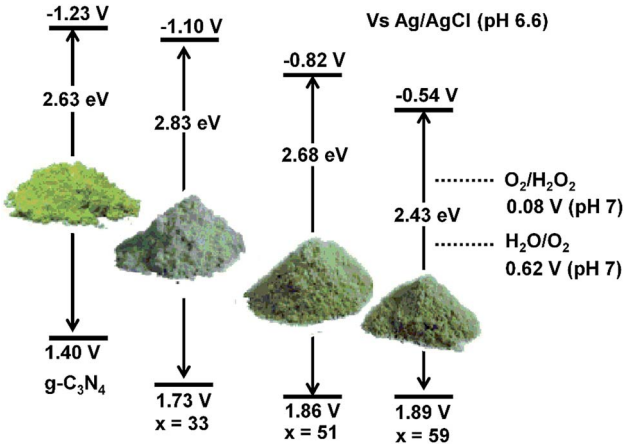

Fig. 46 Electronic band structures of g-C_3N_4 and g-C_3N_4/PDI_x polymer prepared using different ratios of melem and PMDA. Reproduced with permission from ref. 321 Copyright 2014 Wiley-VCH.

feature of the new polyimide polymer from parent carbon nitride was confirmed by XPS, ^{13}C NMR, TEM, XRD, *etc.*, which confirmed the well-established synthesis of the polymeric structure. The band gap of the polyimide polymer was found to be 2.8 eV, which was wide enough to maintain the criterion of a large band gap. Furthermore, due to the insertion of the PMDA unit, the conduction band position of C_3N_4 was shifted from −1.44 V to −0.70 V (*vs.* Ag/AgCl at pH = 6.6), while the valence band showed more oxidative shifting from 1.26 to 2.10 V, clearly revealing the better potential of the catalyst to oxidize water. Due to the shifting of band positions, the rate of hydrogen evolution was increased up to 20.6 μmol h^{-1} in comparison to pristine g-C_3N_4 (7.0 μmol h^{-1}), while a drastic increment of oxygen evolution of 7.7 μmol h^{-1} for PI polymer and 0.8 μmol h^{-1} for g-C_3N_4 was achieved due to more positive oxidation potential (Fig. 45).[320]

The less oxidative valence band of g-C_3N_4 limits its application in numerous oxidation processes such as photocatalytic H_2O_2 synthesis from H_2O and O_2. The prime requirement for visible light photocatalytic H_2O_2 production from water oxidation is that the valence band edge should be more positive, while the band gap should be low enough to obtain adequate absorption in the visible regime. Polyimide offers the possibility of modification of the band gap and band edge position by varying the concentration of monomer units during synthesis. Shiraishi *et al.* demonstrated that by controlling the number of polyimide units in the g-C_3N_4/PDI photocatalyst, the band gap and band positions can be tuned in a desired range (Fig. 46).[321] A g-C_3N_4/PDI_x photocatalyst containing 33, 51, and 59 mol% PDI units was synthesized by heating melem and PMDA in a 1 : 1, 1 : 2 and 1 : 3 wt% ratio at 598 K. The obtained band gap value of g-C_3N_4/PDI_x polymer containing 33, 51, and 59 mol% PDI units was determined to be 2.83, 2.68 and 2.43 eV, respectively, while the band gap of pristine g-C_3N_4 was calculated to be 2.63 eV. Interestingly, the positions of the conduction and valence bands of the g-C_3N_4/PDI_x polymer were shifted toward more positive values, as determined using Mott–Schottky plots. The CB edge positions of pristine g-C_3N_4 and g-C_3N_4/PDI_x polymer containing 33, 51, and 59 mol% PDI units were calculated to be −1.23, −1.10, −0.82 and −0.54 V, respectively, while the VB edges were shifted to +1.40, +1.73, +1.86 and +1.89 V, respectively. The observed shift in the band position was due to the high electron affinity of the diimide unit, which shifted the oxidation and reduction potentials of g-C_3N_4/PDI_x. DFT studies on the melem-PDI model unit suggested that the incorporation of PDI units decreased S_0 and S_1 levels, and the distribution of electron density was mainly located on the HOMO and LUMO+2 of the melem-PDI model unit with partial

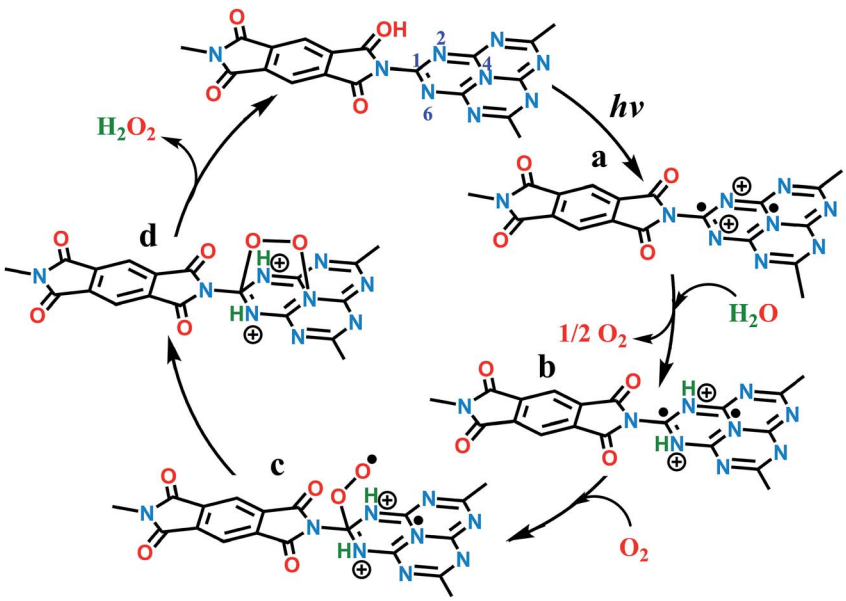

Fig. 47 Proposed mechanism for H_2O_2 formation on photoactivated g-C_3N_4/PDI from water and O_2. Reproduced with permission from ref. 321 Copyright 2014 Wiley-VCH.

distribution to the PDI units. Furthermore, electrons in melem units were located at N2 and N6 for the HOMO and C1 and N4 for the LUMO+2 model, suggesting that N2 and N6 act as oxidation sites while C1 and N4 provide reduction centers. g-C_3N_4/PDI_x photocatalysts were found to be potentially active for visible light mediated H_2O_2 production from water and oxygen. g-C_3N_4/PDI_{51} afforded the highest H_2O_2 yield of 50.6 μmol after 48 h which was 250 times higher than that obtained with pristine g-C_3N_4 (<0.2 mmol). The absence of H_2O_2 when using a mixture of g-C_3N_4 and *N*,*N*′-dipropyl PDI in photoreactions revealed that the incorporation of PDI units into the polymer scaffold by means of a chemical bond was vital for H_2O_2 production. After the absorption of two photons, two electron–hole pairs were generated at the melem unit; holes were localized at N2 and N6 and facilitated water oxidation, while electrons were localized at C1, and N4 and reduced O_2 by following 1,4-endoperoxide intermediate species. This intermediate 1,4-endoperoxide species, after the abstraction of two protons from C1 and N4 positions, yields H_2O_2 (Fig. 47). Replacing the PMDA unit with mellitic anhydride (MA) was also utilized for the synthesis of polyimide polymer (g-C_3N_4/MTI_x) possessing a deep valence band position. g-C_3N_4/MTI_x containing 49 mol% mellitic triimide displayed a band gap of 2.48 eV and the positions of the CB and VB were found to be −0.09 and +2.39 V, respectively.[322] The application of g-C_3N_4/MTI_x for H_2O_2 was able to afford 0.18% solar to chemical (STC) conversion efficiency, which was approximately double that of natural photosynthesis (~0.1%). Unconventional microwave heating was also utilized for the synthesis of polyimides/metal oxide frameworks.[323,324]

Polyimide polymers were also prepared by solid state reaction using melamine and PMDA at 325 °C in a semi-closed system (Fig. 48).[111] By controlling the amount of one precursor, amino or anhydride terminated polymer can be synthesized. For example, when excess of PMDA was used the N–H signal in the FTIR spectra of PI was decreased and new signals around 1850 cm^{-1} were observed. TGA analysis of the reaction mixture (melamine and PMDA) suggests that for achieving polymerization, the reaction temperature should be

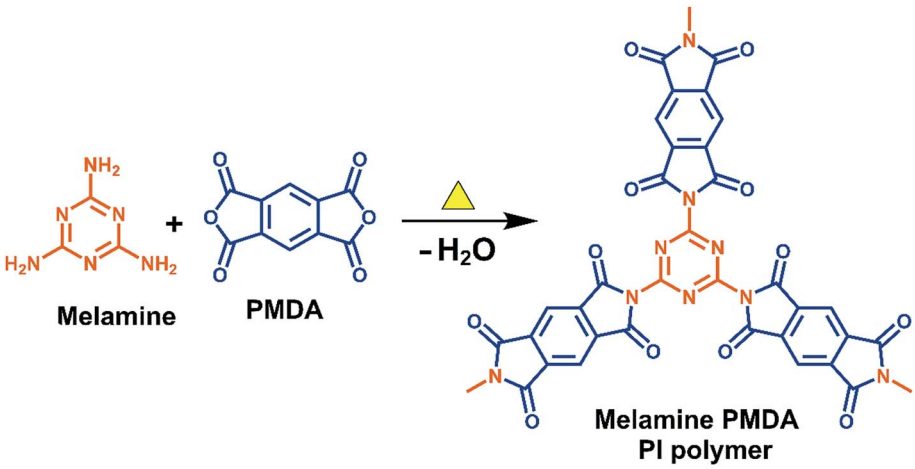

Fig. 48 Synthesis approach of PMDA-triazine polyimide with melamine and PMDA. Adapted with permission from ref. 111.

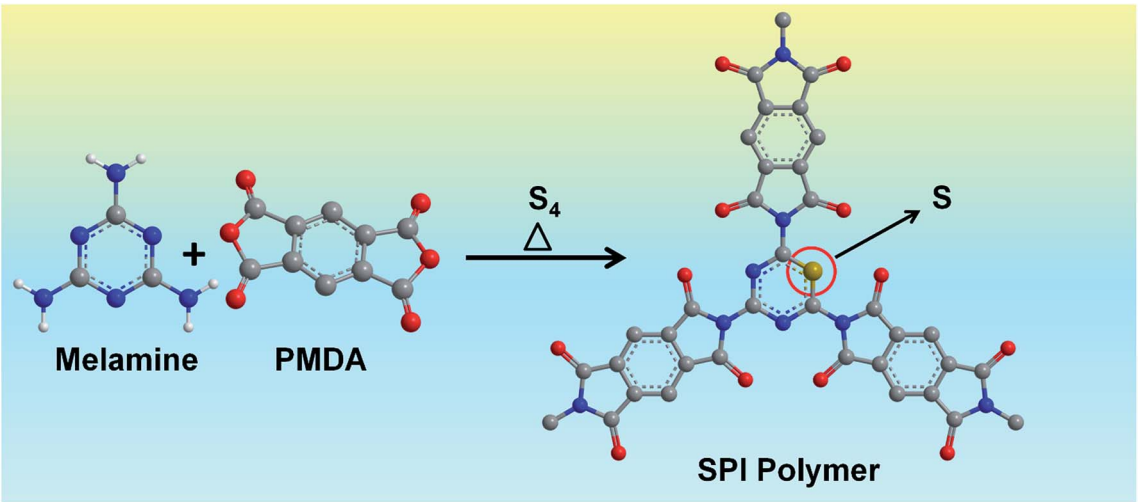

Fig. 49 Synthesis scheme of S-doped polyimide polymer (SPI) by polycondensation of MA and PMDA in the presence of S4 at 598 K. Adapted with permission from ref. 325.

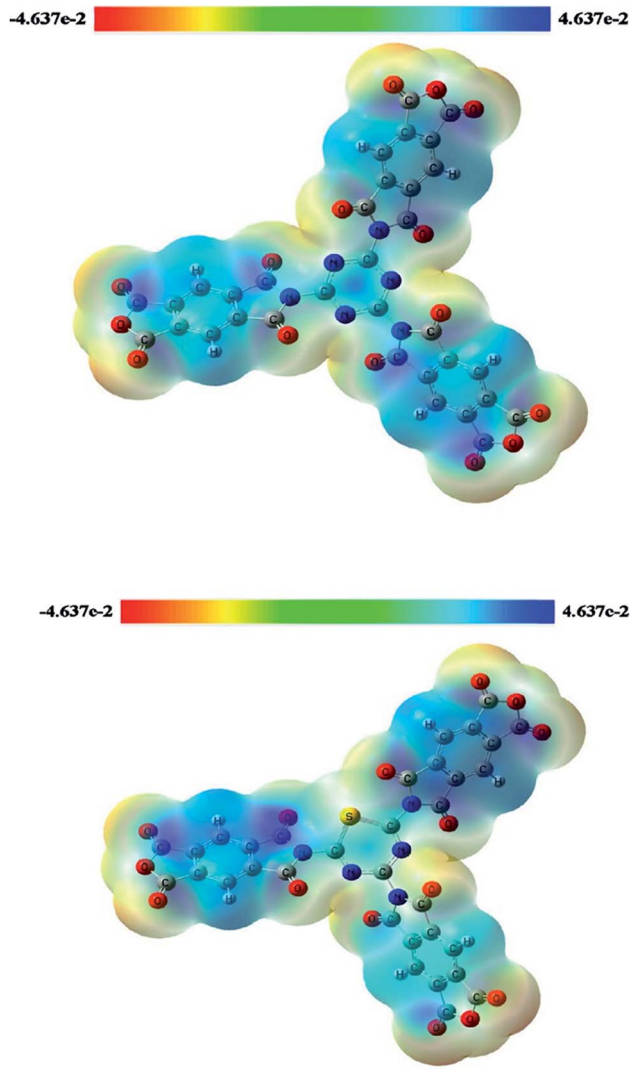

Fig. 50 Calculated electronic densities of PI (top) and SPI (bottom) samples. Carbon, nitrogen, oxygen, and sulfur in the structural models are shown as gray, blue, red, and yellow spheres, respectively. Reproduced with permission from ref. 325 Copyright 2014 American Chemical Society.

higher than the melting point of PMDA (285 °C) and no reaction takes place at 250 °C. The synthesized polymer possessed a band gap value of 2.7 eV, which was large enough to facilitate water splitting while maintaining absorption in the visible region. DFT calculation of PI revealed that the highest occupied molecular orbital (HOMO) was located on the melamine, while the lowest unoccupied molecular orbital (LUMO) was located at the PMDA moiety. The HOMO and LUMO located in different parts of the polymer favor spatial charge separation and thus benefits the photocatalysis process. The synthesized PI polymer was tested for hydrogen evolution using visible light ($\lambda > 420$ nm) with Pt as a cocatalyst and methanol as a sacrificial donor. After 10 h of irradiation, the yield of hydrogen was found to be 70 μmol, which was comparable to that of pristine g-C_3N_4 photocatalyst or double if the surface areas of g-C_3N_4 (10 m^2 g^{-1}) and PI (5 m^2 g^{-1}) are considered.

The sulfur doping of polyimide polymer of melamine and PMDA (SPI) with S_4 as a dopant has been found to increase the visible light absorption profile (Fig. 49). XPS analysis showed that S atoms were introduced into the polymer backbone by replacing the N atoms of the triazine ring to form a S–C bond. The result was corroborated by the calculation of the electrostatic potential (ESP) on the surface of PI, which demonstrated that by replacement of N atoms with S atoms, the electrostatic potential on the triazine ring was disturbed and the electron density on the ring was increased (Fig. 50). The value of the valence band position, as obtained by VBXPS for S-doped PI polymer, was determined to be 1.6 eV, being more negative than that of PI polymer (0.9 eV) and revealed the superior oxidizing power of the catalyst.[325]

These reactions are tedious in the solution phase because of repulsion between the molecular orbitals of oxygen on cyclic anhydrides and nitrogen on melem, which induces steric hindrance. However, the activation of anhydride groups by converting them into –COCl groups and subsequent reaction with melem appears to be a promising solution to form an imide (Fig. 51).[326]

The reaction can also proceed in the presence of a strong Lewis acid and high boiling solvents such as ionic liquids. For instance, a microporous polyimide (PI) framework was prepared by condensation of perylene-3,4,9,10-tetracarboxylic dianhydride (PTCDA) and 1,3,5-triazine-2,4,6-triamine (melamine) by using a zinc acetate/imidazole complex as the Lewis acid (Fig. 52). This polymer, after calcination, gives highly porous nitrogen-rich carbon which adsorbs CO_2 selectively.[327] Recently, heat treatment of carbon and nitrogen rich precursors with planar conjugated structures or planar metal complexes has become a suitable method to prepare highly active carbon based catalysts for catalytic transformations. Many metal organic frameworks (*i.e.*, ZIF-67) can also be used for the synthesis of N-rich metal doped carbon with good catalytic and photocatalytic activities.[328] Similarly, a g-C_3N_4/PTCDA nanocomposite (CN–P) was prepared by thermal condensation of cyanamide and PTCDA at elevated temperature. The synthesized CN–P imide polymer displayed excellent visible absorption and produced hydrogen from water at a rate of 17.7 mmol h^{-1} g^{-1}, with an apparent quantum efficiency of 5.8% at 450 nm.[329] In a recent report, highly porous organic polymers (POPs) were designed by the reaction of hexakis(4-formylphenoxy)cyclotriphosphazene and *meta*- and *para*-substituted amine (*o*- and *m*-phenylenediamine) *via* imine bond formation. Upon calcination at high temperature, these POPs gave high surface area N/P dual-doped carbon. The *m*-substituted imine polymer, after carbonization at 900 °C (C-POP-2-900), gave the highest specific surface area (~1535 m^2 g^{-1}). It is worth mentioning that here the cyclotriphosphazene unit works both as a structure determining agent to improve the surface area as well as a source of N and P atoms for co-doping.[330]

Furthermore, triazine based 2D covalent organic frameworks (COFs) have also been demonstrated to be good photocatalysts, CO_2 capturing agents, and gas separation agents.[331–333] A triazine based covalent organic framework (2D CTF),

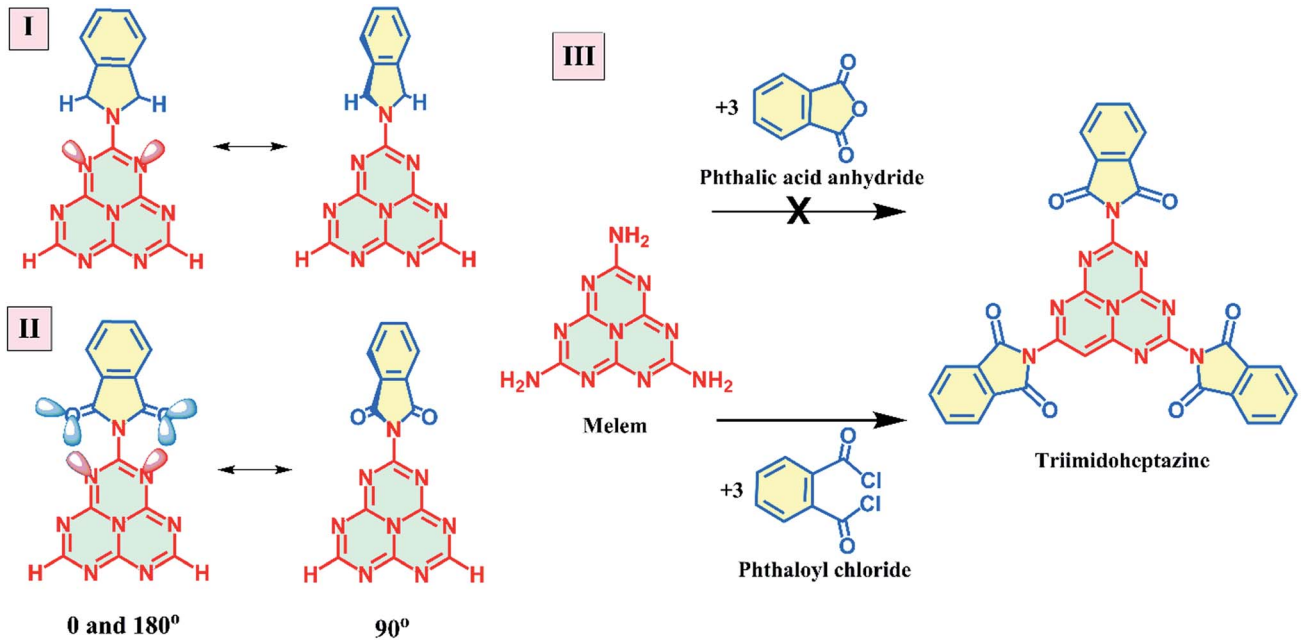

Fig. 51 Structure of imides of (I) 1,3-dihydroisobenzofuran and (II) phthalic acid anhydride (PAA) with melem showing their rotational conformer. Structure II illustrates repulsion between the lone pairs of the oxygen and nitrogen atoms. (III) Reaction of (PAA) with melem is unfavorable under normal conditions while the reaction of melem with activated phthaloyl dichloride (PACl) gives triimido-heptazine. Reproduced and modified with permission from ref. 326 Copyright 2012 Wiley-VCH.

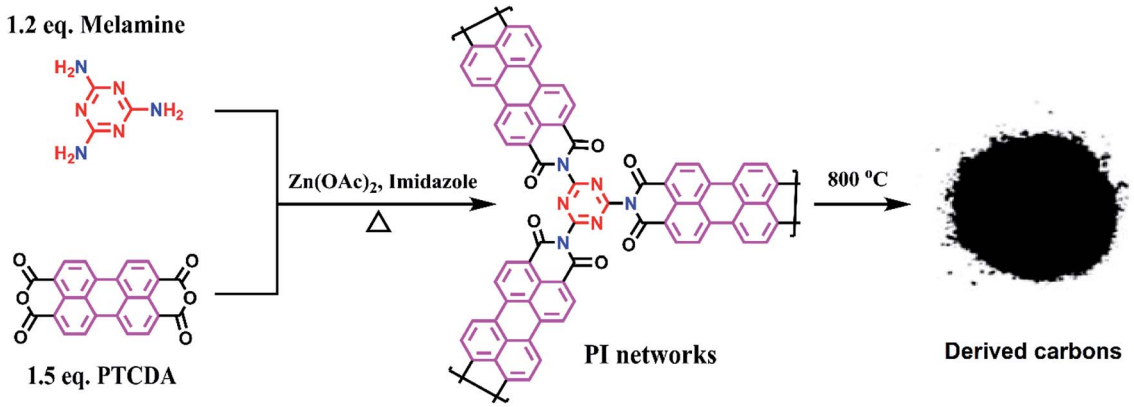

Fig. 52 Synthesis outline of polyimide (PI) frameworks from PTCDA and melamine and subsequent calcination of the polymer to porous nitrogen rich carbon. Reproduced with permission from ref. 327 Copyright 2015 American Chemical Society.

synthesized by the reaction of cyanuric chloride and perylene diimide, was found to be a good photocatalyst for the selective reduction of CO_2 to formic acid.[334] Interestingly, heptazine-based microporous polymer networks (HMP-3), prepared by the reaction of two moles of cyameluric chloride and three moles of 4,4′-(benzo[c][1,2,5]thiadiazole-4,7-diyl)dianiline (BTDADA), can operate as a donor–acceptor assembly in which the heptazine unit acts as an acceptor, while BTDADA acts as a donor (Fig. 53).[335] This HMP-3 polymer with different monomer ratios was prepared and named HMP-3 2 : 3 and HMP-3 4 : 3, respectively. The band gap of the polymeric structure HMP-3 2 : 3 and HMP-3 4 : 3 was determined to be 2.0 and 2.1 eV and evolved 32 μmol h^{-1} and 31 μmol h^{-1} of hydrogen under simulated solar light, respectively. The photoluminescence spectra of HMP-3 polymer at a 370 nm excitation wavelength showed prominent quenching due to better separation of charge between donor–acceptor assemblies. Furthermore, isotopic labeling with D_2O gave D_2 and HD, which confirmed the true origin of hydrogen from water splitting.

In another study, a 2D-CTF (covalent triazine framework) having a chemical composition of $C_{12}N_7H_3$ (referred to as g-$C_{12}N_7H_3$), consisting of alternate benzene and heptazine rings and its multilayer stacking to form a g-C_9N_{10}/g-$C_{12}N_7H_3$ graphene/g-$C_{12}N_7H_3$ heterojunction to improve the electron–hole separation and photo-efficiency were theoretically predicted.[336] The predicted electronic properties such as the band positions and optical properties of g-$C_{12}N_7H_3$ show a direct band gap of

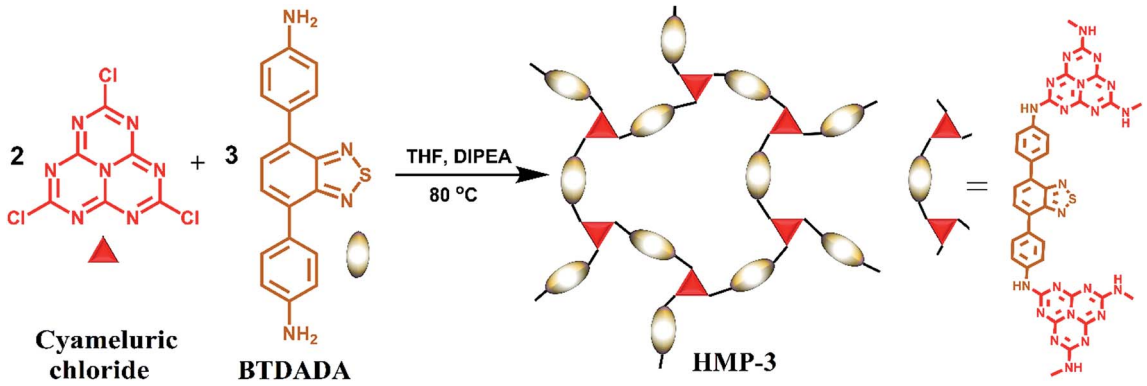

Fig. 53 Schematic illustration of the synthesis of HMP-3 polymer by copolymerization of cyameluric chloride and 4,4′-(benzo[c][1,2,5]thiadiazole-4,7-diyl)dianiline (BTDADA). Adapted with permission from ref. 335.

3.24 eV using the HSE06 hybrid function and the CBM position was 0.75 eV more reductive than proton reduction potential while the VBM position was 1.26 eV more oxidative than water oxidation potential. Furthermore, it has been shown that upon increasing the number of layers, the band gap decreases and can reach 2.91–2.61 eV for 2–6 layers. Nitrogen rich CTF (g-C_9N_{10}) composed of alternate triazine and heptazine units was also investigated and the optimum band gap was found to be 2.69 eV. In the g-C_9N_{10}/g-$C_{12}N_7H_3$ heterojunction, the p_z orbitals of nitrogen atoms in g-$C_{12}N_7H_3$ compose the VBM, while p_z orbitals of nitrogen and carbon atoms in g-C_9N_{10} create the CBM. The lack of overlap of VBM and CBM charge density distribution facilitates efficient electron–hole separation to achieve better photo-catalytic performance. However, a recent report highlighted the challenges associated with band gap calculation using DFT; the difference between theoretical and observed values may be as high as 1 eV.[337] The surface protonation of polymeric materials has been used for tuning the electronic and photoluminescence properties.[338] For instance, the protonation of g-C_3N_4 with a strong acid (37% HCl) produced protonated carbon nitride (g-C_3N_4–H^+Cl^-) having a better solubility/dispersibility, electronic structure, and surface area.[339] The azide precursor of melem (2,5,8-triazido-*s*-heptazine) can afford nitrogen-rich carbon nitride with good luminescence properties.[340] In addition, the hybridization of semiconductors such as MoO_3,[341,342] carbon nitride,[343] WO_3,[344] SWO_3,[324] MoS_2 (ref. 345) and ZnO[346] with polyimide polymer has been reported for enhanced photocatalytic performance. In an appealing report by Bhunia *et al.*, a new carbon nitride (polytriazine imide, PTI) material with different C/N ratios was synthesized by the reaction of melamine and 2,4,6-triaminopyrimidine.[347] Firstly, a hydrogen bonded supramolecular structure was obtained, which upon polycondensation gave a highly crystalline polytriazine imide (PTI) structure consisting of a copolymerized Mel–TAP network. DFT calculations showed a bandgap reduction by 0.6 eV due to a negative shift in the valence band (VB) level upon doping. The composite of polymeric materials with a KCC-1 structure was prepared to achieve maximum light absorption. The obtained PTI-0.15/KCC-1 exhibited an apparent quantum yield of 22.1% and 16.9% for the HER at 400 and 420 nm, respectively (Fig. 54).

The structural change in the monomeric unit also influences the coordination behavior of carbon nitride materials with metals. The incorporation of metals into the nano-cavity of the

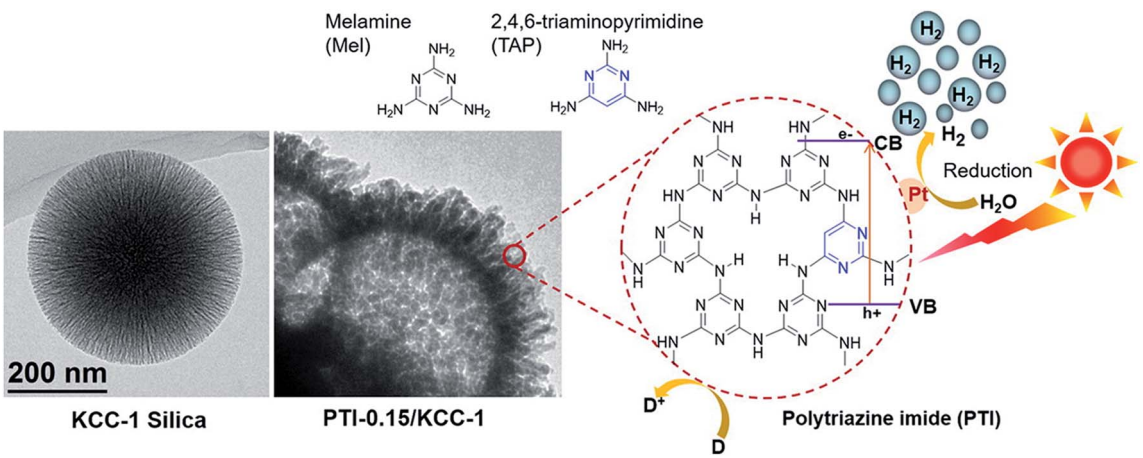

Fig. 54 Chemical structures of melamine (Mem), 2,4,6-triaminopyrimidine (TAP) monomers and polytriazine polymer; right: SEM images of KKC-1 silica and PTI-0.15/KCC-1. Reproduced with permission from ref. 347 Copyright 2015 American Chemical Society.

carbon nitride framework can afford a single atom heterogeneous catalyst (SAHC) system. However, low coordination atoms remain less stable, so the replacement of N atoms with C atoms may provide stable SAHCs. One such system was prepared by introducing high C containing barbituric acid or 2,4,6-triaminopyrimidine units into the g-C_3N_4 framework, which forms stable SAHCs with Pd metal.[348] A compositional change in the carbon nitride 2D framework can also be achieved by functional group transformation on monomer units. For example, Zhao *et al.* demonstrated that the hydrothermal treatment of melamine in water at 200 °C induces the transformation of amine groups in melamine to carbonyl/–OH moieties, resulting in cyanuric acid formation which under hydrothermal conditions was polymerized to yield nitrogen-rich layered organic materials. This layered organic material, after thermal annealing at 550 °C, gave a new CN material.[50] The morphology of the material was dependent on preservation time; the carbon content of the material increased and the observed C/N ratio was found to be 2.30 : 1 after a 2.5 h hold time. The increase in C content was supposedly due to the elimination of oxygen from the C=O moiety at elevated temperature. An increase in carbon content facilitates better charge mobility on the surface of the CN semiconductor. The developed CN photocatalyst was tested for hydrogen evolution by using triethanolamine as a sacrificial donor and Pt as a co-catalyst. The CN sample, prepared at 550 °C and 1.5 hold time, achieved the highest hydrogen evolution rate (1325.1 μmol h^{-1} g^{-1}), while g-C_3N_4 prepared from the melamine precursor could afford only a hydrogen evolution rate of 138.0 μmol h^{-1} g^{-1}. Usually, a high temperature condensed carbon nitride network contains three *s*-heptazine or triazine units linked together with a bridged nitrogen atom. However, careful selection of precursor molecules can generate a cross-linked heptazine framework in which –NH– serves as the bridging moiety. For example, a highly cross linked framework of poly(heptazine imide) was prepared by thermal copolymerization of dicyandiamide with tetramethylammonium salts and showed increased hydrogen evolution with photonic crystals.[349] Additionally, –NH– bridged imides can be synthesized by electrochemical means at a higher applied voltage and moderate temperature. A poly(triazine imide) polymer (PTI) in which the triazine units remain linked together *via* –NH– bridging was prepared electrochemically at 65 °C and linear ramping of the voltage from 5 to 200 V.[350]

12. Graphene/carbon nitride hybrids in photocatalysis

Similar to graphene/semiconductor composites in which photogenerated electrons are efficiently transported on the surface of graphene to achieve higher photoefficiency, nanocomposites of carbon nitride and graphene or graphene derivatives have also been prepared. It has also been observed that the hybridization of graphene with carbon nitride permits the manipulation of the band structure of carbon nitride to achieve high visible light absorption. Due to the aromatic conjugated system in graphene and carbon nitride, their sheets can interact through π–π stacking and it has been found that the immobilization of 1.0 wt% reduced graphene oxide on g-C_3N_4 can modulate the band structure of carbon nitride between more "n-type" and more "p-type" to give 300% higher anodic photocurrent than unblended carbon nitride.[351] Wang *et al.* demonstrated the preparation of face to face contacted monoatomic-

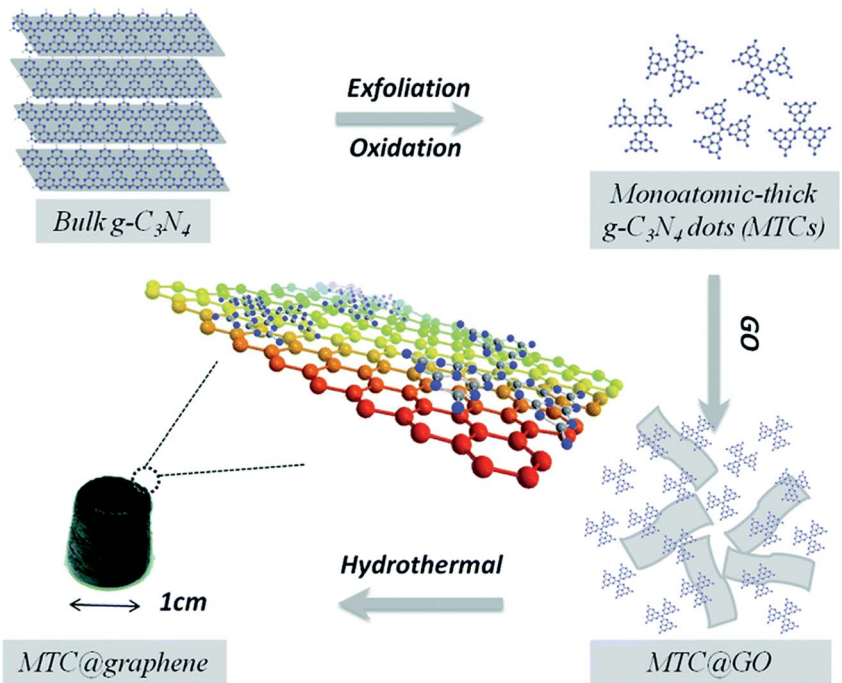

Fig. 55 Proposed synthesis protocol of monoatomic-thick g-C_3N_4 dots@graphene (MTCG). Reproduced with permission from ref. 109 Copyright 2015 Royal Society of Chemistry.

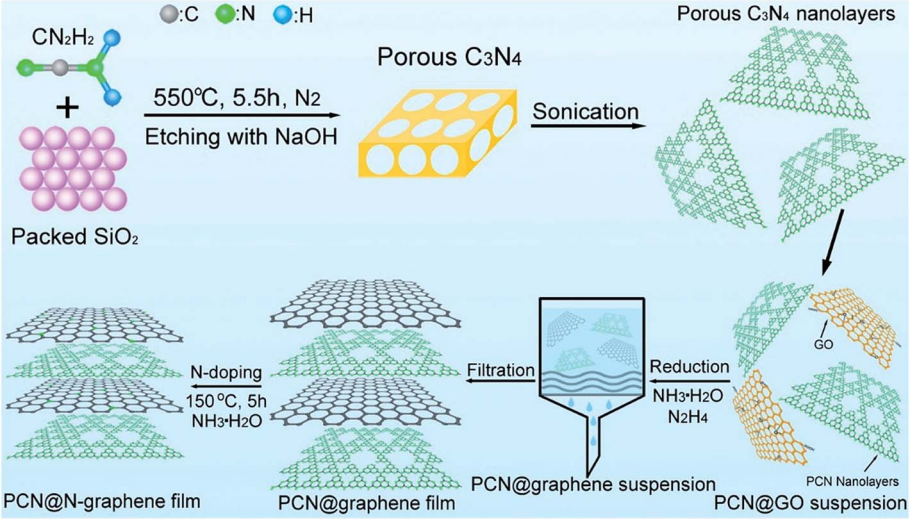

Fig. 56 Schematic illustration of the synthesis of a PCN@N-graphene film. Step (1): synthesis of porous C_3N_4 from cyanamide and SiO_2 nanoparticles followed by the removal of SiO_2 with NaOH, step (2): exfoliation to produce porous CN sheets, step (3): mixing of GO sheets with PCN, step (4): reduction of GO to rGO sheets with NH_2NH_2, and step (5): N-doping of rGO with liquid NH_3. Reproduced with permission from ref. 352 Copyright 2015 American Chemical Society.

thick g-C_3N_4 dots (MTCs) on the basal plane of reduced graphene oxide (MTCG) through self-assembly under hydrothermal conditions (Fig. 55).[109]

Furthermore, porous carbon nitride sheets synthesized by templating and sonication possess more exposed active sites and their integration with GO, followed by reduction under aqueous ammonia, produced a highly active porous carbon nitride/N-doped graphene (PCN@N-graphene) 2D network for the hydrogen evolution reaction with a very positive onset-potential comparable to that of commercial Pt (8 mV *vs.* 0 mV for Pt/C, *vs.* RHE@0.5 mA cm^{-2}) and excellent durability even after 5000 cycles (Fig. 56).[352] In addition, the band position tailored graphene and g-C_3N_4 was prepared by doping a nanoheterojunction in which charge can transfer from a high energy state to a lower energy state. For example, a 2D–2D n–p heterojunction of p-type B-doped reduced graphene oxide (B-rGO) and n-type oxygen-doped carbon nitride (O-g-C_3N_4) facilitated efficient charge separation at the system interface. The optimal loading of B-rGO on O-g-C_3N_4 was found to be 2 wt% which afforded 1639 μmol g^{-1} H_2 after 6 h of visible irradiation.[353] However, recent studies suggested that some doped carbon (S-doped) in the GCN-CS/C composite may degrade on the surface of g-C_3N_4 due to the oxidation of the doped carbon surface, resulting in a decrease in photocatalytic performance.[354] In contrast to graphene, some advanced graphene derivatives such as graphdiyne can also transport holes efficiently.[355] Furthermore, carbon and carbon nitrite nanocomposites have also been demonstrated to generate high hydrogen evolution rates without co-catalysts.[356,357] Other carbonaceous materials with an extended π-conjugated system, derived from cheap precursors, were also used for amalgamation with g-C_3N_4 sheets to achieve better charge separation.[358]

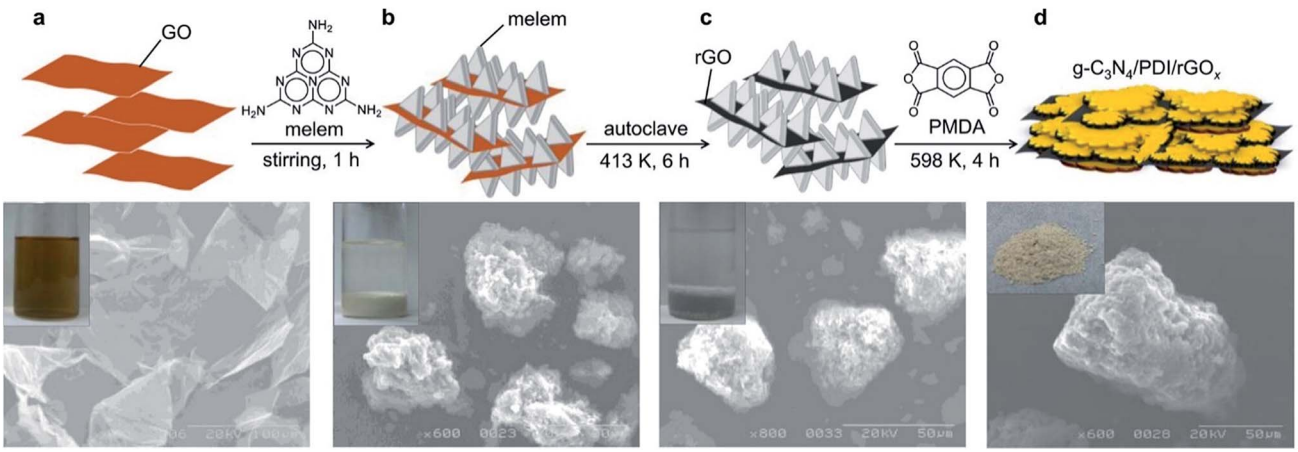

Fig. 57 Synthesis steps of g-C_3N_4/PDI/$rGO_{0.05}$ and corresponding SEM images of (a) GO, (b) melem loaded GO, (c) melem loaded rGO, and (d) g-C_3N_4/PDI/$rGO_{0.05}$. Reproduced with permission from ref. 360 Copyright 2016 American Chemical Society.

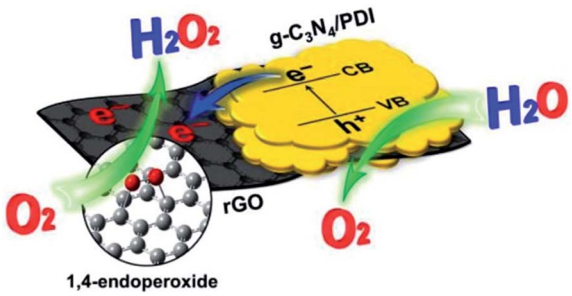

Fig. 58 Schematic representation of H_2O_2 production on the g-C_3N_4/PDI/rGO composite. Reproduced with permission from ref. 360 Copyright 2016 American Chemical Society.

For instance, a poly-(furfural alcohol)/g-C_3N_4 nanocomposite possessing a layered structure, synthesized by heating melamine and furfural alcohol, displayed better charge separation and a H_2 evolution rate as high as 584.7 μmol h^{-1} g^{-1}, which was roughly 4 times higher than that of pure g-C_3N_4 (156.2 μmol h^{-1} g^{-1}).[359]

The photoactivity of a carbon nitride-graphene system can be further increased by using polyimide (carbon nitride–aromatic diimide) which has better band alignment than carbon nitride. Kofuji *et al.* prepared a carbon nitride–aromatic diimide–graphene (g-C_3N_4/PDI/$rGO_{0.05}$) layered framework by deposition of melem on graphene oxide, followed by hydrothermal reduction of GO to rGO and finally polyimide formation by thermal annealing with PMDA.[360] The C_3N_4/PDI/$rGO_{0.05}$ composite exhibited excellent photoactivity for water oxidation to H_2O_2, on a millimole scale under simulated sunlight (Fig. 57 and 58). A metal-free g-C_3N_4/PDI-BN-rGO ternary hybrid photocatalyst containing boron nitride in place of carbon nitride was also reported for hydrogen peroxide production from water and oxygen using solar light as the activation source.[361] The solar to chemical conversion efficiency of g-C_3N_4/PDI-BN-rGO was calculated to be 0.27%, which was the highest reported efficiency for water splitting over powder photocatalysts.

Although the sandwich of carbon nitride and graphene network revealed better photocatalytic performance, there are certain bottlenecks for the practical application. For instance, the hydrogen evolved during the photocatalytic process is always contaminated with stoichiometric amounts of oxygen, which makes the isolation of hydrogen difficult due to the possibility of back reactions and explosion. Recently, some reports highlighted that graphene based materials, *i.e.*, doped, metal doped pillared graphene, alloy decorated graphene, *etc.*, have a promising ability to absorb hydrogen.[362–364] Moreover, Geim *et al.* demonstrated that a graphene sheet is only permeable for protons, while impermeable for other atoms, which can be used for filtering protons from other anions under an electrical bias.[365] Hence, the careful arrangement of carbon nitride as a water splitting catalyst, graphene as a proton filter and hydrogen storage material can provide a practical solution to the problem of hydrogen separation and storage of photo-generated hydrogen and oxygen mixtures. Inspired by these findings, Yang *et al.* constructed a multi-layer simulated model (computational) of carbon nitride sandwiched between two graphene sheets functionalized with different functionalities (Fig. 59). These studies suggested that this system can harvest solar light and generate electron–hole pairs. The holes can migrate to outer graphene sheets and facilitate water oxidation to generate protons, which can penetrate through graphene and react with photoelectrons on carbon nitride to produce hydrogen molecules that can be stored in the sandwiched structure at high density. The obtained results gave inspiration for the development of photocatalytic hydrogen generation and capsule storage to commercialize the technology.[366]

In contrast to a 2D assembly, graphitic carbon nitride frameworks can be assembled in 1D or 3D architectures by

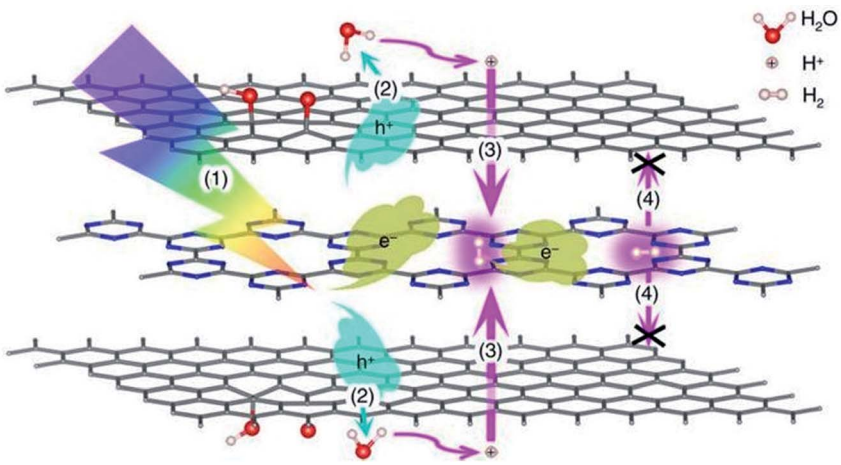

Fig. 59 The photocatalytic (water splitting) hydrogen generation and capsule storage scheme: (1) photo-generated electron (e^-) and hole (h^+) separation; (2) water splitting to produce protons (H^+) through the attack of holes (h^+); (3) protons (H^+) penetrating through GO and producing H_2 molecules; (4) H_2 molecules are prohibited from moving out of the sandwich. Here GO–CN–GO is used as an example. Blue, grey, pink and red beads stand for N, C, H (H^+) and O atoms, respectively; the yellow and light blue clouds are for photo-generated electrons (e^-) and holes (h^+), respectively, and the blue and magenta arrows represent the migration of corresponding particles. Reproduced with permission from ref. 366 Copyright Nature Publishing Group.

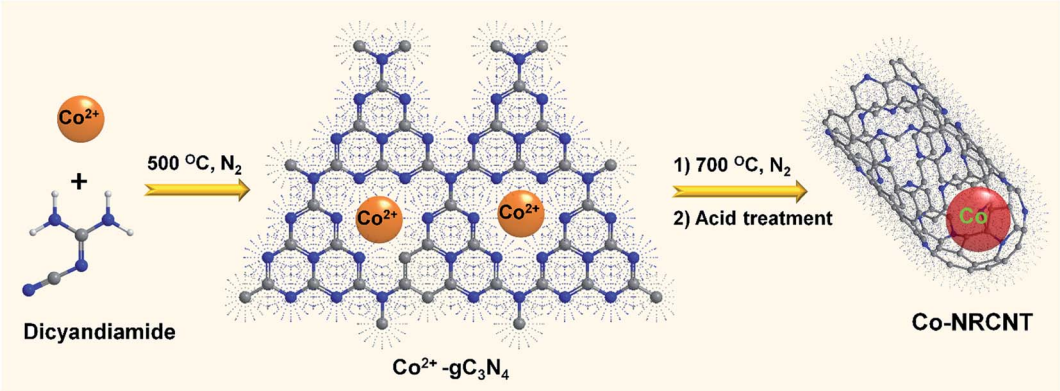

Fig. 60 Step (1): formation of Co^{2+}–g-C_3N_4 from dicyandiamide and $CoCl_2 \cdot 6H_2O$ at 500 °C under a N_2 atmosphere; step (2): formation of Co–NRCNTs from Co^{2+}–g-C_3N_4 by additional thermal treatment at 700 °C under a N_2 atmosphere and subsequent removal of accessible cobalt species by acid treatment. Adapted with permission from ref. 368.

pyrolysis or thermal oxidation of graphite and g-C_3N_4, followed by hydrothermal treatment.[367] Carbon nitride is stable up to 650 °C and heating above this temperature in air degrades the heptazine network with the evolution of ammonia. However, the heating of carbon nitride based materials at high temperature (approx. 900 °C) under an inert atmosphere can be a source of nitrogen-rich graphene or nanotubes. Generally, metal-free pyrolysis affords sheets while the incorporation of a metal precursor during the pyrolysis process yields nanotubes. The growth of nanotubes is favored, because *in situ* generated metal nanoparticles provide a surface for the growth of nanotubes and deposition and condensation take place on their surface. Inherently, doped-carbon materials have good performance for solar water splitting and this behavior extends to the nanotubes. In a report by Zou *et al.*, cobalt embedded nitrogen-rich carbon nanotube (Co–NRCNTs) synthesis was achieved by heating dicyandiamine impregnated with cobalt at 700 °C (Fig. 60). XPS analysis revealed that the N/C ratio in CNTs was 5.2 : 100, which was believed to be responsible for excellent performance for the hydrogen evolution reaction comparable to Pt as well as the ability to work in a wide pH range (0.0 to 14.0).[368] However, there is not a strict rule that only nanotubes will be obtained; if the temperature is fairly below 900 °C then only carbon materials can be obtained even if a metal salt is used. For example, cobalt-tungsten carbide embedded in a carbon network was produced at 700 °C and successfully applied for hydrogen evolution in alkaline solution.[369] Apart from annealing temperature, the chemical composition of monomeric materials also governs the morphological and compositional properties of materials. For instance, the hydrothermal treatment of a melamine precursor at 180 °C in the presence of NaOH and subsequent calcination at 650 °C lead to the formation of sodium-doped carbon nitride nanotubes.[370] The synthesized nanotubes displayed excellent photocatalytic performance for visible light induced water splitting. The doping of Na^+ ions between nitrogen-rich cavities allowed better charge separation. The use of two different monomeric units can also lead to a nanotube morphology, *i.e.*, a mixture of urea and oxamide triggered the formation of a nanotube structure which due to low energy n → π* transition evolved hydrogen even for photons of wavelengths longer than 465 nm.[371]

13. Inorganic/carbonaceous 2D/2D hybrids photocatalysts

Recently two-dimensional (2D) inorganic materials, composed of a few atom thick layers, have shown great potential for various applications owing to their fascinating physical, chemical and electronic properties.[372–374] The hybridization of inorganic 2D semiconductor sheets with carbon based materials is highly promising to achieve excellent photocatalytic performance due to strong face-to-face interactions and better availability of a large surface area, which facilitate efficient charge transfer from the inorganic 2D semiconductor to carbonaceous 2D sheets.[355,375] Additionally, carbon based sheets insulate 2D inorganic sheets which enhances the longevity and reusability of the materials. In recent years, numerous inorganic semiconductors possessing a layered structure such as boron nitride (hBN), SnS_2, MoS_2, GaS, WS_2, black phosphorous, phosphorene and LDHs have been reported which can be easily peeled off into a nanosheet morphology.[374,376–378] The transformation of bulk materials into few atom thick 2D nanosheets induces changes in optical as well as electronic properties. For instance, the transformation of bulk WS_2 to a nanosheet structure promotes indirect to direct band gap transition along with increased absorption (400–700 nm), which makes it an efficient photosensitizer.[379,380] A WS_2/CN 2D/2D nanosheet composite was prepared by mixing ultrasonically exfoliated WS_2 and thermally exfoliated carbon nitride sheets followed by decoration with CdS quantum dots by an immersion method.[381] The developed 2D/2D assembly displayed a promising hydrogen evolution rate (1174.5 μmol g^{-1} h^{-1}), which is approximately 67 times higher than that of pure CN nanosheets (17.2 μmol g^{-1} h^{-1}) in the presence of triethanolamine (TEOA) and without any co-catalyst. PL spectra of the CdS/WS_2/CN ternary composite were found to decrease in intensity compared to the spectra of

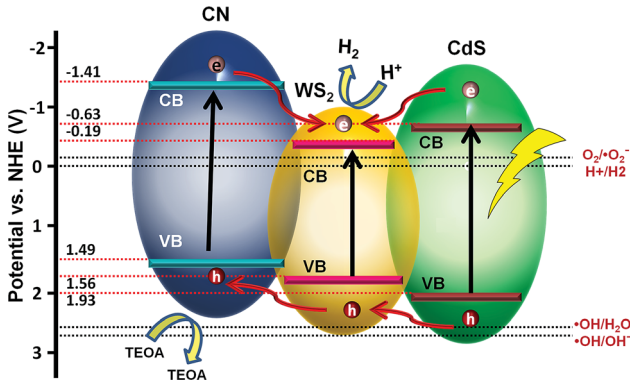

Fig. 61 Proposed mechanism of charge transfer in the $CdS/WS_2/CN$ photocatalyst revealing the relative band edge potential of each component with respect to the redox potential of $O_2/^{\cdot}O_2^-$, $^{\cdot}OH/H_2O$, H^+/H_2, and $OH^-/^{\cdot}OH$. Adapted with permission from ref. 381.

individual components or binary composites, indicating superior charge separation in ternary composite materials. On the basis of EIS and band gap values, the band structure of each component was calculated to elucidate the photocatalytic mechanism of the $CdS/WS_2/CN$ ternary composite. From Mott–Schottky plots (by assuming negligible difference between flat band potentials and the Fermi level), the CB position was calculated to be −1.41, −0.63 and −0.19 V *vs.* NHE for CN, CdS, and WS_2, respectively, while from the Tauc plot the band gap values were found to be 2.90, 2.56, and 1.75 eV corresponding to valence band positions of +1.49, +1.93, and +1.56 V *vs.* NHE, respectively. From the obtained band structure, it was concluded that in the $CdS/WS_2/CN$ composite, the photogenerated electrons move to WS_2 to reduce protons to hydrogen while holes move from CdS → WS_2 → CN and TEOA is oxidized on carbon nitride (Fig. 61).

Recently, black phosphorus (BP), a new 2D material possessing a tunable band gap (0.3–2 eV) and high electron mobility, has emerged as a promising candidate for various applications. Like carbon nitride, bulk black phosphorous can be delaminated into a sheet structure by solvent-assisted exfoliation.[382] By exploiting this phenomenon, a 2D–2D nanocomposite of BP and g-C_3N_4 sheets (CNS) was prepared in water (exfoliating agent) which promoted C–P bond formation and charge redistribution, leading to efficient charge separation. The obtained BPCNS photocatalyst showed excellent performance in photocatalytic nitrogen fixation.[383] EPR spectra of CNS and BP displayed signals of almost equal intensity due to unpaired electrons in π-conjugated aromatic rings, which upon hybridization in BPCNS became more intense revealing that the electrons in BPCNS were present in a more energetic excited state due to the change in the electronic character by the formation of C–P bonds. Some layered double hydroxides (LDHs) or ion exchange inorganic layered materials, composed of positively charged layers (+2, +3, or +4 oxidation states) octahedrally surrounded by oxo-bridges and hydroxyl groups and some negatively charged anions intercalated into the gallery to compensate excess charges, also behave as photocatalysts for hydrogen evolution from water,[384] *i.e.*, N-doped or N- and S-co-doped $CsTaWO_6$ and $HTaWO_6$,[385] Ni–Zn/Cr LDH,[386] N-doped $K_4Nb_6O_{17}$, $KCa_2Nb_3O_{10}$, $K_2Ti_4O_9$, and $KTiNbO_5$ (ref. 387), *etc.* Like other layered materials, LDH sheets can be exfoliated with various solvents. Various LDHs and g-C_3N_4 2D/2D nanocomposites have been shown to be better photocatalysts for hydrogen generation due to superior charge carrier transfer between LDHs and g-C_3N_4.[388–390] Exfoliated ZnCr LDH nanosheets, upon hybridization with g-C_3N_4 sheets, exhibited 2.8 times increase in the hydrogen evolution rate (186.97 μmol h^{-1} g^{-1}) over pristine g-C_3N_4 (65.23 μmol h^{-1} g^{-1}). Type II band alignment was present, which facilitated electron transfer from g-C_3N_4 sheets to LDHs, while holes from LDHs moved to g-C_3N_4 sheets.[391]

14. Other 2D carbonaceous photocatalysts

Apart from these materials, various other carbonaceous materials (either individually or hybridized with other materials) were also investigated for water splitting reactions. For instance, a porphyrin containing 2D polymer (2DP) was synthesized by Schiff-base condensation reaction between tertamino functionalized porphyrin and 2,5-dihydroxyterephthalaldehyde (Fig. 62). The 2D polymer possessing Co atoms in its porphyrin skeleton was a good hydrogen evolving catalyst and its activity was found to be more than that of other homogeneous coronation cobalt based catalysts (Co–N_4).[392] Similarly, a metal-free porphyrin based covalent organic polymer (TpPAM) was synthesized by condensation reaction between triformyl phloroglucinol (Tp) and 5,10,15,20-tetra(4-aminophenyl)-21H,23H-porphyrin (PAM). The synthesized TpPAM demonstrated excellent performance in electrocatalytic hydrogen evolution with a current density of 10 mA cm^{-2} at a low overpotential of 250 mV.[393]

The molecular catalysts of cobalt dithiolene display good photoactivity for hydrogen evolution and their continuous network prepared from trinucleating conjugated ligands, benzenehexathiol (BHT), and cobalt(II) further accelerates the hydrogen evolution rate.[394]

The biggest challenge with graphene chemistry is to tune the band gap for various applications and nitrogen doping seems to be the most suitable strategy. However, harsh reaction conditions, poor control, and limited doping restrict their application. In recent years, a 2D material, nitrogenated holey graphene (C_2N-h2D crystal), having a 2 : 1 stoichiometric ratio of carbon and nitrogen (C_2N) with equally distributed holes, has attracted the attention of the scientific community to drive research in the field.[113] Due to the small direct band gap of C_2N (1.96 eV) and porous nature, it opens new avenues for several applications such as photocatalysis, energy storage, electronics, gas storage, *etc.* The C_2N-h2D crystal structure can be easily synthesized by the reaction of hexaaminobenzene (HAB) trihydrochloride and hexaketocyclohexane (HKH) octahydrate using NMP as the solvent and a few drops of H_2SO_4 as the initiator (Fig. 63).

The band gap and band structure of C_2N-h2D can be manipulated by changing the order of stacking and the number

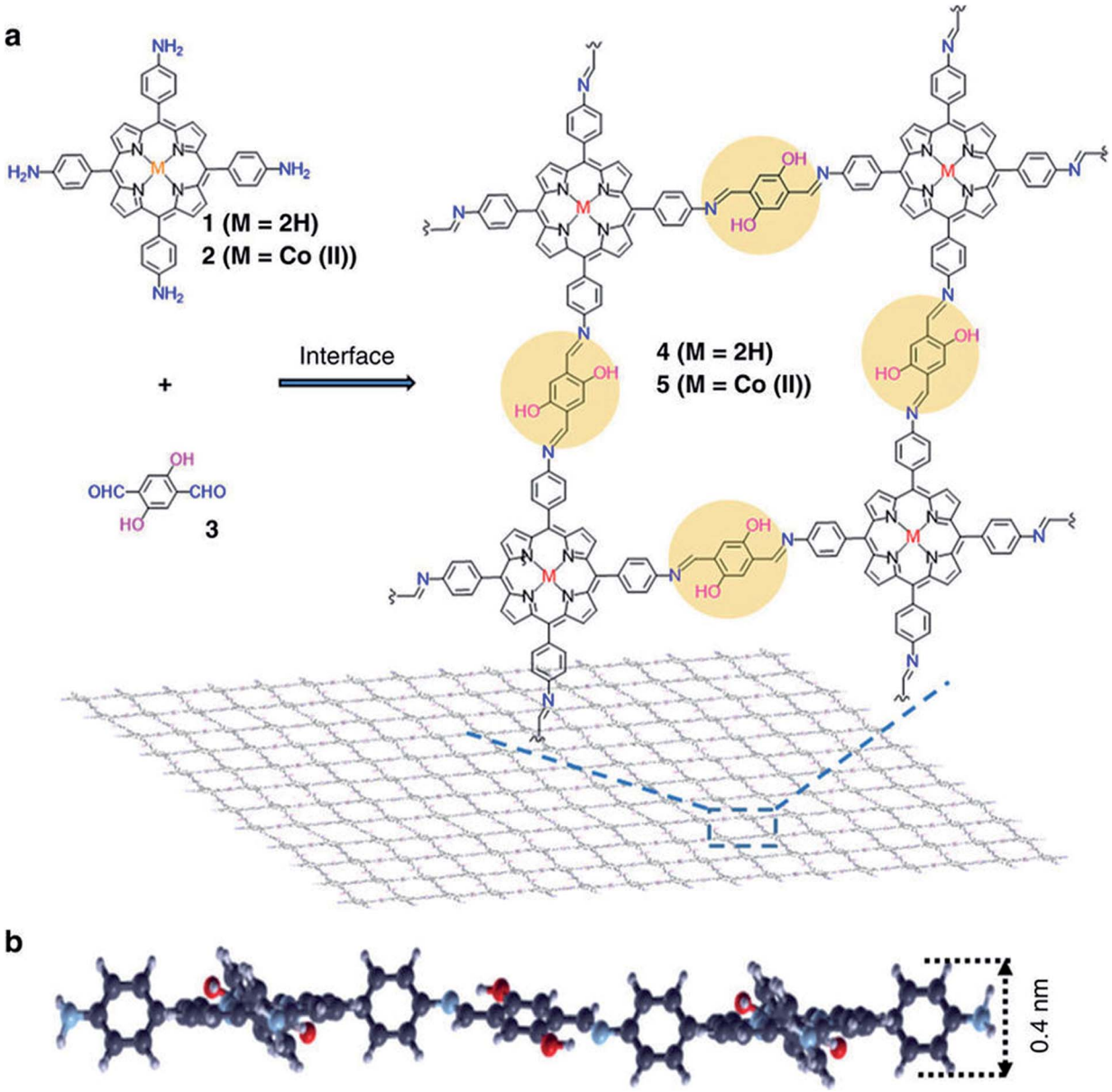

Fig. 62 Schematic illustration of Schiff-base condensation reaction between tertamino functionalized porphyrin and 2,5-dihydroxyterephthalaldehyde at an interface to form a 2D polymer (2DP). Reproduced with permission from ref. 392 Copyright 2016 Nature Publishing Group.

of layers.[395] Theoretical studies on single layer to few layered materials clearly indicated the potential application of the material as a metal-free water splitting photocatalyst.[396] Furthermore, the electronic structure of C_2N/graphene showed that C_2N can break the symmetry of the graphene sub-lattice and create a band gap of 0.40 eV in graphene, which can be further increased up to 0.72 eV if the interlayer distance was decreased up to 3.2 Å.[397] In another report, a band gap opening of 0.239 eV was predicted by g-C_2N stacking on graphene due to the imposition of an electrostatic potential by the g-C_2N substrate over the graphene layer.[398] Further investigation of the heterostructured g-C_3N_4/C_2N composite showed a suitable band edge position to sustain the process of water splitting (Fig. 64).[114] It has been demonstrated, on the basis of DFT theory, that transition metals such as Sc, Ti, V, Cr, Mn, Fe, and Co get embedded in between voids (and stabilized) and show ferromagnetic behavior, while Cu displays paramagnetic character.[399] Holey graphene (g-C_2N) can also accommodate high atomic radius lanthanides in the cavity, which leads to reduction in the band gap and half metallic character.[400]

In a theoretical investigation by Yagmurcukardes *et al.*, it was reported that similar to nitrogenated holey graphene (C_2N), other holey graphene structures such as phosphorated (C_2P) and arsenicated (C_2As) monolayers were energetically feasible and have a direct band gap.[401] Kishore *et al.* also made a similar prediction of a reduced band gap on the basis of DFT studies and investigated the effect of dopant concentration on band gap narrowing.[402] Like C_2N-h2D crystals, a two dimensional

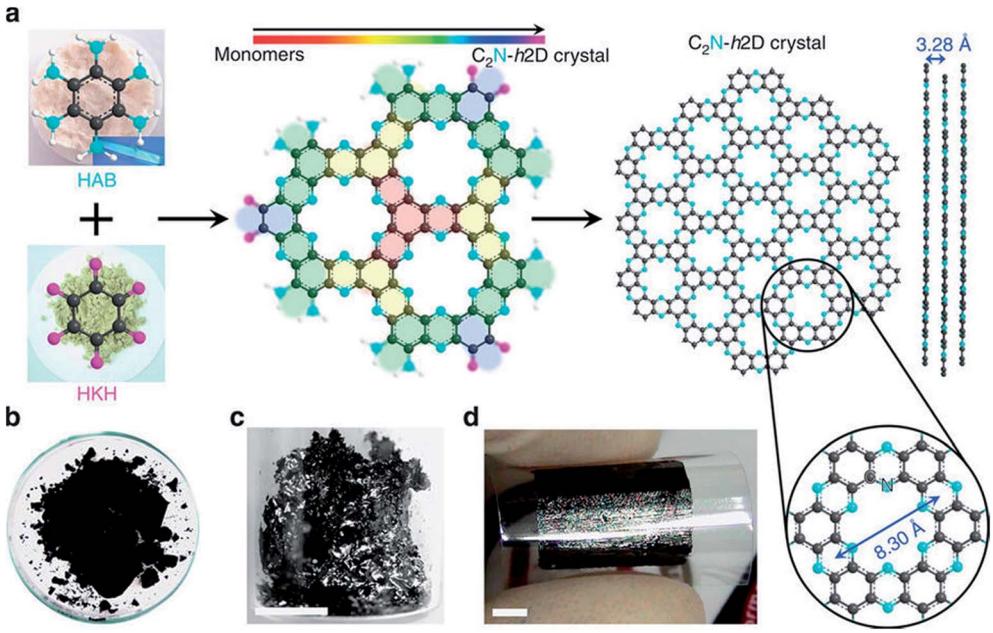

Fig. 63 (a) The synthesis strategy of C_2N-h2D crystals from hexaaminobenzene (HAB) trihydrochloride and hexaketocyclohexane (HKH) octahydrate. The inset in the image of HAB is a polarized optical microscopy image of the HAB single crystal. Digital photographs: (b) as-prepared C_2N-h2D crystal; (c) solution-cast C_2N-h2D crystal on a SiO_2 surface after heat-treatment at 700 °C; (d) a C_2N-h2D crystal film (thickness: approximately 330 nm) transferred onto a PET substrate. The shiny metallic reflection of the sample indicates that it is highly crystalline. Reproduced with permission from ref. 113 Copyright 2015 Nature Publishing Group.

polyaniline (2D PANI) structure having the empirical formula C_3N was obtained by pyrolysis of hexaaminobenzene trihydrochloride single crystals in the solid state having a HOMO–LUMO gap of 2.7 eV, which in turn can have future applications in photocatalysis and electronics (Fig. 65).[403] Due to the presence of ordered cavity defects in the C_2N-h2D structure, many small gas molecules can occupy this space, which provides an opportunity for future application in gas storage and gas sensing.[404] A similar 2D poly(triazine imide) polymer having a 3.88 Å cavity size was predicted to accommodate smaller molecules like CO_2 and N_2, and can be proved to be an excellent material for gas storage.[405] The properties of a 2D network of CdS/C_2N were predicted by DFT calculations, which revealed that the positions of the CBM and VBM of C_2N were 0.76 eV and 0.44 eV lower than those of CdS, which favors type-II band alignment where photogenerated electrons can migrate from CdS to C_2N, while holes move in the opposite direction. These findings suggest that CdS/C_2N photocatalyst represents a promising candidate for noble metal-free water splitting.[406] Similarly, the 2D nanocomposite of MoS_2 and C_2N was anticipated with a direct band gap of 1.3 eV and a band structure of type II configuration in which electrons flow from MoS_2 to C_2N.[407]

Carbonaceous quantum dots such as carbon quantum dots (CQDs) and carbon nitride quantum dots (CNQDs) due to their specific optical and surface chemistry have emerged as new

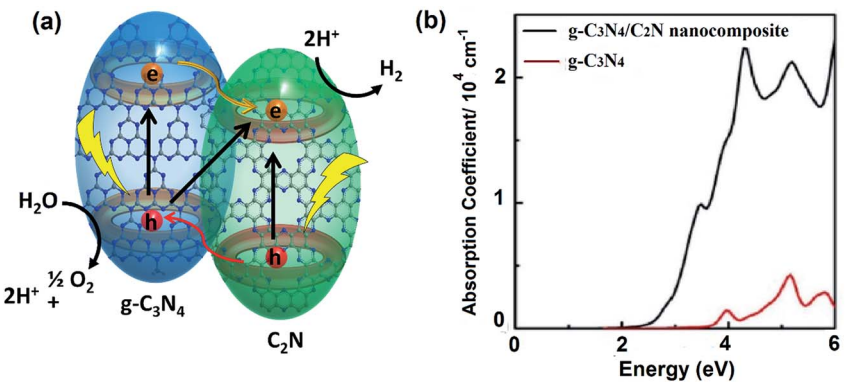

Fig. 64 (a) Generation of electron–hole pairs in the g-C_3N_4/C_2N nanocomposite by three possible routes (adapted from ref. 114); (b) the comparative optical absorption coefficients of the g-C_3N_4/C_2N nanocomposite and g-C_3N_4. Reproduced with permission from ref. 114 Copyright 2016 Wiley-VCH.

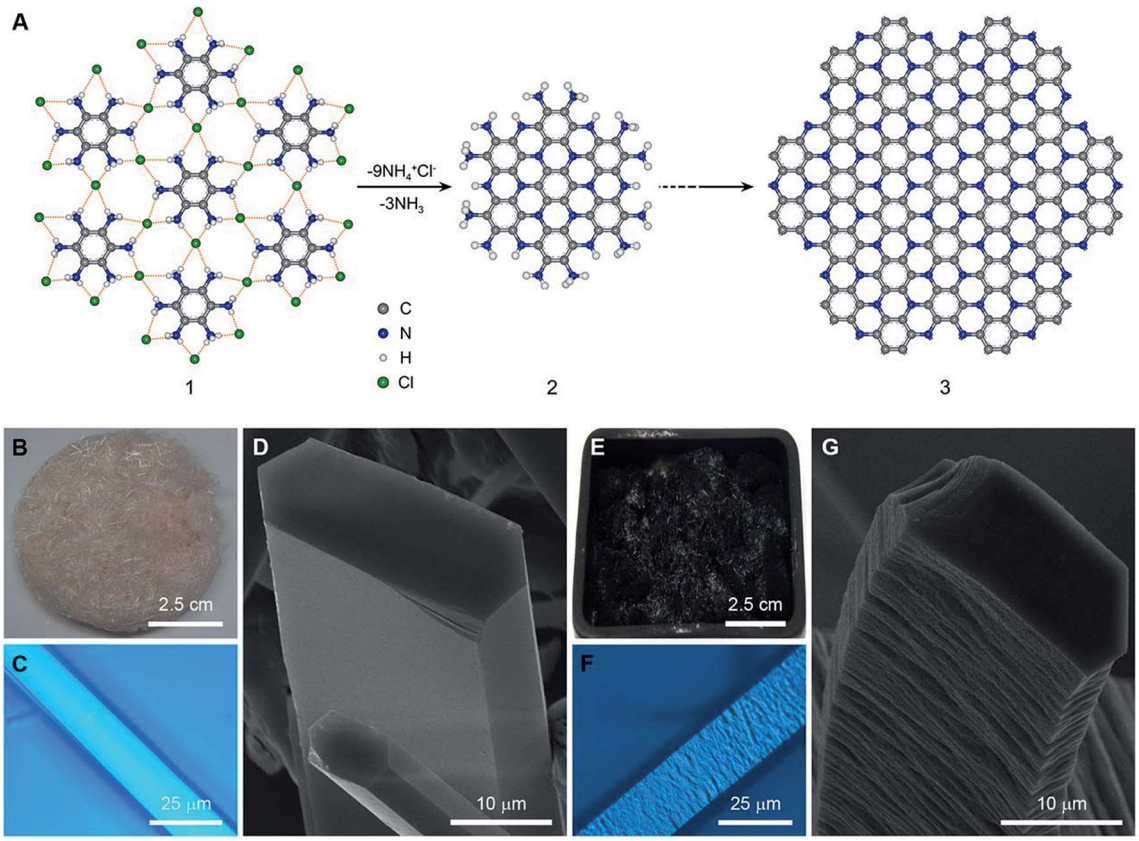

Fig. 65 (A) The synthesis outline of 2D PANI from hexaaminobenzene trihydrochloride (HAB). (1) Single-crystal X-ray packing structure of HAB, (2) structure of a 2D PANI unit with edge groups, C_3NH, and (3) the spontaneous transformation of the HAB crystal unit into the 2D PANI structure. Morphological changes of HAB crystals into 2D PANI frameworks. (B) Digital photograph of HAB crystals on butter paper. (C) Optical microscopy image of a needle-like HAB crystal before annealing. (D) SEM image of an HAB single crystal before annealing. (E) Digital image of HAB after annealing at 500 °C. (F) Optical microscopy image of a 2D PANI crystal after annealing at 500 °C. (G) SEM image of a 2D PANI single crystal after annealing. Reproduced with permission from ref. 403. Copyright 2016 PNAS.

materials for various applications like bioimaging, fluorescent materials, photovoltaics, photodetection, photocatalysis, catalysis, energy storage and photosensitization.[408–410] CQDs are aggregates of chemically bonded sp^2 and sp^3 hybridized amorphous to nanocrystalline quasi-spherical carbon nanoparticles composed of graphitic or turbostratic carbon, or graphene and graphene oxide sheet fragments.[411] Carbon quantum dots can be synthesized by top-down or bottom up approaches. The top-down approach includes breaking of large sheets of carbonaceous materials, graphene/graphene oxide sheets, to small fragments by chemical or physical means while in the bottom up approach, small molecules (like glucose, sucrose, EDTA, *etc.*) after thermal carbonization and/or hydrolysis in the presence of solvent (water) yield carbon quantum dots. Due to the occurrence of hydrolysis and carbonization steps simultaneously, the surface of carbon quantum dots may possess plenty of oxygen groups which provide better dispersibility, broadening of the band gap, specific optical properties and the possibility of surface functionalization. Graphene quantum dots (GQDs) are a class of carbon quantum dots that possess a few layered graphene structure of sp^2 hybridized carbon and are derived from graphene, graphene oxide or benzene ring containing compounds.[412] Although in a strict sense, quantum dots can be considered as zero dimensional materials due to their small size but due to their similar graphenic structure and chemical nature, they can be considered as 2D derivatives of bulk carbon nanosheets. The band gap of quantum dots strongly depends on the particle size due to the quantum confinement effect (increase with decrease in size and *vice versa*) and provides an opportunity to tune the band gap for desired applications. However, the quantum confinement effect is not always present (hence more appropriate to call these materials carbon dots or CDs rather than CQDs) and more research is needed in this field to explore other parameters responsible for optical properties.[77] Apart from the intensively investigated application of CDs as luminescent materials, photocatalytic application was also explored with CDs.[413,414] CDs act as photosensitizers and electron reservoirs due to their electron donating and accepting nature and this property has been used for their hybridization with various semiconductors for water splitting reactions.[54,415–418] For example, P25 TiO_2 composites (CQDs/P25), prepared by one step hydrothermal reaction, showed good water splitting due to better sensitization of TiO_2 and capture of electrons by CDs to prevent them from recombining.[419] A hydrogen evolution rate of 9.1 μmol h^{-1}, which was approximately four times higher than that of pure P25, was observed

for 1.5 wt% CQD loaded P25 nanoparticles. In another study, GQDs were covalently immobilized on a ZnO nanowire array grown on F-doped tin oxide (F-SnO_2) by using a 3-aminopropyltriethoxysilane (APTES) linker and used as a photosensitizer for photoelectrochemical water splitting.[420] A hexagonal tin disulfide (SnS_2) sheet network, which possesses a visible-light band gap (2.2–2.4 eV), was grown on a FTO (fluorine-doped tin oxide) surface with a 10 nm thick nickel nanoparticle layer. Carbon dots were decorated on this assembly and the grown network exhibited an excellent oxygen evolution rate (1.1 mmol g^{-1} h^{-1}) under simulated sunlight.[421] Independently, reduced graphene quantum dots (rGQDs) were deposited on Fe_2O_3 nanorods by self-assembling negatively charged graphene oxide quantum dots on Fe_2O_3, followed by thermal reduction to rGO quantum dots. The rGQDs/Fe_2O_3 structure generated increased photocurrent density due to the passivation of Fe_2O_3 electrodes by rGQDs and heat treatment.[422] Molecular catalyst/metal complexes, *i.e.*, nickel bis(diphosphine) complex grafted quantum dots, have also been used for solar hydrogen production.[423] A Prussian blue modified carbon dot (PB/CD) composite was found to be a good photocatalyst and promoted visible light mediated oxidative cyanation of tertiary amines.[424] Like graphene and carbon based materials, the optical properties of CQDs and GQDs can be tuned for enhanced photocatalytic applications by doping with heteroatoms.[77,425–427] As carbon dots possess a band gap, the phenomenon of charge recombination also exists with carbon dots. Photoreductive metal doping by reduction of metal by photogenerated electrons achieved better surface functionalization of CQDs, which prevented charge recombination and achieved a better quantum yield (*i.e.*, gold doping).[428] Also the decoration of CQDs on g-C_3N_4 sheets displayed an improved hydrogen production rate.[429,430] Carbon quantum dots embedded in g-C_3N_4 sheets (2D CQD/C_3N_4), prepared by spot heating, displayed excellent hydrogen evolution activity (152 μmol g^{-1} h^{-1}).[431] DFT calculations suggested that the CQDs/C_3N_4 system possesses a transition energy state in the middle of the band gap, which reduces the effective band gap along with the facilitation of electron diffusion *via* a polaron hopping mechanism. Interestingly, the CQDs/C_3N_4 system showed a surface plasmon resonance between 450 and 800 nm, which was believed to be responsible for the extended visible light activity of the photocatalyst. Many metal and plasmonic nanoparticles based carbon nitride photocatalysts have been previously reported which utilized the SPR effect for harvesting photons in the visible spectral regime.[432–434] Like CQDs and GQDs, carbon nitride quantum dots (CNQDs) have become popular due to their easy synthesis, tunable band gap, nanoscale processability and high stability. CNQDs are preferred over CQDs due to their easy preparation, high quantum yield, low toxicity, cheap production, good biocompatibility and promising photostability. Carbon nitride CNQDs can be synthesized by heating N-rich precursors such as urea, formamide, EDA, CCl_4, thiourea, *N*,*N*′-dimethyl formamide (DMF), *etc.*, at low temperature (180–200 °C) in a solid phase reaction to maintain a small size.[435–437] Specific functional group rich CNQDs can be prepared by carefully choosing functionalized precursor molecules. For example, phenyl modified CNQDs can be prepared using reaction of cyanuric acid and 2,4-diamino-6-phenyl-1,3,5-triazine.[438] Bulk carbon nitride in which carbon nitride sheets are interconnected with strong hydrogen bonds between NH and $-NH_2$ of the melon unit can be separated into nanosheets by thermal etching, which after sequential slicing with acid and base or hydrothermal treatment can be converted into CNQDs. Wang *et al.* synthesized CNQDs in a multi-step process: thermal etching of bulk g-C_3N_4 into sheets, which upon treatment with H_2SO_4 and HNO_3 generate carbon nitride nanoribbons (CNNRs) by oxidation of C–N bonds which connect the tri-*s*-triazine units, and finally hydrothermal treatment transforms these nanoribbons into CNQDs.[439] The prepared CNQDs displayed blue luminescence and wavelength-dependent PL spectra, and the PL intensity shifted to longer wavelengths when the excitation wavelength was varied from 340 to 420 nm. Furthermore, it was demonstrated that CNQDs exhibit up-conversion properties and excitation with longer wavelength photons (705–862 nm) causes them to emit at smaller wavelengths (350–600 nm); this property holds promise for potential application of CNQDs for the conversion of NIR light to visible light. By utilizing a top down approach, quantum dots doped with various heteroatoms, which possess better fluorescence and electronic characteristics, can be synthesized. F-doped CNQDs with an increased PL quantum yield were prepared by ultrasonication-assisted slicing of bulk sheets.[440] By using a CNQD–g-C_3N_4 suspension with the addition of 1 wt% Pt as a co-catalyst and 10% triethanolamine as a sacrificial donor, a 109.96 μmol h^{-1} H_2 production rate can be achieved. Furthermore, CNQDs can be used for building heterojunctions with other semiconductor materials for enhancing their photocatalytic activity.[441] For instance, CNQDs attached to a TiO_2 nanotube array (TNTA) by physical and chemical interaction through hydrothermal treatment showed excellent photocatalytic activity for water splitting and dye degradation.[442,443] The bonding between TiO_2 nanotubes and CNQDs can be further enhanced by using organic linkers. CNQDs covalently immobilized on TNTAs by use of the bifunctional linker 3-mercaptopropionic acid (MPA), which binds with –OH of TiO_2 and –COOH on the surface of CNQDs, displayed good photocatalytic activity for rhodamine B degradation and water splitting.[444] The enhanced photocatalytic performance was due to the direct injection of photogenerated charge on CNQDs to the conduction band of TiO_2. The doping of CNQDs with heteroatoms can further improve the quantum yield, *i.e.*, O and S co-doped graphitic carbon nitride quantum dots (OS-GCNQDs), prepared by thermal treatment of thiourea and citric acid, achieved a 14.5% quantum yield.[445]

15. Conclusion

To meet the steadily increasing global energy demand and cope with the rising concentrations of greenhouse gases in the atmosphere, there is a strong need to find and deploy environmentally benign renewable sources of energy, which do not leave any carbon footprint. In this arena, photo-assisted hydrogen generation using earth abundant sustainable materials is key to the alternative energy economy, while limiting

global warming. Research in this area is focused on the development of robust and efficient photocatalytic materials, which can sustain the process of water splitting by supplying charge carriers to the oxidation and reduction reactions. Among various nanomaterials, two dimensional carbonaceous materials have been envisaged as future photocatalysts due to their fascinating properties such as high specific surface area, visible light absorption and excellent charge carrier mobility. Graphene, graphene oxide, carbon nitride and carbon quantum dot based materials have been thoroughly investigated for visible light induced water splitting and their synthesis methods, structural variations and photocatalytic activities have been summarized in this report. In semiconductor-graphene hybrids, the conjugated network of carbon in graphene sheets facilitates better charge transportation on its surface to achieve efficient charge separation. However, the absence of a band gap restricts the role of graphene sheets to charge transport channels in composite materials. The introduction of defects into graphene by means of doping with heteroatoms or oxidation can transform conductive sheets into semiconducting sheets and the band gap can be tuned. However, achieving a high dopant concentration and chemical robustness is challenging. On the other hand, carbon nitride (g-C_3N_4) with excellent C : N stoichiometry and alternate C, N atomic configuration possesses a suitable band gap and favorable band edge positions to drive efficient water splitting. Excellent stability, easy fabrication from earth abundant materials, high porosity, favorable band potentials and an ample number of active sites for substrate binding make them highly promising candidate materials for alternative fuel technology. The facile exfoliation of bulk semiconducting g-C_3N_4 to form graphene-like sheets is an appealing route toward achieving a high surface area and exposed active sites for participation in photocatalytic processes. The red shift of the absorption profile by sensitization, doping and blending with other semiconductors further improves the performance for hydrogen evolution. The absorption coefficient of bulk graphitic semiconductors needs to be increased, and one way to accomplish this would be to incorporate highly polarizable heavier divalent and trivalent atoms into the framework. Another way is to form nanocomposites between 3D- and 2D-carbonitrides with one prominent example discussed in this review being a g-C_3N_4/C_2N nanocomposite, which shows a dramatically increased optical density. Band gap tuning and the manipulation of the band edge position of the basic carbon nitride framework by doping and introducing newer compositional units are the most exciting routes for developing breakthrough water splitting photocatalysts. Certain other 2D semiconductor catalysts with an entirely different composition such as C_2N, C_3N, and polyimides, are also interesting new photocatalytic materials due to their extraordinary optical and photocatalytic properties. In the next few years, the achievement of significant and scalable quantities of reaction products without the use of sacrificial donors is needed for practical realization. Despite certain drawbacks, the results with carbon based 2D materials are promising and these materials in the future will prove to be more efficient, cheap and robust photocatalysts for the production of clean hydrogen fuel. In our view, polymeric photocatalysts with new compositions that contain the basic carbon nitride framework modified with suitable units will be engineered to exhibit optimal visible light absorbance and tuned band positions. Divergent graphenic framework polymers constitute another avenue for developing impressive and robust photocatalysts. The possibility of band structure manipulation by nanoscale chemical and physical structural modification of carbonaceous materials is an attractive approach to harvest maximum energy residing in the solar spectrum to produce hydrogen with higher quantum yields.

Conflicts of interest

There are no conflicts to declare.

Acknowledgements

K. S. and P. K. thank NSERC (#06630), Future Energy Systems (#T12-P02) and NRC-NINT for financial support. RB acknowledges financial support from the Centre National de la Recherche Scientifique (CNRS), The University of Lille, and the Hauts-de-France region.

References

1 S. Chu and A. Majumdar, *Nature*, 2012, **488**, 294–303.
2 M. I. Hoffert, K. Calderia, A. K. Jain and E. F. Haites, *Nature*, 1998, **395**, 881.
3 R. M. Navarro, M. C. Alvarez-Galvan, J. A. V. de la Mano, S. M. Al-Zahrani and J. L. G. Fierro, *Energy Environ. Sci.*, 2010, **3**, 1865–1882.
4 N. S. Lewis and D. G. Nocera, *Proc. Natl. Acad. Sci. U. S. A.*, 2006, **103**, 15729–15735.
5 K. H. Nealson and P. G. Conrad, *Philos. Trans. R. Soc. London, Ser. B*, 1999, **354**, 1923–1939.
6 H. Zhou, T. Fan and D. Zhang, *ChemCatChem*, 2011, **3**, 513–528.
7 D. Chemisana, *Renewable Sustainable Energy Rev.*, 2011, **15**, 603–611.
8 L. El Chaar and N. El Zein, *Renewable Sustainable Energy Rev.*, 2011, **15**, 2165–2175.
9 A. Züttel, A. Borgschulte and L. Schlapbach, *Hydrogen as a future energy carrier*, John Wiley & Sons, 2011.
10 J. A. Turner, *Science*, 2004, **305**, 972–974.
11 R. M. Navarro, M. Pena and J. Fierro, *Chem. Rev.*, 2007, **107**, 3952–3991.
12 J. H. Montoya, L. C. Seitz, P. Chakthranont, A. Vojvodic, T. F. Jaramillo and J. K. Nørskov, *Nat. Mater.*, 2017, **16**, 70–81.
13 A. Fujishima and K. Honda, *Nature*, 1972, **238**, 37–38.
14 A. J. Bard, *J. Photochem.*, 1979, **10**, 59–75.
15 R. M. Navarro Yerga, M. C. Álvarez Galván, F. Del Valle, J. A. Villoria de la Mano and J. L. Fierro, *ChemSusChem*, 2009, **2**, 471–485.
16 S. Anantharaj, S. R. Ede, K. Sakthikumar, K. Karthick, S. Mishra and S. Kundu, *ACS Catal.*, 2016, **6**, 8069–8097.
17 S. N. Habisreutinger, L. Schmidt-Mende and J. K. Stolarczyk, *Angew. Chem., Int. Ed.*, 2013, **52**, 7372–7408.

18 G. Rothenberger, D. Fitzmaurice and M. Graetzel, *J. Phys. Chem.*, 1992, **96**, 5983–5986.
19 M. Tahir and N. S. Amin, *Energy Convers. Manage.*, 2013, **76**, 194–214.
20 J. Tian, Q. Liu, A. M. Asiri and X. Sun, *J. Am. Chem. Soc.*, 2014, **136**, 7587–7590.
21 Q. Zhang, Z. Li, S. Wang, R. Li, X. Zhang, Z. Liang, H. Han, S. Liao and C. Li, *ACS Catal.*, 2016, **6**, 2182–2191.
22 Y. Tang, Y. Su, N. Yang, L. Zhang and Y. Lv, *Anal. Chem.*, 2014, **86**, 4528–4535.
23 B. Sørensen, *Renewable energy conversion, transmission, and storage*, Academic press, 2007.
24 S. Farsinezhad, H. Sharma and K. Shankar, *Phys. Chem. Chem. Phys.*, 2015, **17**, 29723–29733.
25 P. Kar, S. Farsinezhad, N. Mahdi, Y. Zhang, U. Obuekwe, H. Sharma, J. Shen, N. Semagina and K. Shankar, *Nano Res.*, 2016, **9**, 3478–3493.
26 E. Mirzakulova, R. Khatmullin, J. Walpita, T. Corrigan, N. M. Vargas-Barbosa, S. Vyas, S. Oottikkal, S. F. Manzer, C. M. Hadad and K. D. Glusac, *Nat. Chem.*, 2012, **4**, 794–801.
27 R. Subbaraman, D. Tripkovic, K.-C. Chang, D. Strmcnik, A. P. Paulikas, P. Hirunsit, M. Chan, J. Greeley, V. Stamenkovic and N. M. Markovic, *Nat. Mater.*, 2012, **11**, 550–557.
28 J. Yang, D. Wang, H. Han and C. Li, *Acc. Chem. Res.*, 2013, **46**, 1900–1909.
29 M. Murdoch, G. Waterhouse, M. Nadeem, J. Metson, M. Keane, R. Howe, J. Llorca and H. Idriss, *Nat. Chem.*, 2011, **3**, 489–492.
30 E. L. Warren, H. A. Atwater and N. S. Lewis, *J. Phys. Chem. C*, 2013, **118**, 747–759.
31 A. Mohammadpour, B. Wiltshire, Y. Zhang, S. Farsinezhad, A. Askar, R. Kisslinger, Y. Ren, P. Kar and K. Shankar, *Nanotechnology*, 2017, **28**, 144001.
32 A. Mohammadpour, P. Kar, B. D Wiltshire, A. M Askar and K. Shankar, *Curr. Nanosci.*, 2015, **11**, 593–614.
33 V. Subramanian, E. E. Wolf and P. V. Kamat, *J. Am. Chem. Soc.*, 2004, **126**, 4943–4950.
34 M. Long, W. Cai, J. Cai, B. Zhou, X. Chai and Y. Wu, *J. Phys. Chem. B*, 2006, **110**, 20211–20216.
35 Z. He, Y. Shi, C. Gao, L. Wen, J. Chen and S. Song, *J. Phys. Chem. C*, 2013, **118**, 389–398.
36 P. Zhou, J. Yu and M. Jaroniec, *Adv. Mater.*, 2014, **26**, 4920–4935.
37 K. Maeda, *ACS Catal.*, 2013, **3**, 1486–1503.
38 Q. Wang, T. Hisatomi, Q. Jia, H. Tokudome, M. Zhong, C. Wang, Z. Pan, T. Takata, M. Nakabayashi and N. Shibata, *Nat. Mater.*, 2016, **15**, 611–615.
39 Y. Sasaki, H. Nemoto, K. Saito and A. Kudo, *J. Phys. Chem. C*, 2009, **113**, 17536–17542.
40 S. Fu, H. Niu, Z. Tao, J. Song, C. Mao, S. Zhang, C. Chen and D. Wang, *J. Alloys Compd.*, 2013, **576**, 5–12.
41 Y. Sasaki, H. Kato and A. Kudo, *J. Am. Chem. Soc.*, 2013, **135**, 5441–5449.
42 A. Iwase, Y. H. Ng, Y. Ishiguro, A. Kudo and R. Amal, *J. Am. Chem. Soc.*, 2011, **133**, 11054–11057.
43 Q. Xiang and J. Yu, *J. Phys. Chem. Lett.*, 2013, **4**, 753–759.
44 G. Algara-Siller, N. Severin, S. Y. Chong, T. Björkman, R. G. Palgrave, A. Laybourn, M. Antonietti, Y. Z. Khimyak, A. V. Krasheninnikov and J. P. Rabe, *Angew. Chem.*, 2014, **126**, 7580–7585.
45 X. Meng and Z. Zisheng, *Catal. Today*, 2018, DOI: 10.1016/j.cattod.2018.03.015.
46 B. Luo, G. Liu and L. Wang, *Nanoscale*, 2016, **8**, 6904–6920.
47 S. Cao and J. Yu, *J. Photochem. Photobiol., C*, 2016, **27**, 72–99.
48 J. Zhang, Y. Chen and X. Wang, *Energy Environ. Sci.*, 2015, **8**, 3092–3108.
49 C. Li, Y. Xu, W. Tu, G. Chen and R. Xu, *Green Chem.*, 2017, **19**, 882–899.
50 G. Zhao, Y. Cheng, Y. Wu, X. Xu and X. Hao, *Small*, 2018, **14**, 1704138.
51 Y. Yang, S. Wang, Y. Li, J. Wang and L. Wang, *Chem.–Asian J.*, 2017, **12**, 1421–1434.
52 L. Jiang, X. Yuan, G. Zeng, J. Liang, Z. Wu and H. Wang, *Environ. Sci.: Nano*, 2018, **5**, 599–615.
53 X. Zou and Y. Zhang, *Chem. Soc. Rev.*, 2015, **44**, 5148–5180.
54 Y. Zheng, Y. Jiao, Y. Zhu, L. H. Li, Y. Han, Y. Chen, A. Du, M. Jaroniec and S. Z. Qiao, *Nat. Commun.*, 2014, **5**, 3783.
55 X.-K. Kong, C.-L. Chen and Q.-W. Chen, *Chem. Soc. Rev.*, 2014, **43**, 2841–2857.
56 X. Li, J. Yu, S. Wageh, A. A. Al-Ghamdi and J. Xie, *Small*, 2016, **12**, 6640–6696.
57 Q. Xiang, B. Cheng and J. Yu, *Angew. Chem., Int. Ed.*, 2015, **54**, 11350–11366.
58 F. Perreault, A. F. De Faria and M. Elimelech, *Chem. Soc. Rev.*, 2015, **44**, 5861–5896.
59 M.-Q. Yang, N. Zhang, M. Pagliaro and Y.-J. Xu, *Chem. Soc. Rev.*, 2014, **43**, 8240–8254.
60 Q. Xiang, J. Yu and M. Jaroniec, *Chem. Soc. Rev.*, 2012, **41**, 782–796.
61 Q. Xiang, J. Yu and M. Jaroniec, *Nanoscale*, 2011, **3**, 3670–3678.
62 X. Xie, K. Kretschmer and G. Wang, *Nanoscale*, 2015, **7**, 13278–13292.
63 Y. Jia, L. Zhang, A. Du, G. Gao, J. Chen, X. Yan, C. L. Brown and X. Yao, *Adv. Mater.*, 2016, **28**, 9532–9538.
64 S. Kawai, S. Saito, S. Osumi, S. Yamaguchi, A. S. Foster, P. Spijker and E. Meyer, *Nat. Commun.*, 2015, **6**, 8098.
65 T. H. Han, S. J. Kwon, N. Li, H. K. Seo, W. Xu, K. S. Kim and T. W. Lee, *Angew. Chem., Int. Ed.*, 2016, **55**, 6197–6201.
66 S. Dou, A. Shen, L. Tao and S. Wang, *Chem. Commun.*, 2014, **50**, 10672–10675.
67 X. Wang, J. Wang, D. Wang, S. Dou, Z. Ma, J. Wu, L. Tao, A. Shen, C. Ouyang and Q. Liu, *Chem. Commun.*, 2014, **50**, 4839–4842.
68 L. K. Putri, W.-J. Ong, W. S. Chang and S.-P. Chai, *Appl. Surf. Sci.*, 2015, **358**, 2–14.
69 J. Duan, S. Chen, M. Jaroniec and S. Z. Qiao, *ACS Catal.*, 2015, **5**, 5207–5234.
70 Z. Shi, A. Kutana and B. I. Yakobson, *J. Phys. Chem. Lett.*, 2015, **6**, 106–112.
71 P. Zhang, J. Zhang and S. Dai, *Chem.–Eur. J.*, 2017, **23**, 1986–1998.

72 S. Huang, Y. Meng, S. He, A. Goswami, Q. Wu, J. Li, S. Tong, T. Asefa and M. Wu, *Adv. Funct. Mater.*, 2017, **27**, 1606585.
73 J. Zhang, L. Qu, G. Shi, J. Liu, J. Chen and L. Dai, *Angew. Chem., Int. Ed.*, 2016, **55**, 2230–2234.
74 G. Xu, J. Han, B. Ding, P. Nie, J. Pan, H. Dou, H. Li and X. Zhang, *Green Chem.*, 2015, **17**, 1668–1674.
75 T. F. Yeh, J. M. Syu, C. Cheng, T. H. Chang and H. Teng, *Adv. Funct. Mater.*, 2010, **20**, 2255–2262.
76 T. F. Yeh, C. Y. Teng, S. J. Chen and H. Teng, *Adv. Mater.*, 2014, **26**, 3297–3303.
77 J. Yang, D. Voiry, S. J. Ahn, D. Kang, A. Y. Kim, M. Chhowalla and H. S. Shin, *Angew. Chem., Int. Ed.*, 2013, **52**, 13751–13754.
78 R. Leary and A. Westwood, *Carbon*, 2011, **49**, 741–772.
79 S. Min and G. Lu, *Int. J. Hydrogen Energy*, 2012, **37**, 10564–10574.
80 Y. Zheng, L. Lin, B. Wang and X. Wang, *Angew. Chem., Int. Ed.*, 2015, **54**, 12868–12884.
81 M. Zhang and X. Wang, *Energy Environ. Sci.*, 2014, **7**, 1902–1906.
82 F. K. Kessler, Y. Zheng, D. Schwarz, C. Merschjann, W. Schnick, X. Wang and M. J. Bojdys, *Nat. Rev. Mater.*, 2017, **2**, 17030.
83 S. Cao, J. Low, J. Yu and M. Jaroniec, *Adv. Mater.*, 2015, **27**, 2150–2176.
84 W.-J. Ong, L.-L. Tan, Y. H. Ng, S.-T. Yong and S.-P. Chai, *Chem. Rev.*, 2016, **116**, 7159–7329.
85 K. S. Lakhi, D.-H. Park, K. Al-Bahily, W. Cha, B. Viswanathan, J.-H. Choy and A. Vinu, *Chem. Soc. Rev.*, 2017, **46**, 72–101.
86 G. Zhang, Z.-A. Lan, L. Lin, S. Lin and X. Wang, *Chem. Sci.*, 2016, **7**, 3062–3066.
87 X. Wang, K. Maeda, A. Thomas, K. Takanabe, G. Xin, J. M. Carlsson, K. Domen and M. Antonietti, *Nat. Mater.*, 2009, **8**, 76–80.
88 D. J. Martin, P. J. T. Reardon, S. J. Moniz and J. Tang, *J. Am. Chem. Soc.*, 2014, **136**, 12568–12571.
89 X. Wang, S. Blechert and M. Antonietti, *ACS Catal.*, 2012, **2**, 1596–1606.
90 Z. Zhou, Y. Zhang, Y. Shen, S. Liu and Y. Zhang, *Chem. Soc. Rev.*, 2018, **47**, 2298–2321.
91 J. Liu, H. Wang and M. Antonietti, *Chem. Soc. Rev.*, 2016, **45**, 2308–2326.
92 Z. Zhao, Y. Sun and F. Dong, *Nanoscale*, 2015, **7**, 15–37.
93 L. Jiang, X. Yuan, Y. Pan, J. Liang, G. Zeng, Z. Wu and H. Wang, *Appl. Catal., B*, 2017, **217**, 388–406.
94 J. Ran, T. Y. Ma, G. Gao, X.-W. Du and S. Z. Qiao, *Energy Environ. Sci.*, 2015, **8**, 3708–3717.
95 L. Zhou, H. Zhang, H. Sun, S. Liu, M. O. Tade, S. Wang and W. Jin, *Catal. Sci. Technol.*, 2016, **6**, 7002–7023.
96 M. Zhang, X. Bai, D. Liu, J. Wang and Y. Zhu, *Appl. Catal., B*, 2015, **164**, 77–81.
97 S. Tonda, S. Kumar, S. Kandula and V. Shanker, *J. Mater. Chem. A*, 2014, **2**, 6772–6780.
98 Y. Zhang, J. Liu, G. Wu and W. Chen, *Nanoscale*, 2012, **4**, 5300–5303.
99 S. Yang, Y. Gong, J. Zhang, L. Zhan, L. Ma, Z. Fang, R. Vajtai, X. Wang and P. M. Ajayan, *Adv. Mater.*, 2013, **25**, 2452–2456.
100 J. Xu, L. Zhang, R. Shi and Y. Zhu, *J. Mater. Chem. A*, 2013, **1**, 14766–14772.
101 P. Xia, B. Zhu, J. Yu, S. Cao and M. Jaroniec, *J. Mater. Chem. A*, 2017, **5**, 3230–3238.
102 X. Dong and F. Cheng, *J. Mater. Chem. A*, 2015, **3**, 23642–23652.
103 K. Schwinghammer, M. B. Mesch, V. Duppel, C. Ziegler, J. r. Senker and B. V. Lotsch, *J. Am. Chem. Soc.*, 2014, **136**, 1730–1733.
104 H. Ou, L. Lin, Y. Zheng, P. Yang, Y. Fang and X. Wang, *Adv. Mater.*, 2017, **29**, 1700008.
105 Y. Kang, Y. Yang, L. C. Yin, X. Kang, L. Wang, G. Liu and H. M. Cheng, *Adv. Mater.*, 2016, **28**, 6471–6477.
106 W. Iqbal, B. Qiu, Q. Zhu, M. Xing and J. Zhang, *Appl. Catal., B*, 2018, **232**, 306–313.
107 Q. Liu, T. Chen, Y. Guo, Z. Zhang and X. Fang, *Appl. Catal., B*, 2016, **193**, 248–258.
108 W.-J. Ong, L.-L. Tan, S.-P. Chai, S.-T. Yong and A. R. Mohamed, *Nano Energy*, 2015, **13**, 757–770.
109 X. Wang, L. Wang, F. Zhao, C. Hu, Y. Zhao, Z. Zhang, S. Chen, G. Shi and L. Qu, *Nanoscale*, 2015, **7**, 3035–3042.
110 S. Chu, Y. Wang, C. Wang, J. Yang and Z. Zou, *Int. J. Hydrogen Energy*, 2013, **38**, 10768–10772.
111 S. Chu, Y. Wang, Y. Guo, P. Zhou, H. Yu, L. Luo, F. Kong and Z. Zou, *J. Mater. Chem.*, 2012, **22**, 15519–15521.
112 L. Lin, P. Ye, C. Cao, Q. Jin, G.-S. Xu, Y.-H. Shen and Y.-P. Yuan, *J. Mater. Chem. A*, 2015, **3**, 10205–10208.
113 J. Mahmood, E. K. Lee, M. Jung, D. Shin, I.-Y. Jeon, S.-M. Jung, H.-J. Choi, J.-M. Seo, S.-Y. Bae, S.-D. Sohn, N. Park, J. H. Oh, H. J. Shin and J.-B. Baek, *Nat. Commun.*, 2015, **6**, 6486.
114 H. Wang, X. Li and J. Yang, *ChemPhysChem*, 2016, **17**, 2100–2104.
115 O. V. Yazyev and Y. P. Chen, *Nat. Nanotechnol.*, 2014, **9**, 755–767.
116 O. C. Compton and S. T. Nguyen, *Small*, 2010, **6**, 711–723.
117 V. Singh, D. Joung, L. Zhai, S. Das, S. I. Khondaker and S. Seal, *Prog. Mater. Sci.*, 2011, **56**, 1178–1271.
118 D. R. Dreyer, R. S. Ruoff and C. W. Bielawski, *Angew. Chem., Int. Ed.*, 2010, **49**, 9336–9344.
119 A. K. Geim and K. S. Novoselov, *Nat. Mater.*, 2007, **6**, 183–191.
120 K. S. Novoselov, V. Fal, L. Colombo, P. Gellert, M. Schwab and K. Kim, *Nature*, 2012, **490**, 192–200.
121 M. J. Allen, V. C. Tung and R. B. Kaner, *Chem. Rev.*, 2010, **110**, 132–145.
122 S. Navalon, A. Dhakshinamoorthy, M. Alvaro and H. Garcia, *Chem. Rev.*, 2014, **114**, 6179–6212.
123 Y. B. Tan and J.-M. Lee, *J. Mater. Chem. A*, 2013, **1**, 14814–14843.
124 M. Pumera, *Energy Environ. Sci.*, 2011, **4**, 668–674.
125 M. Pumera, *Mater. Today*, 2011, **14**, 308–315.
126 D. A. Dikin, S. Stankovich, E. J. Zimney, R. D. Piner, G. H. Dommett, G. Evmenenko, S. T. Nguyen and R. S. Ruoff, *Nature*, 2007, **448**, 457–460.

127 W. S. Hummers Jr and R. E. Offeman, *J. Am. Chem. Soc.*, 1958, **80**, 1339.
128 D. C. Marcano, D. V. Kosynkin, J. M. Berlin, A. Sinitskii, Z. Sun, A. Slesarev, L. B. Alemany, W. Lu and J. M. Tour, *ACS Nano*, 2010, **4**, 4806–4814.
129 Y. Zhu, S. Murali, W. Cai, X. Li, J. W. Suk, J. R. Potts and R. S. Ruoff, *Adv. Mater.*, 2010, **22**, 3906–3924.
130 P. Kumar, A. Kumar, C. Joshi, R. Boukherroub and S. L. Jain, Graphene–semiconductor hybrid photocatalysts and their application in solar fuel production, *Advanced 2D Materials*, ed. A. Tiwari and M. Mikael Syvajarvi, John Wiley & Sons, 2016, ch. 9, pp. 353–386.
131 P. Kumar, S. L. Jain and R. Boukherroub, Graphene-based nanocomposite materials for the photoreduction of carbon dioxide into valuable organic compounds, *Innovations in Nanomaterials*, ed. A.-N. Chowdhury, J. Shapter, and A. B. Imran, Nova Science Publishers, 2015, ch. 13, pp. 321–335.
132 R. Gusain, P. Kumar, O. P. Sharma, S. L. Jain and O. P. Khatri, *Appl. Catal., B*, 2016, **181**, 352–362.
133 P. Kumar, C. Joshi, A. Barras, B. Sieber, A. Addad, L. Boussekey, S. Szunerits, R. Boukherroub and S. L. Jain, *Appl. Catal., B*, 2017, **205**, 654–665.
134 Y. Sun, H. Cheng, S. Gao, Z. Sun, Q. Liu, Q. Liu, F. Lei, T. Yao, J. He and S. Wei, *Angew. Chem., Int. Ed.*, 2012, **51**, 8727–8731.
135 M.-Q. Yang and Y.-J. Xu, *J. Phys. Chem. C*, 2013, **117**, 21724–21734.
136 Y. Zhang, N. Zhang, Z.-R. Tang and Y.-J. Xu, *ACS Nano*, 2012, **6**, 9777–9789.
137 Y. Liang, Y. Li, H. Wang, J. Zhou, J. Wang, T. Regier and H. Dai, *Nat. Mater.*, 2011, **10**, 780–786.
138 Y. Tong, P. Chen, T. Zhou, K. Xu, W. Chu, C. Wu and Y. Xie, *Angew. Chem., Int. Ed.*, 2017, **56**, 7121–7125.
139 A. Cao, Z. Liu, S. Chu, M. Wu, Z. Ye, Z. Cai, Y. Chang, S. Wang, Q. Gong and Y. Liu, *Adv. Mater.*, 2010, **22**, 103–106.
140 P. Zeng, Q. Zhang, T. Peng and X. Zhang, *Phys. Chem. Chem. Phys.*, 2011, **13**, 21496–21502.
141 Q. Li, B. Guo, J. Yu, J. Ran, B. Zhang, H. Yan and J. R. Gong, *J. Am. Chem. Soc.*, 2011, **133**, 10878–10884.
142 L. Jia, D.-H. Wang, Y.-X. Huang, A.-W. Xu and H.-Q. Yu, *J. Phys. Chem. C*, 2011, **115**, 11466–11473.
143 M.-L. Guan, D.-K. Ma, S.-W. Hu, Y.-J. Chen and S.-M. Huang, *Inorg. Chem.*, 2010, **50**, 800–805.
144 X. Li, R. Huang, Y. Hu, Y. Chen, W. Liu, R. Yuan and Z. Li, *Inorg. Chem.*, 2012, **51**, 6245–6250.
145 J. Hou, Z. Wang, W. Kan, S. Jiao, H. Zhu and R. Kumar, *J. Mater. Chem.*, 2012, **22**, 7291–7299.
146 J. S. Lee, K. H. You and C. B. Park, *Adv. Mater.*, 2012, **24**, 1084–1088.
147 X. Wei, T. Xie, L. Peng, W. Fu, J. Chen, Q. Gao, G. Hong and D. Wang, *J. Phys. Chem. C*, 2011, **115**, 8637–8642.
148 G. Eda, C. Mattevi, H. Yamaguchi, H. Kim and M. Chhowalla, *J. Phys. Chem. C*, 2009, **113**, 15768–15771.
149 G. Eda, G. Fanchini and M. Chhowalla, *Nat. Nanotechnol.*, 2008, **3**, 270–274.
150 H.-C. Hsu, I. Shown, H.-Y. Wei, Y.-C. Chang, H.-Y. Du, Y.-G. Lin, C.-A. Tseng, C.-H. Wang, L.-C. Chen and Y.-C. Lin, *Nanoscale*, 2013, **5**, 262–268.
151 I. Shown, H.-C. Hsu, Y.-C. Chang, C.-H. Lin, P. K. Roy, A. Ganguly, C.-H. Wang, J.-K. Chang, C.-I. Wu and L.-C. Chen, *Nano Lett.*, 2014, **14**, 6097–6103.
152 T.-F. Yeh, S.-J. Chen and H. Teng, *Nano Energy*, 2015, **12**, 476–485.
153 L. C. Chen, C. Y. Teng, C. Y. Lin, H. Y. Chang, S. J. Chen and H. Teng, *Adv. Energy Mater.*, 2016, **6**, 1600719.
154 H. Tetsuka, R. Asahi, A. Nagoya, K. Okamoto, I. Tajima, R. Ohta and A. Okamoto, *Adv. Mater.*, 2012, **24**, 5333–5338.
155 H. Zhang, X. Lv, Y. Li, Y. Wang and J. Li, *ACS Nano*, 2009, **4**, 380–386.
156 N. Yang, J. Zhai, D. Wang, Y. Chen and L. Jiang, *ACS Nano*, 2010, **4**, 887–894.
157 T.-F. Yeh, J. Cihlář, C.-Y. Chang, C. Cheng and H. Teng, *Mater. Today*, 2013, **16**, 78–84.
158 P. Kumar, A. Kumar, B. Sreedhar, B. Sain, S. S. Ray and S. L. Jain, *Chem.–Eur. J.*, 2014, **20**, 6154–6161.
159 S. Kumar, P. Kumar and S. L. Jain, *J. Mater. Chem. A*, 2014, **2**, 18861–18866.
160 P. Kumar, G. Singh, D. Tripathi and S. L. Jain, *RSC Adv.*, 2014, **4**, 50331–50337.
161 P. Kumar, A. Bansiwal, N. Labhsetwar and S. L. Jain, *Green Chem.*, 2015, **17**, 1605–1609.
162 P. Kumar, B. Sain and S. L. Jain, *J. Mater. Chem. A*, 2014, **2**, 11246–11253.
163 P. Kumar, S. Kumar, S. Cordier, S. Paofai, R. Boukherroub and S. L. Jain, *RSC Adv.*, 2014, **4**, 10420–10423.
164 P. Kumar, H. P. Mungse, S. Cordier, R. Boukherroub, O. P. Khatri and S. L. Jain, *Carbon*, 2015, **94**, 91–100.
165 A. Kumar, P. Kumar, S. Paul and S. L. Jain, *Appl. Surf. Sci.*, 2016, **386**, 103–114.
166 P. Kumar, H. P. Mungse, O. P. Khatri and S. L. Jain, *RSC Adv.*, 2015, **5**, 54929–54935.
167 D. Wang, J. Huang, X. Li, P. Yang, Y. Du, C. M. Goh and C. Lu, *J. Mater. Chem. A*, 2015, **3**, 4195–4202.
168 S. Min and G. Lu, *J. Phys. Chem. C*, 2011, **115**, 13938–13945.
169 Z. Mou, Y. Dong, S. Li, Y. Du, X. Wang, P. Yang and S. Wang, *Int. J. Hydrogen Energy*, 2011, **36**, 8885–8893.
170 D. Deng, K. Novoselov, Q. Fu, N. Zheng, Z. Tian and X. Bao, *Nat. Nanotechnol.*, 2016, **11**, 218–230.
171 F. Karlicky, K. Kumara Ramanatha Datta, M. Otyepka and R. Zboril, *ACS Nano*, 2013, **7**, 6434–6464.
172 K.-I. Ho, C.-H. Huang, J.-H. Liao, W. Zhang, L.-J. Li, C.-S. Lai and C.-Y. Su, *Sci. Rep.*, 2014, **4**, 5893.
173 K.-J. Jeon, Z. Lee, E. Pollak, L. Moreschini, A. Bostwick, C.-M. Park, R. Mendelsberg, V. Radmilovic, R. Kostecki and T. J. Richardson, *ACS Nano*, 2011, **5**, 1042–1046.
174 B. Li, L. Zhou, D. Wu, H. Peng, K. Yan, Y. Zhou and Z. Liu, *ACS Nano*, 2011, **5**, 5957–5961.
175 A. Bakandritsos, M. Pykal, P. Błoński, P. Jakubec, D. D. Chronopoulos, K. Poláková, V. Georgakilas, K. Čépe, O. Tomanec and V. Ranc, *ACS Nano*, 2017, **11**, 2982–2991.

176 J. Tuček, K. Holá, A. B. Bourlinos, P. Błoński, A. Bakandritsos, J. Ugolotti, M. Dubecký, F. Karlický, V. Ranc and K. Čépe, *Nat. Commun.*, 2017, **8**, 14525.
177 D. Marquardt, F. Beckert, F. Pennetreau, F. Tölle, R. Mülhaupt, O. Riant, S. Hermans, J. Barthel and C. Janiak, *Carbon*, 2014, **66**, 285–294.
178 S. M. Kang, S. Park, D. Kim, S. Y. Park, R. S. Ruoff and H. Lee, *Adv. Funct. Mater.*, 2011, **21**, 108–112.
179 L. Dai, *Acc. Chem. Res.*, 2012, **46**, 31–42.
180 W. Dong, X. Li, J. Yu, W. Guo, B. Li, L. Tan, C. Li, J. Shi and G. Wang, *Mater. Lett.*, 2012, **67**, 131–134.
181 A. Lherbier, X. Blase, Y.-M. Niquet, F. Triozon and S. Roche, *Phys. Rev. Lett.*, 2008, **101**, 036808.
182 X.-F. Li, K.-Y. Lian, L. Liu, Y. Wu, Q. Qiu, J. Jiang, M. Deng and Y. Luo, *Sci. Rep.*, 2016, **6**, 23495.
183 L. Lai, J. R. Potts, D. Zhan, L. Wang, C. K. Poh, C. Tang, H. Gong, Z. Shen, J. Lin and R. S. Ruoff, *Energy Environ. Sci.*, 2012, **5**, 7936–7942.
184 Z.-H. Sheng, L. Shao, J.-J. Chen, W.-J. Bao, F.-B. Wang and X.-H. Xia, *ACS Nano*, 2011, **5**, 4350–4358.
185 X. Zhang, S. Liu, Y. Zang, R. Liu, G. Liu, G. Wang, Y. Zhang, H. Zhang and H. Zhao, *Nano Energy*, 2016, **30**, 93–102.
186 Y. Wen, B. Wang, C. Huang, L. Wang and D. Hulicova-Jurcakova, *Chem.–Eur. J.*, 2015, **21**, 80–85.
187 M. Latorre-Sánchez, A. Primo and H. García, *Angew. Chem., Int. Ed.*, 2013, **52**, 11813–11816.
188 Z. W. Liu, F. Peng, H. J. Wang, H. Yu, W. X. Zheng and J. Yang, *Angew. Chem.*, 2011, **123**, 3315–3319.
189 W. H. Lee, J. W. Suk, H. Chou, J. Lee, Y. Hao, Y. Wu, R. Piner, D. Akinwande, K. S. Kim and R. S. Ruoff, *Nano Lett.*, 2012, **12**, 2374–2378.
190 J. Liang, Y. Jiao, M. Jaroniec and S. Z. Qiao, *Angew. Chem., Int. Ed.*, 2012, **51**, 11496–11500.
191 Y. Zheng, Y. Jiao, L. Ge, M. Jaroniec and S. Z. Qiao, *Angew. Chem.*, 2013, **125**, 3192–3198.
192 X. Yue, S. Huang, J. Cai, Y. Jin and P. K. Shen, *J. Mater. Chem. A*, 2017, **5**, 7784–7790.
193 Y. Zheng, Y. Jiao, L. H. Li, T. Xing, Y. Chen, M. Jaroniec and S. Z. Qiao, *ACS Nano*, 2014, **8**, 5290–5296.
194 J. Zhang and L. Dai, *Angew. Chem.*, 2016, **128**, 13490–13494.
195 S. Chen and S.-Z. Qiao, *ACS Nano*, 2013, **7**, 10190–10196.
196 Y. Yang, F. He, Y. Shen, X. Chen, H. Mei, S. Liu and Y. Zhang, *Chem. Commun.*, 2017, **53**, 9994–9997.
197 M. Z. Rahman, K. Davey and S.-Z. Qiao, *J. Mater. Chem. A*, 2018, **6**, 1305–1322.
198 J.-t. Jin, X.-c. Qiao, F.-l. Cheng, H.-b. Fan and L.-f. Cui, *Carbon*, 2017, **122**, 114–121.
199 S. Yang, L. Peng, P. Huang, X. Wang, Y. Sun, C. Cao and W. Song, *Angew. Chem., Int. Ed.*, 2016, **55**, 4016–4020.
200 J. Sheng, L. Wang, L. Deng, M. Zhang, H. He, K. Zeng, F. Tang and Y.-N. Liu, *ACS Appl. Mater. Interfaces*, 2018, **10**, 7191–7200.
201 Y. Zhu, G. Chen, X. Xu, G. Yang, M. Liu and Z. Shao, *ACS Catal.*, 2017, **7**, 3540–3547.
202 X. Zhao, H. Yang, P. Jing, W. Shi, G. Yang and P. Cheng, *Small*, 2017, **13**, 1603279.
203 Y. Pan, K. Sun, S. Liu, X. Cao, K. Wu, W.-C. Cheong, Z. Chen, Y. Wang, Y. Li and Y. Liu, *J. Am. Chem. Soc.*, 2018, **140**, 2610–2618.
204 Y. Liang, Y. Li, H. Wang and H. Dai, *J. Am. Chem. Soc.*, 2013, **135**, 2013–2036.
205 Y. Zhu, G. Chen, Y. Zhong, W. Zhou and Z. Shao, *Adv. Sci.*, 2018, **5**, 1700603.
206 Y. Xu, W. Tu, B. Zhang, S. Yin, Y. Huang, M. Kraft and R. Xu, *Adv. Mater.*, 2017, **29**, 1605957.
207 C. Ray, S. C. Lee, B. Jin, A. Kundu, J. H. Park and S. C. Jun, *J. Mater. Chem. A*, 2018, **6**, 4466–4476.
208 H. Kim, Y. Kim, Y. Noh, S. Lee, J. Sung and W. B. Kim, *ChemCatChem*, 2017, **9**, 1503–1510.
209 Y. Liu, G. Yu, G. D. Li, Y. Sun, T. Asefa, W. Chen and X. Zou, *Angew. Chem., Int. Ed.*, 2015, **54**, 10752–10757.
210 C. Lu, D. Tranca, J. Zhang, F. n. Rodríguez Hernández, Y. Su, X. Zhuang, F. Zhang, G. Seifert and X. Feng, *ACS Nano*, 2017, **11**, 3933–3942.
211 S. Liu, H. Zhang, Q. Zhao, X. Zhang, R. Liu, X. Ge, G. Wang, H. Zhao and W. Cai, *Carbon*, 2016, **106**, 74–83.
212 S. Yanagida, A. Kabumoto, K. Mizumoto, C. Pac and K. Yoshino, *J. Chem. Soc., Chem. Commun.*, 1985, 474–475.
213 V. N. Khabashesku, J. L. Zimmerman and J. L. Margrave, *Chem. Mater.*, 2000, **12**, 3264–3270.
214 E. Kroke, *Angew. Chem., Int. Ed.*, 2014, **53**, 11134–11136.
215 W.-J. Ong, L.-L. Tan, Y. H. Ng, S.-T. Yong and S.-P. Chai, *Chem. Rev.*, 2016, **116**, 7159–7329.
216 X. Wang, K. Maeda, X. Chen, K. Takanabe, K. Domen, Y. Hou, X. Fu and M. Antonietti, *J. Am. Chem. Soc.*, 2009, **131**, 1680–1681.
217 D. J. Martin, K. Qiu, S. A. Shevlin, A. D. Handoko, X. Chen, Z. Guo and J. Tang, *Angew. Chem., Int. Ed.*, 2014, **53**, 9240–9245.
218 L. Shi, L. Liang, F. Wang, M. Liu, K. Chen, K. Sun, N. Zhang and J. Sun, *ACS Sustainable Chem. Eng.*, 2015, **3**, 3412–3419.
219 A. Jin, Y. Jia, C. Chen, X. Liu, J. Jiang, X. Chen and F. Zhang, *J. Phys. Chem. C*, 2017, **121**, 21497–21509.
220 I. Papailias, T. Giannakopoulou, N. Todorova, D. Demotikali, T. Vaimakis and C. Trapalis, *Appl. Surf. Sci.*, 2015, **358**, 278–286.
221 P. Niu, G. Liu and H.-M. Cheng, *J. Phys. Chem. C*, 2012, **116**, 11013–11018.
222 J. Li, M. Zhang, X. Li, Q. Li and J. Yang, *Appl. Catal., B*, 2017, **212**, 106–114.
223 M. R. Gholipour, F. Béland and T.-O. Do, *ACS Sustainable Chem. Eng.*, 2016, **5**, 213–220.
224 P. Niu, M. Qiao, Y. Li, L. Huang and T. Zhai, *Nano Energy*, 2018, **44**, 73–81.
225 F. Goettmann, A. Fischer, M. Antonietti and A. Thomas, *Angew. Chem.*, 2006, **118**, 4579–4583.
226 F. Su, S. C. Mathew, L. Möhlmann, M. Antonietti, X. Wang and S. Blechert, *Angew. Chem., Int. Ed.*, 2011, **50**, 657–660.
227 Y. Wang, J. Yao, H. Li, D. Su and M. Antonietti, *J. Am. Chem. Soc.*, 2011, **133**, 2362–2365.
228 J. Zhu, Y. Wei, W. Chen, Z. Zhao and A. Thomas, *Chem. Commun.*, 2010, **46**, 6965–6967.
229 S. Yang, X. Feng, X. Wang and K. Müllen, *Angew. Chem., Int. Ed.*, 2011, **50**, 5339–5343.

230 J. Hong, W. Zhang, Y. Wang, T. Zhou and R. Xu, *ChemCatChem*, 2014, **6**, 2315–2321.
231 F. Su, S. C. Mathew, G. Lipner, X. Fu, M. Antonietti, S. Blechert and X. Wang, *J. Am. Chem. Soc.*, 2010, **132**, 16299–16301.
232 X. Jin, V. V. Balasubramanian, S. T. Selvan, D. P. Sawant, M. A. Chari, G. e. Q. Lu and A. Vinu, *Angew. Chem.*, 2009, **121**, 8024–8027.
233 K. Datta, B. Reddy, K. Ariga and A. Vinu, *Angew. Chem., Int. Ed.*, 2010, **49**, 5961–5965.
234 X. Wang, X. Chen, A. Thomas, X. Fu and M. Antonietti, *Adv. Mater.*, 2009, **21**, 1609–1612.
235 K. Kailasam, A. Fischer, G. Zhang, J. Zhang, M. Schwarze, M. Schröder, X. Wang, R. Schomäcker and A. Thomas, *ChemSusChem*, 2015, **8**, 1404–1410.
236 D. Zeng, W. J. Ong, Y. Chen, S. Y. Tee, C. S. Chua, D. L. Peng and M. Y. Han, *Part. Part. Syst. Charact.*, 2018, **35**, 1700251.
237 S. Patnaik, D. P. Sahoo, L. Mohapatra, S. Martha and K. Parida, *Energy Technol.*, 2017, **5**, 1687–1701.
238 Z. Pan, Y. Zheng, F. Guo, P. Niu and X. Wang, *ChemSusChem*, 2017, **10**, 87–90.
239 W. Niu, Z. Li, K. Marcus, L. Zhou, Y. Li, R. Ye, K. Liang and Y. Yang, *Adv. Energy Mater.*, 2018, **8**, 1701642.
240 S. M. N. Jeghan, J. Y. Do and M. Kang, *J. Ind. Eng. Chem.*, 2018, **57**, 405–415.
241 A. Indra, A. Acharjya, P. W. Menezes, C. Merschjann, D. Hollmann, M. Schwarze, M. Aktas, A. Friedrich, S. Lochbrunner and A. Thomas, *Angew. Chem.*, 2017, **129**, 1675–1679.
242 W. Zou, Y. Shao, Y. Pu, Y. Luo, J. Sun, K. Ma, C. Tang, F. Gao and L. Dong, *Appl. Catal., B*, 2017, **218**, 51–59.
243 L. Song, T. Li and S. Zhang, *J. Phys. Chem. C*, 2016, **121**, 293–299.
244 Z. Yi, J. Ye, N. Kikugawa, T. Kako, S. Ouyang, H. Stuart-Williams, H. Yang, J. Cao, W. Luo and Z. Li, *Nat. Mater.*, 2010, **9**, 559–564.
245 X. Yang, H. Tang, J. Xu, M. Antonietti and M. Shalom, *ChemSusChem*, 2015, **8**, 1350–1358.
246 S. Kumar, T. Surendar, A. Baruah and V. Shanker, *J. Mater. Chem. A*, 2013, **1**, 5333–5340.
247 D. Jiang, J. Zhu, M. Chen and J. Xie, *J. Colloid Interface Sci.*, 2014, **417**, 115–120.
248 L. Tian, X. Xian, X. Cui, H. Tang and X. Yang, *Appl. Surf. Sci.*, 2018, **430**, 301–308.
249 Y. Zhang, T. Mori, J. Ye and M. Antonietti, *J. Am. Chem. Soc.*, 2010, **132**, 6294–6295.
250 Y. Zhou, L. Zhang, J. Liu, X. Fan, B. Wang, M. Wang, W. Ren, J. Wang, M. Li and J. Shi, *J. Mater. Chem. A*, 2015, **3**, 3862–3867.
251 S. Guo, Y. Tang, Y. Xie, C. Tian, Q. Feng, W. Zhou and B. Jiang, *Appl. Catal., B*, 2017, **218**, 664–671.
252 A. Kumar, P. Kumar, C. Joshi, M. Manchanda, R. Boukherroub and S. L. Jain, *Nanomaterials*, 2016, **6**, 59.
253 Y. Wang, J. Zhang, X. Wang, M. Antonietti and H. Li, *Angew. Chem., Int. Ed.*, 2010, **49**, 3356–3359.
254 Z. Lin and X. Wang, *Angew. Chem., Int. Ed.*, 2013, **52**, 1735–1738.
255 D. W. Stephan, *Org. Biomol. Chem.*, 2008, **6**, 1535–1539.
256 D. W. Stephan and G. Erker, *Angew. Chem.*, 2010, **122**, 50–81.
257 S. Thaweesak, S. Wang, M. Lyu, M. Xiao, P. Peerakiatkhajohn and L. Wang, *Dalton Trans.*, 2017, **46**, 10714–10720.
258 J. Zhu, T. Diao, W. Wang, X. Xu, X. Sun, S. A. Carabineiro and Z. Zhao, *Appl. Catal., B*, 2017, **219**, 92–100.
259 J. P. Paraknowitsch, J. Zhang, D. Su, A. Thomas and M. Antonietti, *Adv. Mater.*, 2010, **22**, 87–92.
260 G. P. Mane, S. N. Talapaneni, K. S. Lakhi, H. Ilbeygi, U. Ravon, K. Al-Bahily, T. Mori, D. H. Park and A. Vinu, *Angew. Chem., Int. Ed.*, 2017, **56**, 8481–8485.
261 S. N. Talapaneni, G. P. Mane, D.-H. Park, K. S. Lakhi, K. Ramadass, S. Joseph, W. M. Skinner, U. Ravon, K. Al-Bahily and A. Vinu, *J. Mater. Chem. A*, 2017, **5**, 18183–18192.
262 Y. Wang, Y. Di, M. Antonietti, H. Li, X. Chen and X. Wang, *Chem. Mater.*, 2010, **22**, 5119–5121.
263 L. Zeng, X. Ding, Z. Sun, W. Hua, W. Song, S. Liu and L. Huang, *Appl. Catal., B*, 2018, **227**, 276–284.
264 P. Zhang, X. Li, C. Shao and Y. Liu, *J. Mater. Chem. A*, 2015, **3**, 3281–3284.
265 P. Xiao, D. Jiang, T. Liu, D. Li and M. Chen, *Mater. Lett.*, 2018, **212**, 111–113.
266 W. Che, W. Cheng, T. Yao, F. Tang, W. Liu, H. Su, Y. Huang, Q. Liu, J. Liu and F. Hu, *J. Am. Chem. Soc.*, 2017, **139**, 3021–3026.
267 M. Z. Rahman, J. Moffatt and N. A. Spooner, *Mater. Horiz.*, 2018, **5**, 553–559.
268 H. Wang, B. Wang, Y. Bian and L. Dai, *ACS Appl. Mater. Interfaces*, 2017, **9**, 21730–21737.
269 V. S. Kale, U. Sim, J. Yang, K. Jin, S. I. Chae, W. J. Chang, A. K. Sinha, H. Ha, C. C. Hwang and J. An, *Small*, 2017, **13**, 1603893.
270 C. Liu, Y. Zhang, F. Dong, A. Reshak, L. Ye, N. Pinna, C. Zeng, T. Zhang and H. Huang, *Appl. Catal., B*, 2017, **203**, 465–474.
271 Z.-A. Lan, G. Zhang and X. Wang, *Appl. Catal., B*, 2016, **192**, 116–125.
272 S. Zhao, Y. Zhang, Y. Wang, Y. Zhou, K. Qiu, C. Zhang, J. Fang and X. Sheng, *J. Power Sources*, 2017, **370**, 106–113.
273 J. Xu, Y. Wang and Y. Zhu, *Langmuir*, 2013, **29**, 10566–10572.
274 Y. Wang, X. Wang, M. Antonietti and Y. Zhang, *ChemSusChem*, 2010, **3**, 435–439.
275 Y. S. Jun, W. H. Hong, M. Antonietti and A. Thomas, *Adv. Mater.*, 2009, **21**, 4270–4274.
276 M. Li, H. Wang, X. Li, S. Zhang, J. Han, A. F. Masters, T. Maschmeyer and X. Liu, *ChemCatChem*, 2018, **10**, 581–589.
277 K. Kailasam, J. D. Epping, A. Thomas, S. Losse and H. Junge, *Energy Environ. Sci.*, 2011, **4**, 4668–4674.
278 E. Z. Lee, Y. S. Jun, W. H. Hong, A. Thomas and M. M. Jin, *Angew. Chem., Int. Ed.*, 2010, **49**, 9706–9710.
279 J. Zhang, M. Zhang, C. Yang and X. Wang, *Adv. Mater.*, 2014, **26**, 4121–4126.
280 Y. S. Jun, E. Z. Lee, X. Wang, W. H. Hong, G. D. Stucky and A. Thomas, *Adv. Funct. Mater.*, 2013, **23**, 3661–3667.
281 Y. Guo, J. Li, Y. Yuan, L. Li, M. Zhang, C. Zhou and Z. Lin, *Angew. Chem., Int. Ed.*, 2016, **55**, 14693–14697.

282 Y. Wang, H. Wang, F. Chen, F. Cao, X. Zhao, S. Meng and Y. Cui, *Appl. Catal., B*, 2017, **206**, 417–425.
283 S. Zhao, Y. Zhang, Y. Zhou, Y. Wang, K. Qiu, C. Zhang, J. Fang and X. Sheng, *Carbon*, 2018, **126**, 247–256.
284 F. Wei, Y. Liu, H. Zhao, X. Ren, J. Liu, T. Hasan, L. Chen, Y. Li and B.-L. Su, *Nanoscale*, 2018, **10**, 4515–4522.
285 Y. Chen and X. Wang, *J. Phys. Chem. C*, 2018, **122**, 3786–3793.
286 Q. Liu, X. Wang, Q. Yang, Z. Zhang and X. Fang, *Appl. Catal., B*, 2018, **225**, 22–29.
287 B. V. Lotsch, M. Döblinger, J. Sehnert, L. Seyfarth, J. Senker, O. Oeckler and W. Schnick, *Chem.–Eur. J.*, 2007, **13**, 4969–4980.
288 P. Niu, L. Zhang, G. Liu and H. M. Cheng, *Adv. Funct. Mater.*, 2012, **22**, 4763–4770.
289 X. Zhang, X. Xie, H. Wang, J. Zhang, B. Pan and Y. Xie, *J. Am. Chem. Soc.*, 2013, **135**, 18–21.
290 X. She, H. Xu, Y. Xu, J. Yan, J. Xia, L. Xu, Y. Song, Y. Jiang, Q. Zhang and H. Li, *J. Mater. Chem. A*, 2014, **2**, 2563–2570.
291 Y. Yin, J. Han, X. Zhang, Y. Zhang, J. Zhou, D. Muir, R. Sutarto, Z. Zhang, S. Liu and B. Song, *RSC Adv.*, 2014, **4**, 32690–32697.
292 J. Ji, J. Wen, Y. Shen, Y. Lv, Y. Chen, S. Liu, H. Ma and Y. Zhang, *J. Am. Chem. Soc.*, 2017, **139**, 11698–11701.
293 M. Wu, J. M. Yan, X. n. Tang, M. Zhao and Q. Jiang, *ChemSusChem*, 2014, **7**, 2654–2658.
294 N. Cheng, P. Jiang, Q. Liu, J. Tian, A. M. Asiri and X. Sun, *Analyst*, 2014, **139**, 5065–5068.
295 X. Lu, K. Xu, P. Chen, K. Jia, S. Liu and C. Wu, *J. Mater. Chem. A*, 2014, **2**, 18924–18928.
296 S. Yu, R. D. Webster, Y. Zhou and X. Yan, *Catal. Sci. Technol.*, 2017, **7**, 2050–2056.
297 Y. Hong, C. Li, Z. Fang, B. Luo and W. Shi, *Carbon*, 2017, **121**, 463–471.
298 K. L. Corp and C. W. Schlenker, *J. Am. Chem. Soc.*, 2017, **139**, 7904–7912.
299 Q. Ruan, W. Luo, J. Xie, Y. Wang, X. Liu, Z. Bai, C. J. Carmalt and J. Tang, *Angew. Chem., Int. Ed.*, 2017, **56**, 8221–8225.
300 Y. Wang, J. Hong, W. Zhang and R. Xu, *Catal. Sci. Technol.*, 2013, **3**, 1703–1711.
301 K. Takanabe, K. Kamata, X. Wang, M. Antonietti, J. Kubota and K. Domen, *Phys. Chem. Chem. Phys.*, 2010, **12**, 13020–13025.
302 X. Zhang, L. Yu, C. Zhuang, T. Peng, R. Li and X. Li, *ACS Catal.*, 2013, **4**, 162–170.
303 A. Kumar, P. Kumar, C. Joshi, S. Ponnada, A. K. Pathak, A. Ali, B. Sreedhar and S. L. Jain, *Green Chem.*, 2016, **18**, 2514–2521.
304 R. Kuriki, K. Sekizawa, O. Ishitani and K. Maeda, *Angew. Chem., Int. Ed.*, 2015, **54**, 2406–2409.
305 R. Kuriki, M. Yamamoto, K. Higuchi, Y. Yamamoto, M. Akatsuka, D. Lu, S. Yagi, T. Yoshida, O. Ishitani and K. Maeda, *Angew. Chem., Int. Ed.*, 2017, **56**, 4867–4871.
306 E. S. Da Silva, N. M. Moura, M. G. P. Neves, A. Coutinho, M. Prieto, C. G. Silva and J. L. Faria, *Appl. Catal., B*, 2018, **221**, 56–69.
307 G. Dong, Z. Ai and L. Zhang, *RSC Adv.*, 2014, **4**, 5553–5560.
308 L. Li, D. Cruz, A. Savateev, G. Zhang, M. Antonietti and Y. Zhao, *Appl. Catal., B*, 2018, **229**, 249–253.
309 X. Liu, P. Wang, H. Zhai, Q. Zhang, B. Huang, Z. Wang, Y. Liu, Y. Dai, X. Qin and X. Zhang, *Appl. Catal., B*, 2018, **232**, 521–530.
310 A. Kumar, P. Kumar, R. Borkar, A. Bansiwal, N. Labhsetwar and S. L. Jain, *Carbon*, 2017, **123**, 371–379.
311 A. Kumar, P. Kumar, A. K. Pathak, A. N. Chokkapu and S. L. Jain, *ChemistrySelect*, 2017, **2**, 3437–3443.
312 Y.-N. Liu, C.-C. Shen, N. Jiang, Z.-W. Zhao, X. Zhou, S.-J. Zhao and A.-W. Xu, *ACS Catal.*, 2017, **7**, 8228–8234.
313 J. v. Liebig, *Ann. Pharmacother.*, 1834, **10**, 10.
314 A. Sattler, S. Schönberger and W. Schnick, *Z. Anorg. Allg. Chem.*, 2010, **636**, 476–482.
315 S. Chu, C. Wang, J. Feng, Y. Wang and Z. Zou, *Int. J. Hydrogen Energy*, 2014, **39**, 13519–13526.
316 J. Ehrmaier, T. N. Karsili, A. L. Sobolewski and W. Domcke, *J. Phys. Chem. A*, 2017, **121**, 4754–4764.
317 S. Liu, H. Sun, K. O'Donnell, H. Ang, M. O. Tade and S. Wang, *J. Colloid Interface Sci.*, 2016, **464**, 10–17.
318 T. Saplinova, V. Bakumov, T. Gmeiner, J. Wagler, M. Schwarz and E. Kroke, *Z. Anorg. Allg. Chem.*, 2009, **635**, 2480–2487.
319 L. Luo, M. Zhang, P. Wang, Y. Wang and F. Wang, *New J. Chem.*, 2018, **42**, 1087–1091.
320 S. Chu, Y. Wang, Y. Guo, J. Feng, C. Wang, W. Luo, X. Fan and Z. Zou, *ACS Catal.*, 2013, **3**, 912–919.
321 Y. Shiraishi, S. Kanazawa, Y. Kofuji, H. Sakamoto, S. Ichikawa, S. Tanaka and T. Hirai, *Angew. Chem., Int. Ed.*, 2014, **53**, 13454–13459.
322 Y. Kofuji, S. Ohkita, Y. Shiraishi, H. Sakamoto, S. Ichikawa, S. Tanaka and T. Hirai, *ACS Sustainable Chem. Eng.*, 2017, **5**, 6478–6485.
323 J.-D. Xiao, L.-G. Qiu, Y.-P. Yuan, X. Jiang, A.-J. Xie and Y.-H. Shen, *Inorg. Chem. Commun.*, 2013, **29**, 128–130.
324 J. Dasgupta, J. Sikder, S. Chakraborty, U. Adhikari, A. Mondal and S. Curcio, *ACS Sustainable Chem. Eng.*, 2017, **5**, 6817–6826.
325 C. Wang, Y. Guo, Y. Yang, S. Chu, C. Zhou, Y. Wang and Z. Zou, *ACS Appl. Mater. Interfaces*, 2014, **6**, 4321–4328.
326 A. Schwarzer, U. Böhme and E. Kroke, *Chem.–Eur. J.*, 2012, **18**, 12052–12058.
327 Y. Liao, J. Weber and C. F. Faul, *Macromolecules*, 2015, **48**, 2064–2073.
328 Y. Qian, I. A. Khan and D. Zhao, *Small*, 2017, **13**, 1701143.
329 C. Ye, J.-X. Li, H.-L. Wu, X.-B. Li, B. Chen, C.-H. Tung and L.-Z. Wu, *ACS Appl. Mater. Interfaces*, 2018, **10**, 3515–3521.
330 J. Yang, M. Xu, J. Wang, S. Jin and B. Tan, *Sci. Rep.*, 2018, **8**, 4200.
331 M. R. Liebl and J. r. Senker, *Chem. Mater.*, 2013, **25**, 970–980.
332 S. Ren, M. J. Bojdys, R. Dawson, A. Laybourn, Y. Z. Khimyak, D. J. Adams and A. I. Cooper, *Adv. Mater.*, 2012, **24**, 2357–2361.
333 O. Buyukcakir, S. H. Je, S. N. Talapaneni, D. Kim and A. Coskun, *ACS Appl. Mater. Interfaces*, 2017, **9**, 7209–7216.

334 R. K. Yadav, A. Kumar, N.-J. Park, K.-J. Kong and J.-O. Baeg, *J. Mater. Chem. A*, 2016, **4**, 9413–9418.
335 K. Kailasam, M. B. Mesch, L. Möhlmann, M. Baar, S. Blechert, M. Schwarze, M. Schröder, R. Schomäcker, J. Senker and A. Thomas, *Energy Technol.*, 2016, **4**, 744–750.
336 H. Li, H. Hu, C. Bao, F. Guo, X. Zhang, X. Liu, J. Hua, J. Tan, A. Wang and H. Zhou, *Sci. Rep.*, 2016, **6**, 29327.
337 S. N. Steinmann, S. T. Melissen, T. Le Bahers and P. Sautet, *J. Mater. Chem. A*, 2017, **5**, 5115–5122.
338 A. G. MacDiarmid, *Angew. Chem., Int. Ed.*, 2001, **40**, 2581–2590.
339 Y. Zhang, A. Thomas, M. Antonietti and X. Wang, *J. Am. Chem. Soc.*, 2009, **131**, 50.
340 D. R. Miller, D. C. Swenson and E. G. Gillan, *J. Am. Chem. Soc.*, 2004, **126**, 5372–5373.
341 C. Ma, J. Zhou, H. Zhu, W. Yang, J. Liu, Y. Wang and Z. Zou, *ACS Appl. Mater. Interfaces*, 2015, **7**, 14628–14637.
342 C. Ma, J. Zhou, Z. Cui, Y. Wang and Z. Zou, *Sol. Energy Mater. Sol. Cells*, 2016, **150**, 102–111.
343 Y. Gong, H. Yu, S. Chen and X. Quan, *RSC Adv.*, 2015, **5**, 83225–83231.
344 P. Meng, H. Heng, Y. Sun and X. Liu, *Appl. Surf. Sci.*, 2017, **428**, 1130–1140.
345 C. Ma, H. Zhu, J. Zhou, Z. Cui, T. Liu, Y. Wang, Y. Wang and Z. Zou, *Dalton Trans.*, 2017, **46**, 3877–3886.
346 T. Seçkin, N. Kıvılcım and S. Köytepe, *Polym.-Plast. Technol. Eng.*, 2013, **52**, 1368–1375.
347 M. K. Bhunia, S. Melissen, M. R. Parida, P. Sarawade, J.-M. Basset, D. H. Anjum, O. F. Mohammed, P. Sautet, T. Le Bahers and K. Takanabe, *Chem. Mater.*, 2015, **27**, 8237–8247.
348 E. Vorobyeva, Z. Chen, S. Mitchell, R. K. Leary, P. Midgley, J. M. Thomas, R. Hauert, E. Fako, N. López and J. Pérez-Ramírez, *J. Mater. Chem. A*, 2017, **5**, 16393–16403.
349 L. Sun, W. Hong, J. Liu, M. Yang, W. Lin, G. Chen, D. Yu and X. Chen, *ACS Appl. Mater. Interfaces*, 2017, **9**, 44503–44511.
350 L. Heymann, B. r. Schiller, H. Noei, A. Stierle and C. Klinke, *ACS Omega*, 2018, **3**, 3892–3900.
351 Y. Zhang, T. Mori, L. Niu and J. Ye, *Energy Environ. Sci.*, 2011, **4**, 4517–4521.
352 J. Duan, S. Chen, M. Jaroniec and S. Z. Qiao, *ACS Nano*, 2015, **9**, 931–940.
353 L. K. Putri, B.-J. Ng, W.-J. Ong, H. W. Lee, W. S. Chang and S.-P. Chai, *J. Mater. Chem. A*, 2018, **6**, 3181–3194.
354 W. Li, E. Rodríguez-Castellón and T. J. Bandosz, *J. Mater. Chem. A*, 2017, **5**, 24880–24891.
355 Y. Y. Han, X. L. Lu, S. F. Tang, X. P. Yin, Z. W. Wei and T. B. Lu, *Adv. Energy Mater.*, 2018, **8**, 1702992.
356 X. An, Y. Cao, Q. Liu, L. Chen, Z. Lin, Y. Zhou, Z. Zhang, J. Long and X. Wang, *Appl. Catal., A*, 2017, **546**, 30–35.
357 N. Ding, L. Zhang, M. Hashimoto, K. Iwasaki, N. Chikamori, K. Nakata, Y. Xu, J. Shi, H. Wu and Y. Luo, *J. Colloid Interface Sci.*, 2018, **512**, 474–479.
358 H. Li, H.-Y. Lee, G.-S. Park, B.-J. Lee, J.-D. Park, C.-H. Shin, W. Hou and J.-S. Yu, *Carbon*, 2018, **129**, 637–645.
359 W. Xing, C. Li, Y. Wang, Z. Han, Y. Hu, D. Chen, Q. Meng and G. Chen, *Carbon*, 2017, **115**, 486–492.
360 Y. Kofuji, Y. Isobe, Y. Shiraishi, H. Sakamoto, S. Tanaka, S. Ichikawa and T. Hirai, *J. Am. Chem. Soc.*, 2016, **138**, 10019–10025.
361 Y. Kofuji, Y. Isobe, Y. Shiraishi, H. Sakamoto, S. Ichikawa, S. Tanaka and T. Hirai, *ChemCatChem*, 2018, **10**, 2070–2077.
362 E. S. Cho, A. M. Ruminski, S. Aloni, Y.-S. Liu, J. Guo and J. J. Urban, *Nat. Commun.*, 2016, **7**, 10804.
363 R. Nagar, B. P. Vinayan, S. S. Samantaray and S. Ramaprabhu, *J. Mater. Chem. A*, 2017, **5**, 22897–22912.
364 G. K. Dimitrakakis, E. Tylianakis and G. E. Froudakis, *Nano Lett.*, 2008, **8**, 3166–3170.
365 S. Hu, M. Lozada-Hidalgo, F. C. Wang, A. Mishchenko, F. Schedin, R. R. Nair, E. W. Hill, D. W. Boukhvalov, M. I. Katsnelson, R. A. W. Dryfe, I. V. Grigorieva, H. A. Wu and A. K. Geim, *Nature*, 2014, **516**, 227–230.
366 L. Yang, X. Li, G. Zhang, P. Cui, X. Wang, X. Jiang, J. Zhao, Y. Luo and J. Jiang, *Nat. Commun.*, 2017, **8**, 16049.
367 H. Huang, S. Yang, R. Vajtai, X. Wang and P. M. Ajayan, *Adv. Mater.*, 2014, **26**, 5160–5165.
368 X. Zou, X. Huang, A. Goswami, R. Silva, B. R. Sathe, E. Mikmeková and T. Asefa, *Angew. Chem.*, 2014, **126**, 4461–4465.
369 Y. Liu, G.-D. Li, L. Yuan, L. Ge, H. Ding, D. Wang and X. Zou, *Nanoscale*, 2015, **7**, 3130–3136.
370 L. Zhang, N. Ding, M. Hashimoto, K. Iwasaki, N. Chikamori, K. Nakata, Y. Xu, J. Shi, H. Wu and Y. Luo, *Nano Res.*, 2018, **11**, 2295–2309.
371 G. Zhang, A. Savateev, Y. Zhao, L. Li and M. Antonietti, *J. Mater. Chem. A*, 2017, **5**, 12723–12728.
372 S. Z. Butler, S. M. Hollen, L. Cao, Y. Cui, J. A. Gupta, H. R. Gutiérrez, T. F. Heinz, S. S. Hong, J. Huang and A. F. Ismach, *ACS Nano*, 2013, **7**, 2898–2926.
373 P. Miró, M. Audiffred and T. Heine, *Chem. Soc. Rev.*, 2014, **43**, 6537–6554.
374 M. Xu, T. Liang, M. Shi and H. Chen, *Chem. Rev.*, 2013, **113**, 3766–3798.
375 W.-J. Ong, *Frontiers Mater.*, 2017, **4**, 11.
376 F. Xia, H. Wang, D. Xiao, M. Dubey and A. Ramasubramaniam, *Nat. Photonics*, 2014, **8**, 899–907.
377 W. Hu, L. Lin, R. Zhang, C. Yang and J. Yang, *J. Am. Chem. Soc.*, 2017, **139**, 15429–15436.
378 B. Wang, A. Kuang, X. Luo, G. Wang, H. Yuan and H. Chen, *Appl. Surf. Sci.*, 2018, **439**, 374–379.
379 W. Zhao, Z. Ghorannevis, L. Chu, M. Toh, C. Kloc, P.-H. Tan and G. Eda, *ACS Nano*, 2012, **7**, 791–797.
380 D. A. Reddy, H. Park, R. Ma, D. P. Kumar, M. Lim and T. K. Kim, *ChemSusChem*, 2017, **10**, 1563–1570.
381 Y. Zou, D. Shi, D. Ma, Z. Fan, L. Cheng, D. Sun, Z. Wang and C. Niu, *ChemSusChem*, 2018, **11**, 1187–1197.
382 M. Zhu, Y. Osakada, S. Kim, M. Fujitsuka and T. Majima, *Appl. Catal., B*, 2017, **217**, 285–292.
383 P. Qiu, C. Xu, N. Zhou, H. Chen and F. Jiang, *Appl. Catal., B*, 2018, **221**, 27–35.
384 X. Zong and L. Wang, *J. Photochem. Photobiol., C*, 2014, **18**, 32–49.

385 A. Mukherji, R. Marschall, A. Tanksale, C. Sun, S. C. Smith, G. Q. Lu and L. Wang, *Adv. Funct. Mater.*, 2011, **21**, 126–132.
386 N. Baliarsingh, L. Mohapatra and K. Parida, *J. Mater. Chem. A*, 2013, **1**, 4236–4243.
387 Y. Matsumoto, M. Koinuma, Y. Iwanaga, T. Sato and S. Ida, *J. Am. Chem. Soc.*, 2009, **131**, 6644–6645.
388 J. Liu, J. Li, X. Bing, D. H. Ng, X. Cui, F. Ji and D. D. Kionga, *Mater. Res. Bull.*, 2018, **102**, 379–390.
389 S. Tonda, S. Kumar, M. Bhardwaj, P. Yadav and S. Ogale, *ACS Appl. Mater. Interfaces*, 2018, **10**, 2667–2678.
390 S. Nayak, L. Mohapatra and K. Parida, *J. Mater. Chem. A*, 2015, **3**, 18622–18635.
391 B. Luo, R. Song and D. Jing, *Int. J. Hydrogen Energy*, 2017, **42**, 23427–23436.
392 H. Sahabudeen, H. Qi, B. A. Glatz, D. Tranca, R. Dong, Y. Hou, T. Zhang, C. Kuttner, T. Lehnert and G. Seifert, *Nat. Commun.*, 2016, **7**, 13461.
393 B. C. Patra, S. Khilari, R. N. Manna, S. Mondal, D. Pradhan, A. Pradhan and A. Bhaumik, *ACS Catal.*, 2017, **7**, 6120–6127.
394 A. J. Clough, J. W. Yoo, M. H. Mecklenburg and S. C. Marinescu, *J. Am. Chem. Soc.*, 2015, **137**, 118–121.
395 R. Zhang, B. Li and J. Yang, *Nanoscale*, 2015, **7**, 14062–14070.
396 R. Zhang and J. Yang, arXiv preprint arXiv:1505.02768, 2015.
397 D. Wang, D. Han, L. Liu and L. Niu, *RSC Adv.*, 2016, **6**, 28484–28488.
398 Z. Guan, J. Li and W. Duan, arXiv preprint arXiv:1510.09022, 2015.
399 J. Du, C. Xia, W. Xiong, X. Zhao, T. Wang and Y. Jia, *Phys. Chem. Chem. Phys.*, 2016, **18**, 22678–22686.
400 C. N. M. Ouma, K. O. Obodo, M. Braun and G. O. Amolo, *J. Mater. Chem. C*, 2018, **6**, 4015–4022.
401 M. Yagmurcukardes, S. Horzum, E. Torun, F. M. Peeters and R. T. Senger, *Phys. Chem. Chem. Phys.*, 2016, **18**, 3144–3150.
402 M. Ashwin Kishore and P. Ravindran, *J. Phys. Chem. C*, 2017, **121**, 22216–22224.
403 J. Mahmood, E. K. Lee, M. Jung, D. Shin, H.-J. Choi, J.-M. Seo, S.-M. Jung, D. Kim, F. Li and M. S. Lah, *Proc. Natl. Acad. Sci. U. S. A.*, 2016, **113**, 7414–7419.
404 K. Bhattacharyya, S. M. Pratik and A. Datta, *J. Phys. Chem. C*, 2018, **122**, 2248–2258.
405 Y. Wang, Q. Yang, C. Zhong and J. Li, *J. Phys. Chem. C*, 2016, **120**, 28782–28788.
406 X. Luo, G. Wang, Y. Huang, B. Wang, H. Yuan and H. Chen, *Phys. Chem. Chem. Phys.*, 2017, **19**, 28216–28224.
407 Z. Guan, C.-S. Lian, S. Hu, S. Ni, J. Li and W. Duan, *J. Phys. Chem. C*, 2017, **121**, 3654–3660.
408 S. Y. Lim, W. Shen and Z. Gao, *Chem. Soc. Rev.*, 2015, **44**, 362–381.
409 Y. Wang and A. Hu, *J. Mater. Chem. C*, 2014, **2**, 6921–6939.
410 X. Chen, Q. Liu, Q. Wu, P. Du, J. Zhu, S. Dai and S. Yang, *Adv. Funct. Mater.*, 2016, **26**, 1719–1728.
411 L. Wang, S.-J. Zhu, H.-Y. Wang, S.-N. Qu, Y.-L. Zhang, J.-H. Zhang, Q.-D. Chen, H.-L. Xu, W. Han and B. Yang, *ACS Nano*, 2014, **8**, 2541–2547.
412 X. Li, M. Rui, J. Song, Z. Shen and H. Zeng, *Adv. Funct. Mater.*, 2015, **25**, 4929–4947.
413 K. S. Fernando, S. Sahu, Y. Liu, W. K. Lewis, E. A. Guliants, A. Jafariyan, P. Wang, C. E. Bunker and Y.-P. Sun, *ACS Appl. Mater. Interfaces*, 2015, **7**, 8363–8376.
414 H. Yu, R. Shi, Y. Zhao, G. I. Waterhouse, L. Z. Wu, C. H. Tung and T. Zhang, *Adv. Mater.*, 2016, **28**, 9454–9477.
415 J. Di, J. Xia, M. Ji, H. Li, H. Xu, H. Li and R. Chen, *Nanoscale*, 2015, **7**, 11433–11443.
416 F. Nan, Z. Kang, J. Wang, M. Shen and L. Fang, *Appl. Phys. Lett.*, 2015, **106**, 153901.
417 J. J. Lv, J. Zhao, H. Fang, L. P. Jiang, L. L. Li, J. Ma and J. J. Zhu, *Small*, 2017, **13**, 1700264.
418 K.-H. Ye, Z. Wang, J. Gu, S. Xiao, Y. Yuan, Y. Zhu, Y. Zhang, W. Mai and S. Yang, *Energy Environ. Sci.*, 2017, **10**, 772–779.
419 H. Yu, Y. Zhao, C. Zhou, L. Shang, Y. Peng, Y. Cao, L.-Z. Wu, C.-H. Tung and T. Zhang, *J. Mater. Chem. A*, 2014, **2**, 3344–3351.
420 C. X. Guo, Y. Dong, H. B. Yang and C. M. Li, *Adv. Energ. Mater.*, 2013, **3**, 997–1003.
421 Z. Cheng, F. Wang, T. A. Shifa, K. Liu, Y. Huang, Q. Liu, C. Jiang and J. He, *Appl. Phys. Lett.*, 2016, **109**, 053905.
422 J. Xie, J. Chen and C. M. Li, *Int. J. Hydrogen Energy*, 2017, **42**, 7158–7165.
423 B. C. Martindale, G. A. Hutton, C. A. Caputo and E. Reisner, *J. Am. Chem. Soc.*, 2015, **137**, 6018–6025.
424 H. Maaoui, P. Kumar, A. Kumar, G.-H. Pan, R. Chtourou, S. Szunerits, R. Boukherroub and S. L. Jain, *Photochem. Photobiol. Sci.*, 2016, **15**, 1282–1288.
425 Z. Qian, J. Ma, X. Shan, H. Feng, L. Shao and J. Chen, *Chem.–Eur. J.*, 2014, **20**, 2254–2263.
426 X. Shan, L. Chai, J. Ma, Z. Qian, J. Chen and H. Feng, *Analyst*, 2014, **139**, 2322–2325.
427 M. Xu, G. He, Z. Li, F. He, F. Gao, Y. Su, L. Zhang, Z. Yang and Y. Zhang, *Nanoscale*, 2014, **6**, 10307–10315.
428 S. Sahu, Y. Liu, P. Wang, C. E. Bunker, K. S. Fernando, W. K. Lewis, E. A. Guliants, F. Yang, J. Wang and Y.-P. Sun, *Langmuir*, 2014, **30**, 8631–8636.
429 K. Li, F.-Y. Su and W.-D. Zhang, *Appl. Surf. Sci.*, 2016, **375**, 110–117.
430 J. Liu, Y. Liu, N. Liu, Y. Han, X. Zhang, H. Huang, Y. Lifshitz, S.-T. Lee, J. Zhong and Z. Kang, *Science*, 2015, **347**, 970–974.
431 G. Zhang, Q. Ji, Z. Wu, G. Wang, H. Liu, J. Qu and J. Li, *Adv. Funct. Mater.*, 2018, **28**, 1706462.
432 I. Majeed, U. Manzoor, F. K. Kanodarwala, M. A. Nadeem, E. Hussain, H. Ali, A. Badshah, J. A. Stride and M. A. Nadeem, *Catal. Sci. Technol.*, 2018, **8**, 1183–1193.
433 S. L. Shinde, S. Ishii, T. D. Dao, R. P. Sugavaneshwar, T. Takei, K. K. Nanda and T. Nagao, *ACS Appl. Mater. Interfaces*, 2018, **10**, 2460–2468.
434 P. Devaraji and C. S. Gopinath, *Int. J. Hydrogen Energy*, 2018, **43**, 601–613.
435 S. Liu, J. Tian, L. Wang, Y. Luo, J. Zhai and X. Sun, *J. Mater. Chem.*, 2011, **21**, 11726–11729.
436 S. Barman and M. Sadhukhan, *J. Mater. Chem.*, 2012, **22**, 21832–21837.

437 S. Liu, L. Wang, J. Tian, J. Zhai, Y. Luo, W. Lu and X. Sun, *RSC Adv.*, 2011, **1**, 951–953.
438 Q. Cui, J. Xu, X. Wang, L. Li, M. Antonietti and M. Shalom, *Angew. Chem., Int. Ed.*, 2016, **55**, 3672–3676.
439 W. Wang, C. Y. Jimmy, Z. Shen, D. K. Chan and T. Gu, *Chem. Commun.*, 2014, **50**, 10148–10150.
440 N. Wang, H. Fan, J. Sun, Z. Han, J. Dong and S. Ai, *Carbon*, 2016, **109**, 141–148.
441 X. Lin, D. Xu, J. Zheng, M. Song, G. Che, Y. Wang, Y. Yang, C. Liu, L. Zhao and L. Chang, *J. Alloys Compd.*, 2016, **688**, 891–898.
442 J. Su, L. Zhu, P. Geng and G. Chen, *J. Hazard. Mater.*, 2016, **316**, 159–168.
443 B. Sun, N. Lu, Y. Su, H. Yu, X. Meng and Z. Gao, *Appl. Surf. Sci.*, 2017, **394**, 479–487.
444 J. Su, L. Zhu and G. Chen, *Appl. Catal., B*, 2016, **186**, 127–135.
445 Y.-C. Lu, J. Chen, A.-J. Wang, N. Bao, J.-J. Feng, W. Wang and L. Shao, *J. Mater. Chem. C*, 2015, **3**, 73–78.